QUANTITATIVE ANALYSIS ON THE FORMATION OF METAL NANOCRYSTALS

BY

YIMING WANG

DISSERTATION

Submitted in partial fulfillment of the requirements
for the degree of Doctor of Philosophy in Chemistry
in the Graduate College of the
University of Illinois Urbana-Champaign, 2021

Urbana, Illinois

Doctoral Committee:

Professor Yi Lu, Chair
Professor Prashant K. Jain
Professor Catherine J. Murphy
Professor Hong Yang

ABSTRACT

It is desirable to rationally engineer nanomaterials with predictable structures and properties, thereby producing desirable functions for their applications on demand. However, most of the nanostructures are discovered by iterative screening of synthetic strategies, which is labor intensive and time consuming. The future of nanomaterials research lies in digitalizing the nanomaterials formation process, so scientists can design and optimize synthetic protocols by computer simulations. Therefore, in my thesis work, I focus on quantitative analysis on the formation of metal nanocrystals to extract appropriate parameters for predictive modeling and synthesis.

Predictive synthesis of metal nanocrystals with desired structures relies on precise control of the reaction kinetics. Using a capping ligand is an effective method to affect the reduction kinetics of metal ions precursors. However, predictively synthesizing nanostructures has been difficult to achieve using conventional capping ligands. DNA, as a class of the promising biomolecular capping ligands, has been used to generate sequence-specific morphologies in various metal nanocrystals. However, mechanistic insight into the DNA-mediated nanocrystal formation remains elusive due to the lack of quantitative experimental evidence. In Chapter 2, I quantitatively analyzed the precise control of DNA over Ag^+ reduction and the structures of resulting Au-Ag core shell nanocrystals. I derived the equilibrium binding constants between DNA and Ag^+, the kinetic rate constants of sequence specific Ag^+ reduction pathways, and the percentage of active surface sites remaining on the nanocrystals after DNA passivation. These three synergistic factors influence the nucleation and growth process both thermodynamically and kinetically, which contributed to the morphological evolution of Au-Ag nanocrystals synthesized with different DNA sequences. This study demonstrates the potential of using

functional DNA sequences as a versatile and tunable capping ligand system for the predictable synthesis of metal nanostructures.

Besides the challenges in predicting the reaction kinetics, the tangled relationships between each functional parameter and multiple structural parameters also make it more difficult to predicting the functions of the resulting nanostructures. Researchers need to deconvolute the structure-function relationships and understand the co-evolution of structural and functional parameters as the nanostructures grow. DNA is a programmable biomolecular capping ligand that has superior control over the kinetic evolution of metal nanostructures. In Chapter 3, I systematically analyzed the evolution of two structural parameters and several functional parameters in the growth of Au-Ag nanostructures controlled by two DNA sequences. I deconvoluted the contributions from the two structural parameters in affecting the plasmonic properties of the nanostructures in different kinetic and geometric domains. I further designed new nanostructures by exchanging DNA sequences in the growth environment, which also exchanged their kinetic evolution pathways. The resulting structural and functional parameters could be predictively tuned by the timing of the exchange. This study shows that by understanding the kinetic evolution of the structural parameters and their relationships with the function parameters, it is possible to design the precise combinations of structural and functional parameters in the nanostructured products of a synthesis reaction.

To fully digitalize the reaction of the formation of metal nanocrystals, it is essential to establish the quantitative relationships between the reactants, the kinetics and the resulting nanostructures. The key parameters for the quantitative description are the energy terms of the reaction, such as free energy and activation energy. Typically, those energy terms are primarily obtained by simulation because they are very difficult to be measured experimentally. However,

those energy terms can be easily measured in an electrochemical cell. The redox reaction in the synthesis of metal nanocrystals can be understood in the concept of a battery. The cathodic reaction is the reduction of metal ions, and the anodic reaction is the oxidation of reducing agents. The free energy, activation energy and reaction kinetics in the synthesis reaction can be converted to the potential, overpotential and current output of the battery. Using this concept, we can establish quantitative relationships between the reactants, the kinetics, and the resulting nanocrystals, similar to the voltage-current relationships in a battery. This conceptual model will enable scientists to make informed choices of chemical reactants in a synthetic protocol based on the desired nanostructured outcome, which will significantly reduce trial and error. In Chapter 4, I demonstrated this idea in a model system of synthesizing Palladium nanocrystals. By modulating redox potentials of the starting chemical reactants, the reaction kinetics and the size of the resulting Palladium nanostructures were tunable.

The three works in this thesis constitute a comprehensive investigation of the quantitative relationships between starting reactants, reaction kinetics, structures, and functions of the resulting nanostructures in a synthesis reaction for metal nanocrystals. In a future predictive synthesis, once a specific function is designed by the end user, the structure-functional relationship in Chapter 3 will help the simulation of functional as well as the structural evolution pathways of the nanostructures; The quantitative kinetic analysis in Chapter 2 will enable the prediction of how much and how fast the atom should be added onto the growing crystal as the nanostructures evolve, and as a result the global reaction kinetics over the course of the reaction. Finally, based on the quantitative relationship between the kinetics and the driving force derived in Chapter 4, we could precisely choose the type of precursors and reducing agents as well as their concentrations based on the combination of their redox potentials that drive the desired

reaction kinetics. The quantitative relationships between the starting reactants, reaction kinetics as well as the structures and functions of the nanostructures signify a major step towards predictive synthesis of nanostructures from functional design.

ACKNOWLEDGEMENTS

I am amazed by how many people I have met, and how many memories I have created in the past five years. Looking back at my Ph.D. journey, I am full of gratitude. I want to thank Dr. Lu for giving me the freedom to explore my research interest even though it was quite different from the rest of the lab. Thanks Dr. Yang for spending so much time revising my papers, encouraging me to pursuit difficult research topics, and acknowledging the significance of my research when I was in serious self-doubt. Thanks Dr. Murphy for being a beacon in my life, letting me to see how powerful a female scientist can be, and giving me motherly warmth and support. Thanks Dr. Joaquin Rodriguez for leading me into the world of electrochemistry, graciously offering me lab space during the pandemic, and introducing me to his amazing students for collaboration. Thanks Dr. Jain for giving me great respect and patience when I first sought for collaboration in my second year. Thanks Dr. Olson for teaching me how to love the students, and how to make the class fun and inspiring. I also want to thank my parents for always being supportive and understanding. Even though we have been separated in two sides of the earth, their unconditional support was the reason for me to be brave in pursuing my dream and face all the challenges in life. Thanks to my boyfriend Jeffrey, who is not only my best friend but also gave me great support when I went through up and downs in life.

I want to thank the Lu group, both current members and those who have graduated, including the visiting students who have gone back to their home countries. I have encountered at least 50 members in Lu group in the past five years. Shout out to my amazing mentor Nitya. You taught me so much during the two years when we had overlap, which prepared me for independence after you graduated. You have so much wisdom. I couldn't have survived the five years without your suggestions. Thanks to Greg, who have walked the entire five years with me.

Thank you for listening to me complaining about life and offering wise suggestions. You always have the humor to joke about everything, which magically made seemingly unbearable things insignificant. Thanks to Tingjie and Ana. We have once been the only members of the close-to-extinct “material subgroup”. We shared a common interest for nano, soccer, and love for Amy (Tingjie’s daughter). I am grateful to have someone in lab to discuss about research as well as life, you made me feel less lonely. Thanks to Claire, Ryan and Kevin. You were the senior students when I first joined the lab. You taught me how senior students should take responsibility and genuinely love the group members. You have been my great friends and mentors for navigating through graduate school. Thanks Suds for gave me so much advice when I was looking for postdoc position. You are such a wise and caring person who sincerely want to help others to grow. I am sure you will be a great leader who will love your fellows to pieces! I also want to thank Zhenglin, Yuting, Mingkuan, Quan, Mandy, Quanbin and Yuan and many the visiting students who I have met, past and present. Your diligence, humility and kindness always motivated me to be a better scientist like you. Thank you all!

I would also like to thank everyone who have helped International Chemists Association (ICA). Chang and I founded ICA in 2019. Lloyd first encouraged us to establish this organization and helped us tremendously in getting the initial resources. Thanks to Alison and Hannah, who are experienced student leaders in the department. They saw our struggles as a newly established organization, so they reached out to help us come up with events and taught us hand by hand on how to organize departmental level events. I want to thank to all current members of ICA, Yu, Qi, Dinu, Aastha, Sagnik, Saman, Priti. I am so thankful to have met all of you who also love and care for international students. I am especially encouraged by the second-year students who have grown tremendously during serving in ICA in the past year. During the

departmental new student weekend (Feb 2021), I had a concussion. I was not only cognitively compromised but also physically weak. I was anxious about not being able to lead the event. Yu volunteered to take on the leadership role, together with everyone in ICA, led a most heartfelt welcoming event for the international students. Now Qi and Sagnik took on the leadership roles as both Yu and I are leaving UIUC. I am so grateful to see an organization that I initiated are now be taken over by a group of caring, loving friends. I feel fortunate to be able to serve the international communities with you all in the past two years, and I am so encouraged to see that ICA can continue to serve the international student community without me in the future.

I would like to thank my collaborators, Michael, Kendrich, Ahyoung, Junfeng, Edzna, Justin and Dinu. Thank you for being so open-minded and adventurous about trying out the crazy ideas with me. Thank you for always being patient in teaching me your expertise. Even though some of our collaboration has not produced any paper, but we learned something from each other and had fun exploring the unknowns. This was also how we developed lifelong friendship. You are all amazing scientist, and I am grateful you have met you all! I would also like to thank the ladies in the IMP office. You are always so helpful and encouraging. You always prepared ways to light up our day (candies, notes of encouraging words, etc) You have made graduate school so much more delightful!

I would like to thank my fellowship - Illini Chinese Christian Fellowship (ICCF). ICCF is where I was baptized, grew, and served. I consider all the brothers and sisters as my dear family. You have supported me and loved me in the ways that only God can. We shared each other's burden in life and encouraged each other in the journey of faith. Thank you for teaching me how to love. Thank you for reminding me to be humble when I was proud, to be vulnerable when I was overwhelmed. It is hard for me to say goodbye to all of you. However, I know that God will

take good care of you after I leave. You will always in my prayer. Pray that all of you will be fruitful and faithful wherever you go in the world!

I would also like to thank campus recreation. I had so much fun in participating in group fitness classes in the past five years. I also thank Rosa and Yiyi in helping me to become an instructor myself. It was an empowering journey, which not only made me physically strong but letting me see how much power and potential I can possibly have. Also thanks to second wind running club. I am grateful to have met the group of amazing runners, who are so committed and so caring. You led me into the world of running. You not only motivated me to get up at 6 am in the freezing winter but also let me see how fun running can be!

As a scientist, I have always been amazed by how extraordinary nature is. I want to thank God for creating this beautiful universe and giving me the privilege to be in the vocation to explore the intricate natural mechanisms. Whenever I was frustrated, I always thought of how God radically loves this broken world. This fact motivated me to use my insignificant creative ability to make this world a little bit more lovable. Going forward, I am excited to continue to expand the boundary of human knowledge and think hard on how to use my research to promote human flourishing. I also want to be humbler and be better at loving people. As fallible as I have been, I am tremendously grateful to have walked this journey with all of you amazing people.

For those who are reading this thesis, wish you have a legendary graduate school experience, and enjoy the exploration of the wonder of nature!

Dedicated to our heavenly Father

TABLE OF CONTENTS

CHAPTER 1: INTRODUCTION 1

1.1 Introduction 2

1.2 Sequence-specific control of inorganic nanomaterial morphologies by DNA 4

1.3 Sequence-specific control of inorganic nanomaterial morphologies by peptides 9

1.4 Sequence-specific interaction with nanomaterials surface 12

1.5 Sequence-specific interaction with precursor 15

1.6 Properties resulting from the sequence-specific control 16

1.7 Optical properties including surface enhanced Raman spectroscopy (SERS) 16

1.8 Catalytic properties 18

1.9 Biomedical imaging and nanomedicine 19

1.10 Summary and outlook 19

1.11 References 22

CHAPTER 2: QUANTITATIVE ANALYSIS OF DNA-MEDIATED FORMATION OF METAL NANOCRYSTALS 29

2.1 Introduction 29

2.2 Results and discussion 31

2.2.1 Morphology of DNA controlled metal nanocrystals 31

2.2.2 Interaction between DNA and the Ag precursor: 35

2.2.3 DNA-mediated Ag^{+} reduction pathways 39

2.2.4 Kinetic analyses of the DNA-mediated Ag^{+} reduction pathways in the absence of pre-synthesized seed 45
2.2.5 Kinetic analyses of the DNA-mediated Ag+ reduction pathways in the presence of pre-synthesized seed. 53
2.2.6 Interactions between DNA and the surface of nanocrystals 60
2.2.7 Proposed mechanism for morphology evolution 65
2.3 Conclusion 67
2.4 Experimental section 68
2.4.1 Chemicals and Materials 68
2.4.2 Preparation of Au Decahedra NPs 69
2.4.3 DNA-Mediated Synthesis of Au-Ag Core-Shell NPs 69
2.4.4 Measurement of open circuit potential of AgOAc Solution with different DNA sequences 69
2.4.5 Instrumentation and Characterization 70
2.5 References 70
CHAPTER 3: KINETIC RECONSTRUCTION OF DNA PROGRAMMED PLASMONIC METAL NANOSTRUCTURES WITH PREDICTABLE SHAPES AND OPTICAL PROPERTIES 78
3.1 Introduction 78
3.2 Results and discussion 80
3.2.1 Structural descriptions of DNA controlled Au-Ag nanostructures 80
3.2.2 Optical properties of DNA controlled nanostructures 86

3.2.3 Kinetic reconstruction of Au-Ag nanostructures 93

3.2.4 Optical properties of kinetically reconstructed Au-Ag nanostructures..... 97

3.2.5 Mechanisms for DNA controlled structural evolution of Au-Ag nanostructures..... 103

3.3 Conclusion 108

3.4 Experimental section..... 109

3.4.1 Chemicals and Materials..... 109

3.4.2 Preparation of Au Bipyramid seeds 110

3.4.3 DNA-Mediated Synthesis of Au-Ag Core-Shell NPs..... 110

3.4.4 Kinetic reconstruction of DNA controlled Au-Ag nanostructures 110

3.4.5 Instrumentation and Characterization 111

3.5 Reference 111

CHAPTER 4: QUANTITATIVE DESIGN OF METAL NANOCRYSTAL SYNTHESIS USING ELECTROCHEMISTRY 118

4.1 Introduction..... 118

4.2 Results and discussion 119

4.2.1 Introduction of ultramicroelectrode 119

4.2.2 Choosing reducing agents 123

4.2.3 Measuring reduction potentials and overpotentials of metal precursors 126

4.2.4 Monitoring reduction kinetics..... 129

4.2.5 Effect of different concentration of ligand..... 131

4.3 Conclusion 136

4.4 Experimental section..... 137

4.4.1 Fabrication of Ultramicroelectrode 137

4.4.2 Pd nanocrystal synthesis and monitoring reaction kinetics 137

4.5 References 137

CHAPTER 1: INTRODUCTION[1]

Nanomaterials refer to the materials with at least one dimension reaching the nanometer scale (1-100 nm). The small size of nanomaterials gives rise to novel properties that revolutionize the way materials interact with our daily life. The applications of nanomaterials range from cancer therapy and anti-stain coating to television screen. The ultimate goal is to rationally engineer nanomaterials with predictable structures and properties, thereby producing desirable functions for their applications on demand. However, most of the nanostructures are discovered by iterative screening of synthetic strategies, which is labor intensive and time consuming. The future of nanomaterials research lies in digitalizing the nanomaterials formation process, so scientists can design and optimize synthetic protocols by computer simulations. In order to realize the dream, experimentalists first need to extract initial parameters from experiments to feed into computer models. However, it is overwhelming to choose the appropriate parameters out of numerous physical and chemical variables in nanomaterials formation processes. Furthermore, there are limited experimental tools and theoretical frameworks to measure and conceptualize the parameters. Therefore, in my thesis work, I focus on quantitative analysis on the formation of metal nanocrystals to extract appropriate parameters for predictive modeling and synthesis. Specifically, in Chapter 2 and 3, I will talk about DNA controlled synthesis of metal nanocrystals. For the remaining of this Chapter, I will provide more background on this topic.

[1] Part of this chapter was published in "Wang, Y.; Reddy Satyavolu, N. S.; Lu, Y., Sequence-specific control of inorganic nanomaterials morphologies by biomolecules. *Current Opinion in Colloid & Interface Science* **2018,** *38*, 158-169"

1.1 Introduction

In the synthesis of inorganic nanomaterials, capping agents play an important role in determining the size, shape and growth kinetics of the nanostructures. Biomolecules are a special class of capping agents that can bind to the surface of the nanomaterials, lower their surface energy, and thus affect the nanomaterials growth at different stages, both kinetically and thermodynamically, resulting in different morphologies. For example, in the synthesis of metal nanoparticles, metal ions are firstly reduced by either an exogenous reductant or endogenous reducing functional groups on biomolecules themselves; Biomolecules may also interact with the precursors by forming a complex, which can be the direct template for the following nucleation and growth events.[1] During the metal particle formation, biomolecules may interact with the forming nanocrystals based on their specific molecular recognition and hence produce specific-faceted nanostructures.

Nature has demonstrated it is possible to control the synthesis of biomaterials such as bones and sea shells, at the molecular level, using biomolecules with specific sequences that form different structures.[2] Therefore, mimicking the natural process to achieve sequence-specific control of nanomaterials morphology has been a major endeavor in the field of nanomaterial synthesis. Morphology-controlled synthesis is known to be related to facet-specific interactions of capping ligands with inorganic materials.[3] The interactions are mainly driven by soft epitaxial matching, which involves the coordination of polarizable functional groups in the ligands (e.g., O, N, C) with hollow sites on different facets of nanomaterials.[4-5] Biomolecules have diverse functional groups that contain these polarizable atoms, such as the phosphodiester backbone and the nitrogen or oxygen atoms in nucleobases, including N7 and N1 of adenine, N7 and O6 of guanine, and N3 of cytosine and thymine[6] (Fig. 1.1a) of DNA, as well as -NH_2, -CO_2H, -OH, -SH

in the side chains of peptides[7] (Fig. 1.1b). These functional groups in different sequences of biomolecules allow different coordination modes onto the materials' surfaces, directing the nanocrystals to grow into different morphologies.

Apart from the functional groups, other properties such as length and conformation, including secondary and tertiary structures, can also affect the interaction between biomolecules and nanomaterials.[8] For example, Hamad-Schifferli and coworkers[9] showed that the location of the DNA bases with high or low affinity towards gold nanoparticles determines whether they have "laid down" or exhibited random coil conformation. Peptides also exhibited sequence-specific conformational change on inorganic materials. For example, Ruan et al.[10] explored the effect of compositional and conformational changes of a platinum (111) facet-specific peptide on its facet-binding properties and identified phenylalanine as the key to facet selectivity. In addition, the importance of conformation of CTPR3 protein that binds to gold ion in determining the initial nucleation step of gold nanoparticle formation has also been established.[1] All these studies have clearly demonstrated the importance of sequence-specific biomolecules in controlling the morphologies of inorganic materials.

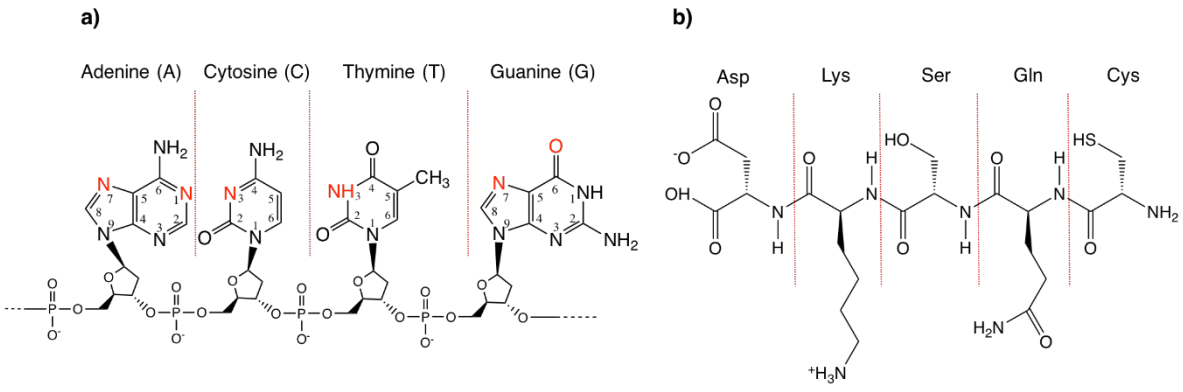


Figure 1.1: Structures of a) DNA and b) peptide with representative sequences. The potential coordination sites in DNA bases are highlighted in red.

1.2 Sequence-specific control of inorganic nanomaterial morphologies by DNA

DNA sequences have been screened for synthesis of various metal nanoparticles, including Au[11-14], Ag[15] and Pd@Au[16] core-shell nanoparticles. In the case of Au nanoparticles, Song et al. [17] screened homo-oligo nucleotides as well as sequences with different base combinations for controlling the morphology of Au nanorod overgrowth. The structures synthesized in the presence of homo-oligo nucleotides with 20 adenine bases (A20) exhibited dumbbell-shaped nanostructures, whereas G20 (G = guanine) yielded octahedron-shaped nanostructures. Meanwhile, the particles synthesized in the presence of T20 (T = thymine) or C20 (C = cytosine) grew into cracked octahedron with smooth facets (Fig. 1.2a). When the sequences with two base combinations were applied in the synthesis, A and G bases exhibited dominating effects over C and T in determining the final morphology. Whereas if A and G bases are combined, the final structure could be precisely tuned from dumbbell shape to octahedron shape, depending on the ratio of A and G in the sequence applied. The authors have also conducted a detailed mechanistic study, and proposed that the differences in nanoparticle morphologies resulted from the different binding affinity of DNA bases to the gold surface. Adenine has the highest binding affinity; Therefore, it could stabilize the high-energy side facets ({110} and {100} facets) during the nanoparticle growth, which resulted in longitudinal growth from the end of gold nanorod into a dumbbell shape. On the other hand, G has a low affinity, which cannot stabilize side facets, resulting in transversal growth into the octahedral shape. C and T have intermediate binding affinity, between A and G, hence can form the transitional cracked octahedron morphology. Finally, the authors also investigated the effect of phosphorothioate modified A20 sequence on the final morphology of the particles. The results showed that by varying the number of phosphorothioate modifications on the strand, the intra-particle gap between the two spheres in the

A20 dumbbell could be controlled. As a result of these morphological differences, the localized surface plasmon resonance (LSPR) peaks can be tuned from visible to second near-infrared (NIR-II) region.

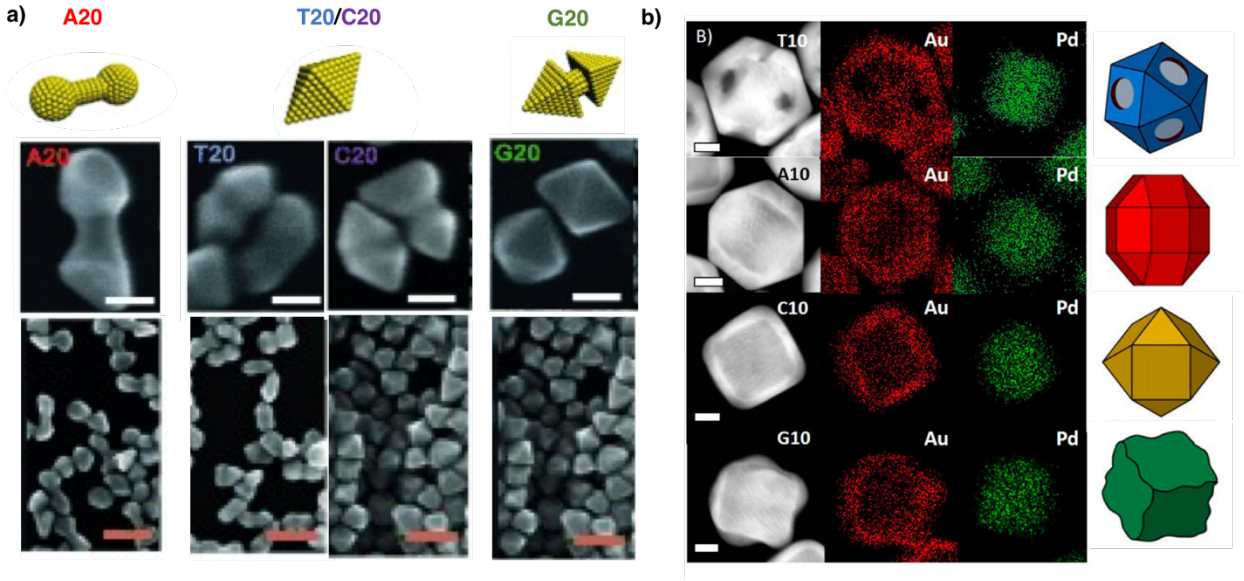


Figure 1.2: Sequence-specific control of inorganic nanomaterial morphologies by DNA. a) SEM images of gold nanoparticle morphologies produced with A20, T20, C20, and G20 at different magnifications and corresponding models. Adapted with permission from reference [26]. Copyright 2015, John Wiley and Sons. Sacle bars = 30 nm for the top row. Scale bars = 100nm for the bottom row. b) STEM and elemental mapping images of the Pd−Au nanoparticles synthesized in the presence of T10, A10, C10, and G10 and models of corresponding particles. Adapted with permission from reference [25]. Copyright 2016 American Chemical Society. Scale bars = 25 nm.

To extend the above studies of morphological controls from monometallic to bimetallic nanoparticles systems, Satyavolu et al.[16] screened four homo-oligo nucleotide sequences, A10, G10, C10, T10 for Pd-Au core-shell structural synthesis using Pd cubic seed. As a result, A10 produced rhombicuboctahedron shape, and C10 produced cuboctahedron shape, while G10 and

T10 promoted an undulated structure and a core-frame structure, respectively (Fig. 1.2b). The authors proposed that the final morphologies of the nanoparticles depend on the interaction of DNA molecules with both the seed surface and the precursor, which determines the deposition and diffusion rate of atoms on the surface. In the case of T10, because of its low binding affinity to both the precursor and the surface in comparison with the other sequences, the deposition rate of atoms was much faster than the diffusion rate of atoms. Therefore, the metal atoms would preferentially grow on the high-energy site (edge and vertices of cubic seed), which resulted in {100} facet exposed core-frame structure. On the other hand, C10 has a stronger binding affinity than T10, hence C10 could slow down the gold atom deposition rate by its surface passivation effect, as well as the interaction with precursor. In the presence of C10, the growth of nanoparticles was also initiated from the edge and vertices. However, because of the low deposition rate, the nanoparticles would eventually reach a thermodynamically more stable cuboctahedral morphology through atom diffusion. The growth in the presence of G10 and A10 adopted mechanisms that were more unique to the DNA sequences. As supported by circular dichroism, G10 could form G-quadruplex, which could passivate the surface to a larger extend. The formation of secondary structures led to island growth of the shell which eventually evolved into undulated structure. The growth in the presence of A10 adopted a sigmoidal growth curve as showed by the UV-Vis kinetic study. In addition, transmission electron microscopy (TEM) demonstrated that A10 would promote the self-nucleation of gold precursors to form smaller nanocrystals at the initial stage. Therefore, the authors proposed that the growth was achieved by the aggregation and Ostwald ripening of the smaller nanoparticles onto seed crystals. More recently, the same DNA sequences were utilized in a follow up study where a high-indexed Pd concave nanocube was used as the seed.[18] The role of the seed in a DNA-mediated synthesis was elucidated in this study.

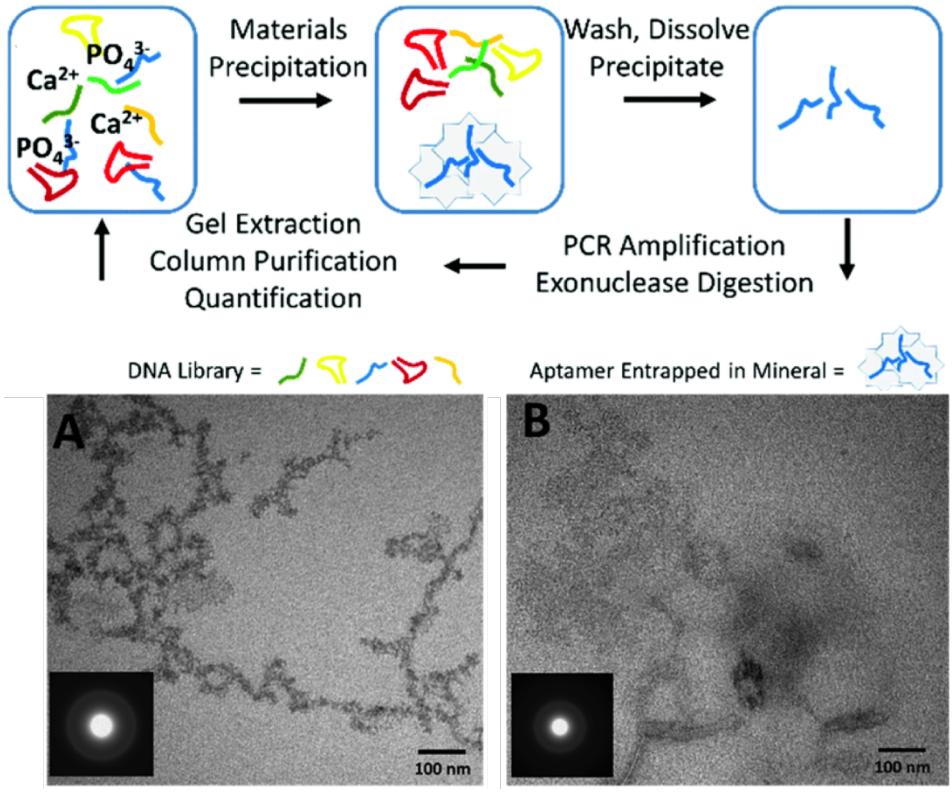


Figure 1.3: A generalized protocol of precipitation SELEX and TEM images of $CaCO_3$ formed in the presence of (A) 50 nM DNA sequence from the selection and (B) no DNA. Inset shows selected-area electron diffraction. Adapted from reference [31] with permission from The Royal Society of Chemistry.

In addition to screening the selected sequences for inorganic nanomaterial synthesis, DNA sequences can also be selected toward specific inorganic material surface using *in vitro* selection. *In vitro* selection is a combinatorial method conventionally used for selecting biomolecules that bind to specific molecular targets, where a random DNA library of 10^{14} to 10^{15} sequences are mixed with the target molecules, and DNA sequences that are bound to the targets would then be isolated and amplified by polymerase chain reaction (PCR). The selection cycle would be repeated under increasingly stringent conditions until the sequence with the highest binding affinity is identified.[19-20] DNA sequence selection toward inorganic nanomaterials could be achieved by

replacing the molecular target with target nanomaterials. For example, Morse and coworkers [21] performed a single round of DNA sequence selection on polycrystalline ZnO nanoparticles, and used sequencing to analyze the results. They showed that T30 has the strongest binding affinity for ZnO nanoparticles, and it could assist the synthesis of ZnO nanoparticles with an amorphous-crystalline core-shell structure. Furthermore, based on the binding affinity of DNA towards inorganic material surface, selection has also been performed based on in situ synthesis assay. Baillargeon et al.[22] used systematic evolution of ligands by exponential enrichment (SELEX) combined with precipitation assay to identify the DNA sequences that are specific for calcium phosphate. In this case, DNA directly participated in the nanomaterial formation process in selection and was incorporated into the final calcium phosphate structures, which were analyzed by sequencing (Fig. 1.3). The selected sequence was used for the synthesis of calcium phosphate nanoparticles. The resulting structure from selected DNA sequence is a loose network of weakly associated amorphous nanoparticles, whereas the structures synthesized without DNA sequence did not form the network (Fig. 1.3). The idea of using the ability to template nanomaterial synthesis as the criteria for selection is valuable in providing better predictability of the performance of selected sequence in the actual nanomaterial synthesis. There have been very limited reports about selection on metal nanomaterials. This could potentially be attributed to the strong non-specific interaction of metal surface and DNA sequences, which would generate high background noise and false positive signals.[20] Moreover, even in the reported case, the relative binding affinity of different DNA sequences towards inorganic materials surface is debatable. For example, oligo-C DNA has later been demonstrated to have stronger binding affinity towards ZnO than oligo-T DNA.[23-24] No facet specific DNA selection has been reported.

1.3 Sequence-specific control of inorganic nanomaterial morphologies by peptides

In comparison to DNA molecules, peptides contain more diverse functional groups and therefore have also been employed for various inorganic nanomaterial synthesis. For example, Tang and coworkers[25] used peptide R5 (SSKKSGSYSGSKGSKRRIL) for the synthesis of Au and Pt nanoparticles. As a result, when the synthesis was performed under lower metal-to-peptide ratios, both Au and Pt nanoparticles grew into spherical shapes, whereas higher metal-to-peptide ratios yielded nanoribbons or networked nanochains. In addition to peptides, peptoids, which are peptidomimetics whose side chains are appended to the nitrogen atom of the peptide backbone, rather than to the α-carbons, have also been studied for controlling the morphology of inorganic nanomaterials. Because peptoids do not contain backbone hydrogen bonding interactions found in peptides, using peptoids for controlling nanomaterials syntheses would allow the focus on the effect from the side chains instead of peptide bonds, potentially making the system less complicated and more predictable. Yan et al.[26] screened ten peptoids with different sequences containing different side chains for gold nanoparticle synthesis. The resulting morphologies varied from spherical to coral-shape, depending on the sequences used (Fig. 1.4A). By systematically varying the hydrophobicity, number of carboxylate and amino groups, and the side-chain positions of the peptoids, the authors found that side chains containing amino group, high hydrophobicity, as well as the specific arrangement of the hydrophobic groups were all critical elements in enhancing the binding affinity of peptoids towards gold nanoparticle surfaces. A mechanistic study on the nanoparticle growth was conducted with in situ TEM, molecular simulations and time-of-flight secondary ion mass spectrometry. As a result, the peptoid with higher binding affinity would induce the growth of distorted gold nanorods, which aggregated into spherical coral-shaped particles. In contrast, the peptoids with lower binding affinity could not stabilize the high surface

energy of the aggregated cluster of distorted nanorods. Therefore, the particles would relax to spheres. Furthermore, the authors also demonstrated the same principles can be applied to the controlled synthesis of coral-shaped Pd- and Pt- nanoparticles.

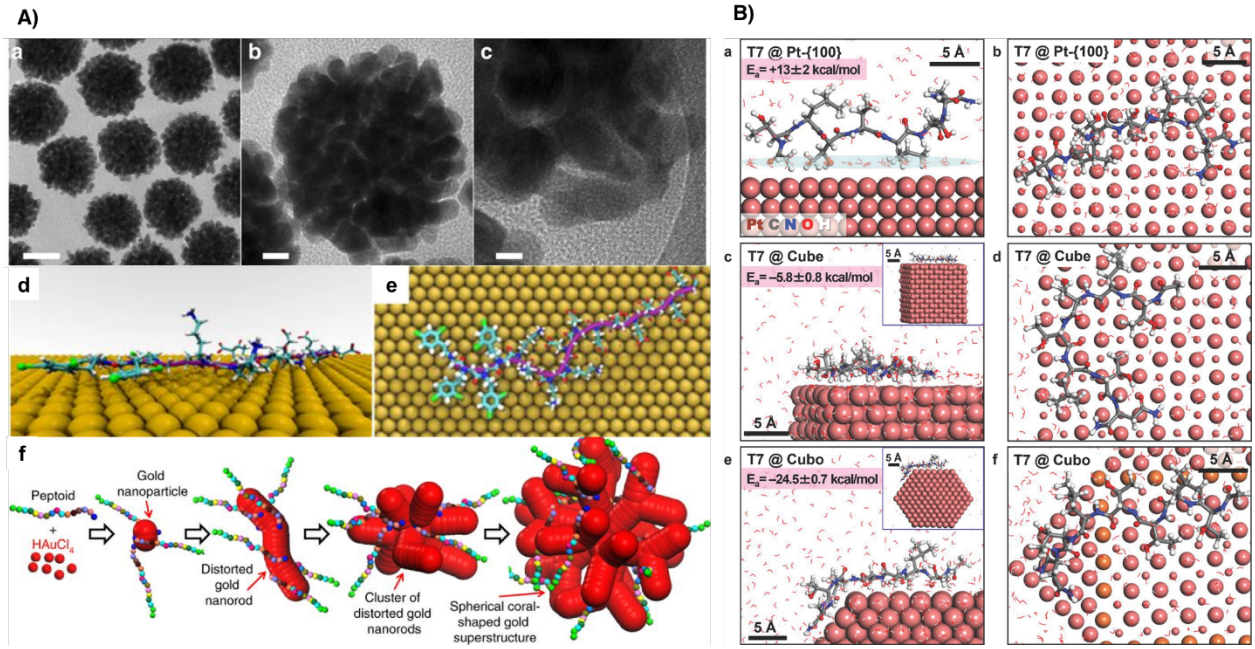


Figure 1.4: Sequence-specific control of inorganic nanomaterials morphologies by peptides. A) a-c TEM image of Pep-1-induced formation of spherical coral-shaped gold nanoparticles. d, e Representative structures of Pep-1 adsorbed at the aqueous Au (111) interface predicted from REST-MD simulations. f Mechanism of peptide induced formation of spherical coral-shaped gold nanoparticles. Adapted with permission from reference [35]. Copyright 2018 Nature Publishing Group. B) Differences in average binding conformation of a single peptide T7 on extended Pt {100} surfaces, cubes, and cuboctahedra according to molecular dynamics simulation. Adapted with permission from reference [41]. Copyright 2015, John Wiley and Sons.

Instead of screening different peptide sequences for morphological controls, specific peptide sequence could also be selected for inorganic nanomaterial synthesis by phage display. In the phage display method, randomized DNA sequences were inserted into the phage virus genome,

which would create the peptide library by expressing the corresponding peptides on the coat protein of the phage. Then a target surface would be brought in contact to the phage. The unbound or weakly bound phage would be washed away whereas the tightly bound phage would be retained, amplified and sequenced to find the corresponding sequences that code for the peptides.[27] This method allows for the simultaneous testing of up to 10^{11} different peptides.[28] This technique has been used to identify peptide sequences that can specifically bind to metals, oxides and semiconductors[29-30]. Furthermore, an improvement of phage display method has enabled facet-specific peptide selection toward certain materials. For example, Chiu et al.[31] selected peptides that bind either Pt-{100} or Pt-{111} by using Pt cubes and Pt octahedrons as targets in phage display selection. The selected peptides could produce Pt cubes and Pt tetrahedrons correspondingly. A follow up study on the recognition mechanism of the peptides on different Pt nanoparticle facets was performed using molecular dynamics simulation (MD).[32] The simulated results showed excellent matching between peptide T7 and the epitaxial sites on the edge of {100} facet (Fig. 1.4B). In addition, the concentration of the T7 peptide used during nanoparticle synthesis also affected the relative coverage of peptide sequence on different facets. The experimental results demonstrated that only intermediate concentration of T7 can lead to high yields of Pt nanocubes, which agreed with the simulated results. In a special case, as an extension of phage display method, Mao and coworkers[33] selected a peptide sequence that specifically binds to tetragonal barium titanate ($BaTiO_3$) using phage display and then expressed the peptide sequence on the phage. The peptide was then used as the direct template for in situ synthesis of $BaTiO_3$ polycrystalline nanowires.

1.4 Sequence-specific interaction with nanomaterials surface

It is generally believed that the interaction of biomolecules with inorganic nanomaterials shares some common features with that of conventional capping agents such as small organic molecules. Both could modify the surface energy and surface structure of inorganic nanomaterials during the growth process. However, the modification by biomolecules is sequence dependent. For example, DNA could interact with gold nanoparticles through ring nitrogen, exocyclic amino and keto groups of the nucleobases. The exocyclic amino group and the ring nitrogen in adenine enables exceptionally high adsorption affinity towards gold surface even in the range of covalent attachment.[34] On the other hand, the delocalization of the lone pair electrons of the imine group in cytosine and guanine contributed to their non-covalent attachment onto the gold nanoparticles. Finally, thymine is thought to have the lowest affinity towards gold surface among all nucleobases, because it does not have imine group.[35] In addition to the aforementioned interactions, DNA could also interact with the gold surface through electrostatic and hydrophobic forces, which depend highly on the protonation state of the nucleobases and conformation of DNA molecules with different sequences.[34] As a result, DNA molecules with different sequences have different binding affinity as well as different mobility on the surface of gold nanoparticles, which affect the growth process of nanomaterials. For instance, Tan et al.[14] investigated DNA-mediated morphological evolution of gold nanoprism seeds into nonagon with rough surface, nonagon with smooth surface, hexagon, and six-pointed stars in the presence of A30, C30, G20 and T30, respectively (Fig. 1.5A). After characterizing the growth process of nanoparticles using various analytical methods including UV-vis, SEM, TEM, zeta potential, fluorescence, and cyclic voltammetry, the authors observed that the growth always started with the expansion of diameter of the prism seed, followed by the increase of thickness. The authors proposed that, in the first stage, the binding affinity and

concentration of DNA molecules with different sequences determined the desorption rate as well as the density of the DNA onto the seed. T30 has the lowest binding affinity for the gold surface, and therefore the incoming precursor could freely deposit on the seed surface and let the shape to fully develop into six-pointed star with the largest diameter amongst all four shapes. While A30, C30 and G20 have higher binding affinity than T30, those DNA molecules could stabilize the high-energy side facets (reentrant groves in the stacking defaults), thus kinetically trapped the intermediate morphologies during the shape evolution of AuNPs. And the stronger the affinity, the earlier the growth would be arrested. In the second stage, the growth in thickness depends on both the remaining precursor concentration and DNA mobility. The thickness of the nanoparticles in the second stage has an inverse trend with the diameter development in the first stage. The nanoparticles that grew larger in diameter in the first stage would consume more gold precursor than the nanoparticles that have smaller diameter. As a result, there would be less remaining gold precursor for thickness increase in the second stage for large nanoparticles. On the other hand, the roughness of the gold nanoparticles depends on the mobility of DNA sequences on gold surface. For example, because A30 has lower mobility than C30 on gold surface, A30 resulted in roughened nonagon, while C30 resulted in smooth nonagon.

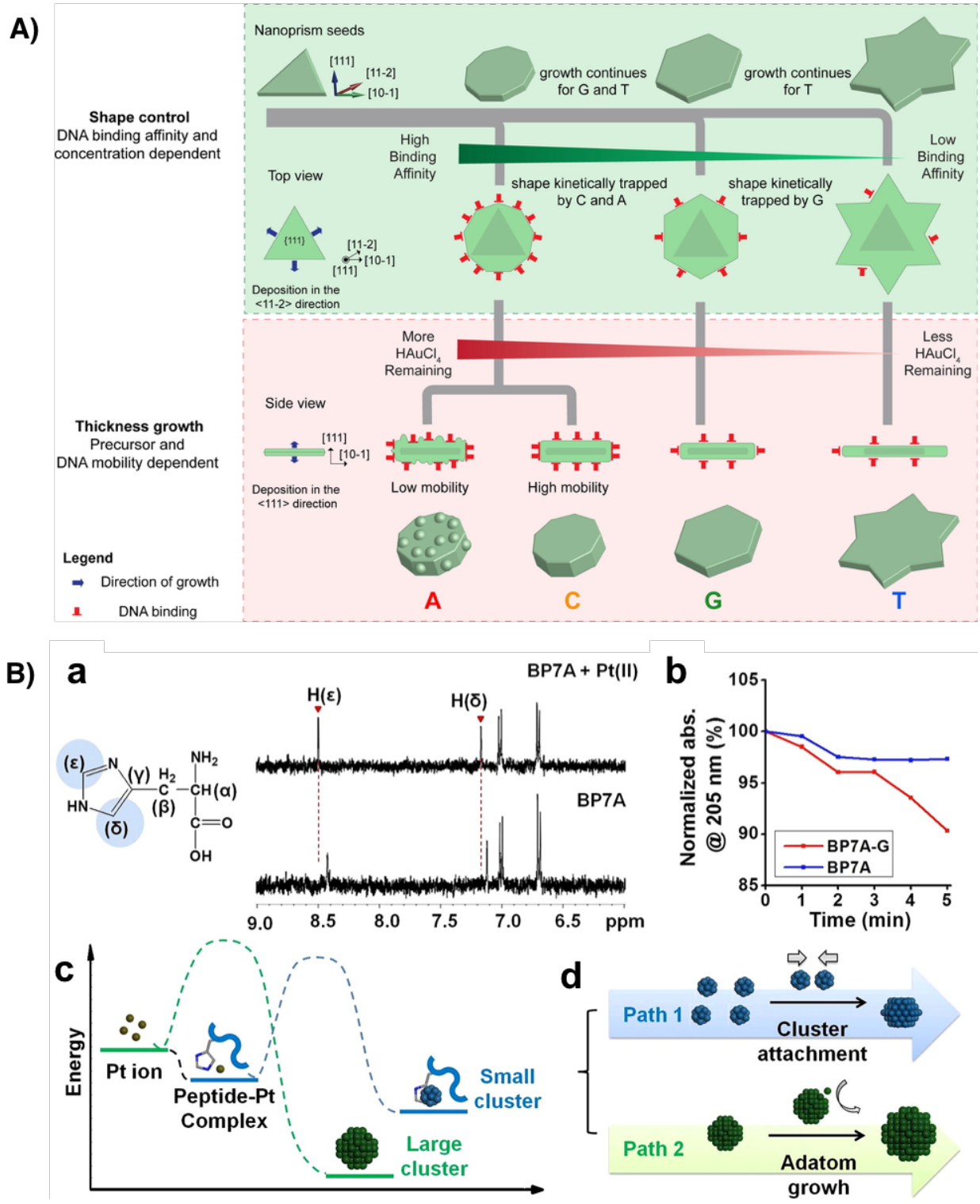


Figure 1.5: Mechanism for sequence-specific control of inorganic nanomaterials morphologies by DNA and peptides. A) Proposed mechanism of growth of Au nanoprisms controlled by

Figure 1.5 (cont.): DNA. Adapted with permission from reference [23], copyright 2015 American Chemical Society. B) Interaction of BP7A peptide with Pt precursor and cluster. a) NMR spectra of peptide-Pt(II) complex; b) UV vis spectra of K_2PtCl_4 reduction in the presence of BP7A and BP7A-G peptides; c) Scheme showing the complex formation between histidine-containing peptides and Pt ions and following Pt cluster formation. d) Scheme showing two possible NC growth pathways: cluster attachment and adatom deposition. Adapted with permission from reference [47], copyright 2014 American Chemical Society.

1.5 Sequence-specific interaction with precursor

In addition to sequence-specific interactions with inorganic nanomaterial surface, biomolecules could also interact with the precursor during the synthesis. Previous studies have demonstrated that certain biomolecule sequences could form complexes with metal ions or stabilize small clusters under various conditions.[36-38] Those complexes and clusters could also be important reaction intermediates in biomolecule-controlled synthesis of inorganic nanomaterials. For example, Ruan et al.[39] reported that the histidine residue in BP7A peptide could form complexes with Pt ions, which reduced the reduction rate of the Pt precursors and modified the growth pathway of Pt nanocrystals towards cluster attachment. The strong interaction between histidine and Pt ions and the preferential stabilization of {111} facets by BP7A peptide contributed to the formation of twinned seed in Pt nanocrystals.

The exact mechanism for nucleation and growth of inorganic nanomaterials is still debatable. In classical nucleation theory, nucleation and growth are mediated by monomer-by-monomer addition. However, in recent years, more and more studies have indicated an alternative nucleation pathway through cluster or particle addition.[40] Direct experimental evidence of the cluster intermediates captured during crystal formation is still rather limited. With the well-

controlled reaction kinetics and stabilization of clusters, biomolecule-controlled inorganic material nucleation and growth are very likely to adopt a non-classical nucleation pathway, and hence could be a model system to elucidate the unknown nucleation and growth mechanism. A close multidisciplinary collaboration involving chemistry, biology and physics is required for fully understand the mechanism for biomolecule sequence specific control of inorganic nanomaterial synthesis.

1.6 Properties resulting from the sequence-specific control

A major motivation behind exploring new synthetic routes to control morphologies of inorganic nanoparticles is the resultant physiochemical properties, which can be exploited in many applications including, but are not limited to, catalysis, optical spectroscopy and biological applications.[41] Since the synthetic condition using biomolecules are normally more benign or "green", the study is a step towards the production of more sustainable materials that can potentially replace existing materials that are otherwise synthesized under harsher conditions.

1.7 Optical properties including surface enhanced Raman spectroscopy (SERS)

The morphology of plasmonic metal nanoparticles such as Au and Ag strongly determines the optical absorption cross-section of the nanoparticles. The Lu lab has reported the synthesis of DNA-sequence dependent morphology control of both Au[42] and Pd@Au[18] nanoparticles, which display sequence-dependent plasmonic particles. The Pd@Au particles showed different enhancement factors as SERS probes for 4-mercaptobenzenethiol[18] (Fig. 1.6a). Using a slightly different synthetic approach, Nam and coworkers[43] were able to manipulate "nano-gaps" by anchoring thiolated DNA with difference sequences onto the Au seed to control the shell growth. They reported the relationships between the width of the interior plasmonic nanogap and surface-enhanced Raman scattering efficiencies. On the other hand, Pu et al.[44] reported a protein-mediated

synthesis of Ag nanoparticles that exhibited specific localized surface plasmon resonance (LSPR) for each protein used. This method involved multiple proteins that produced multiple readouts of LSPR signals of AgNPs to further construct sensor arrays for pattern recognition of proteins.

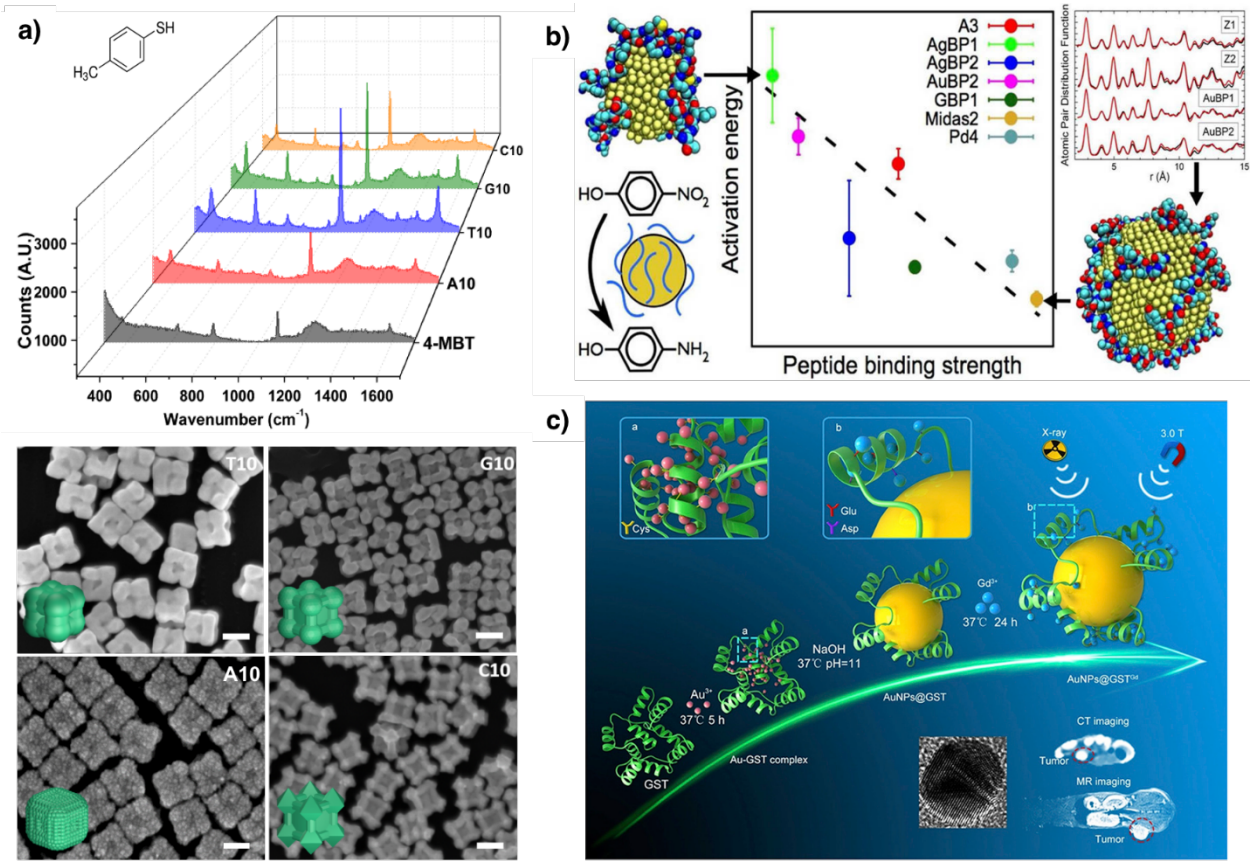


Figure 1.6: Examples of sequence-specific properties of nanomaterials with different morphologies. a) SERS spectra of 4-MBT functionalized on the DNA-mediated nanoparticles and Raman spectra of a concentrated solution of 4-MBT. The corresponding SEM images of the DNA mediated Pd@Au core shell nanoparticles. Scale bar = 100 nm. Adapted with permission from reference [27], copyright 2018 Tsinghua University Press and Springer-Verlag GmbH Germany, part of Springer Nature. b) Peptide sequence dependent structure-function relationship in peptide mediated AuNP synthesis. The Au NPs exhibit varying degrees of catalytic activity for 4-

Figure 1.6 (cont.): nitrophenol reduction. The pair distribution function (PDF) analysis revealed sequence-dependent differences in structural order at the NP surface. Adapted with permission from reference [55], copyright 2016 American Chemical Society c) Schematic illustration of GST-mediated AuNPs that anchor Gd ions and biomedical imaging functions of material as a MR/CT dual-modal imaging contrast agent. Adapted with permission from reference [58], copyright 2018 Elsevier Ltd.

1.8 Catalytic properties

The synthesis of nanomaterials with different morphologies through sequence-specific control can give rise to the ability to tune catalytic efficiencies of these materials. For example, Bedford et al.[45] have demonstrated that peptides with different sequences play an important role in determining the catalytic efficiencies of Pd nanocatalysts for the Stille coupling reaction and olefin hydrogenation. These Pd nanoparticles were synthesized in the presence of combinatorially derived peptides that influence the surface disorder of the nanoparticles. Atomic pair distribution function (PDF) analysis of high-energy X-ray diffraction (HE-XRD) patterns and X-ray absorption fine-structure spectroscopy (XAFS) were used to probe atomic-scale structure details of peptide-derived Pd nanocatalysts, backed by MD simulation. The overall analysis shows clear atomic-scale structural differences associated with changes in the peptide sequences. In agreement to this result, sequence-specific peptides have been used for metal composition control in Pd-Au bimetallic nanoparticles to achieve ultimate tunability of catalytic efficiency in electrocatalytic methanol oxidation reactions[46]. Similar effects were observed in the case of 4-nitrophenol reduction by Au nanoparticles synthesized in the presence of different peptide sequences.[47] (Fig. 1.6b).

1.9 Biomedical imaging and nanomedicine

Given that the nanoparticle surfaces are functionalized with biomolecules such as DNA, peptide or proteins, the biocompatibility of the particles increases compared to nanoparticles synthesized with other ligands. The DNA-mediated Ag nanoparticles have been utilized for antimicrobial activity in the past. On the other hand, peptide-coated nanomaterials have been used as implant materials, for regenerative medicine, and for medical imaging.[48] Wang et al.[49] reported BSA protein mediated synthesis of Au core/shell nanoparticles loaded with drugs, which were further used for simultaneous CT imaging and drug delivery. Similarly, Zhang and coworkers[50] reported glutathione S-transferase (GST) protein mediated in-situ synthesis of Au NPs. The protein also had the functional groups to anchor Gd ions and this set-up enabled them to perform *in vivo* MR and CT imaging (Fig. 6c). Peptide nanofibers have also been used for the synthesis of Ag nanoparticles, which were utilized for antimicrobial applications.[51]

1.10 Summary and outlook

As discussed in the sections above, impressive progress has been made in the past few years toward sequence-specific controlled morphologies of inorganic nanomaterials. The programmability and unique chemical and structural characteristics of biomolecules allow screening of sequences to direct the growth of nanostructures into specific morphology, which in some cases cannot be achieved by conventional methods using inorganic anions or organic molecules. To complement the rational design method, combinatorial molecular selection or evolution method has also been developed to discover specific sequences towards different inorganic material surfaces as well as specific nanostructure morphology. Each of the two methods has its own strengths and limitations.

Screening of biomolecules for nanomaterials synthesis is the most straight forward method. It starts with a relatively small library (usually tens to hundreds of sequences). Each sequence is assayed separately, where in situ nanomaterial synthesis is performed in each assay. The sequences that produce desired nanostructures will be retained and the material characterized further. Screening is performed exactly in the synthesis condition. Therefore, it has better predictability for the actual performance of biomolecules in nanomaterial synthesis. However, the throughput of screening is relatively low (several to hundreds of sequences). Each sequence need to be assayed separately, and each synthesis may take some time to finish, which makes this method time consuming and labor intensive. Moreover, because of the relatively small library, the best sequence could be left out considering the numerous combinations of biomolecule building blocks.

Selection, on the other hand, enables examination of a much larger library (10^{11} to 10^{15} sequences) where all sequences are mixed together and assayed simultaneously. For most studies so far, selection is essentially a binding assay, where the sequence with the strongest binding affinity will be selected. However, capping agent assisted nanocrystal growth process is more than a simple binding event, it involves a dynamic adsorption and desorption process of molecules on the surface. Any shapes and sizes of the nanocrystals used as target in the selection is eventually a snapshot of a growing crystal and therefore the affinity for those targets does not guarantee the final yield of the same crystal. For example, a molecule with too strong an affinity might quench the crystal growth at a much earlier time point, which can result in crystals that never evolve into the desired shape. Moreover, the affinity-based selection has the interference from non-sequence specific binding to nanomaterial surface, such as electrostatic interaction, and this issue is especially serious with inorganic materials .[20] If the background noise is too high and the difference between different sequences is too little, it is highly possible to generate a false positive result.

Additionally, most of the reported cases are on metal nanomaterial synthesis. The generality of these methods need to be demonstrated on other nanomaterials. New methods that have combine the benefits of both better predictability in screening and high throughput in selection should be developed to accelerate discovery of new biomolecules with sequences that can control novel morphologies.

The successful cases of using rationally designed biomolecules to control synthesis toward certain nanostructure morphology is still relatively rare. Most of the studies are based on trial and error. Mechanistic insight is essential in truly achieving sequence specific controlled synthesis of inorganic nanomaterials. However, challenges remain in multiple perspectives in understanding biomolecule-inorganic nanomaterial interaction in the synthesis. For biomolecules, different sequences generate more than one conformation or three-dimensional structures, and they often dynamically interchange between each other in aqueous solution. For inorganic material surfaces, varies facets as well as lattice defects, together with the limited choice of atomic level characterization technique made their structures difficult to characterize and simulate. Therefore, these factors make understanding biomolecule-inorganic interface difficult. Currently, direct experimental tool to resolve the configuration and packing of biomolecules on inorganic nanomaterial surfaces is quite rare.[3] We have to largely rely on computational tool to understand and predict the behavior of biomolecules on inorganic surfaces.[48] Moreover, in the actual nanomaterial synthesis, the surface of the growing crystal is always changing, and the interaction of biomolecules with precursors and other biomolecules should also be considered. Both experimental and computational methods need to be developed in order to provide greater insight of biomolecule controlled inorganic nanomaterial synthesis, which would eventually help us to obtain programmable nanomaterial morphologies using different biomolecule sequences.

1.11 References

1. Roth, K. L.; Geng, X.; Grove, T. Z., Bioinorganic Interface: Mechanistic Studies of Protein-Directed Nanomaterial Synthesis. *The Journal of Physical Chemistry C* **2016,** *120* (20), 10951-10960.

2. Zan, G.; Wu, Q., Biomimetic and Bioinspired Synthesis of Nanomaterials/Nanostructures. *Adv. Mater.* **2016,** *28* (11), 2099-2147.

3. Xia, Y.; Xia, X.; Peng, H.-C., Shape-Controlled Synthesis of Colloidal Metal Nanocrystals: Thermodynamic versus Kinetic Products. *Journal of the American Chemical Society* **2015,** *137* (25), 7947-7966.

4. Ramezani‐Dakhel, H.; Ruan, L.; Huang, Y.; Heinz, H., Molecular Mechanism of Specific Recognition of Cubic Pt Nanocrystals by Peptides and of the Concentration‐Dependent Formation from Seed Crystals. *Adv. Funct. Mater.* **2015,** *25* (9), 1374-1384.

5. Heinz, H.; Ramezani-Dakhel, H., Simulations of inorganic-bioorganic interfaces to discover new materials: insights, comparisons to experiment, challenges, and opportunities. *Chem. Soc. Rev.* **2016,** *45* (2), 412-448.

6. Carnerero Jose, M.; Jimenez‐Ruiz, A.; Castillo Paula, M.; Prado‐Gotor, R., Covalent and Non‐Covalent DNA–Gold‐Nanoparticle Interactions: New Avenues of Research. *ChemPhysChem* **2016,** *18* (1), 17-33.

7. Zheng, X. T.; Xu, H. V.; Tan, Y. N., Bioinspired Design and Engineering of Functional Nanostructured Materials for Biomedical Applications. In *Advances in Bioinspired and Biomedical Materials Volume 2*, American Chemical Society: 2017; Vol. 1253, pp 123-152.

8. Li, Y.; Tang, Z.; Prasad, P. N.; Knecht, M. R.; Swihart, M. T., Peptide-mediated synthesis of gold nanoparticles: effects of peptide sequence and nature of binding on physicochemical properties. *Nanoscale* **2014,** *6* (6), 3165-3172.

9. Brown, K. A.; Park, S.; Hamad-Schifferli, K., Nucleotide−Surface Interactions in DNA-Modified Au−Nanoparticle Conjugates: Sequence Effects on Reactivity and Hybridization. *The Journal of Physical Chemistry C* **2008,** *112* (20), 7517-7521.

10. Ruan, L.; Ramezani-Dakhel, H.; Chiu, C.-Y.; Zhu, E.; Li, Y.; Heinz, H.; Huang, Y., Tailoring Molecular Specificity Toward a Crystal Facet: a Lesson From Biorecognition Toward Pt{111}. *Nano Lett.* **2013,** *13* (2), 840-846.

11. Wang, Z.; Zhang, J.; Ekman, J. M.; Kenis, P. J. A.; Lu, Y., DNA-Mediated Control of Metal Nanoparticle Shape: One-Pot Synthesis and Cellular Uptake of Highly Stable and Functional Gold Nanoflowers. *Nano Lett.* **2010,** *10* (5), 1886-1891.

12. Wang, Z.; Tang, L.; Tan Li, H.; Li, J.; Lu, Y., Discovery of the DNA "Genetic Code" for Abiological Gold Nanoparticle Morphologies. *Angew. Chem. Int. Ed.* **2012,** *51* (36), 9078-9082.

13. Wang, Z.; Bharathi, M. S.; Hariharaputran, R.; Xing, H.; Tang, L.; Li, J.; Zhang, Y.-W.; Lu, Y., pH-Dependent Evolution of Five-Star Gold Nanostructures: An Experimental and Computational Study. *ACS Nano* **2013,** *7* (3), 2258-2265.

14. Tan, L. H.; Yue, Y.; Satyavolu, N. S. R.; Ali, A. S.; Wang, Z.; Wu, Y.; Lu, Y., Mechanistic Insight into DNA-Guided Control of Nanoparticle Morphologies. *JACS* **2015,** *137* (45), 14456-14464.

15. Wu, J.; Tan, L. H.; Hwang, K.; Xing, H.; Wu, P.; Li, W.; Lu, Y., DNA Sequence-Dependent Morphological Evolution of Silver Nanoparticles and Their Optical and Hybridization Properties. *JACS* **2014,** *136* (43), 15195-15202.

16. Satyavolu, N. S. R.; Tan, L. H.; Lu, Y., DNA-Mediated Morphological Control of Pd–Au Bimetallic Nanoparticles. *JACS* **2016,** *138* (50), 16542-16548.

17. Song, T.; Tang, L.; Tan Li, H.; Wang, X.; Satyavolu Nitya Sai, R.; Xing, H.; Wang, Z.; Li, J.; Liang, H.; Lu, Y., DNA-Encoded Tuning of Geometric and Plasmonic Properties of Nanoparticles Growing from Gold Nanorod Seeds. *Angew. Chem. Int. Ed.* **2015,** *54* (28), 8114-8118.

18. Satyavolu, N. S. R.; Pishevaresfahani, N.; Tan, L. H.; Lu, Y., DNA-encoded morphological evolution of bimetallic Pd@Au core-shell nanoparticles from a high-indexed core. *Nano Research* **2018**.

19. McGhee, C. E.; Loh, K. Y.; Lu, Y., DNAzyme sensors for detection of metal ions in the environment and imaging them in living cells. *Curr. Opin. Biotechnol.* **2017,** *45*, 191-201.

20. Zhou, Y.; Huang, Z.; Yang, R.; Liu, J., Selection and Screening of DNA Aptamers for Inorganic Nanomaterials. *Chemistry – A European Journal* **2017,** *24* (11), 2525-2532.

21. Bawazer, L. A.; Newman, A. M.; Gu, Q.; Ibish, A.; Arcila, M.; Cooper, J. B.; Meldrum, F. C.; Morse, D. E., Efficient Selection of Biomineralizing DNA Aptamers Using Deep Sequencing and Population Clustering. *ACS Nano* **2014,** *8* (1), 387-395.

22. Baillargeon, K. R.; Meserve, K.; Faulkner, S.; Watson, S.; Butts, H.; Deighan, P.; Gerdon, A. E., Precipitation SELEX: identification of DNA aptamers for calcium phosphate materials synthesis. *Chem. Commun.* **2017,** *53* (6), 1092-1095.

23. Lu, C.; Huang, Z.; Liu, B.; Liu, Y.; Ying, Y.; Liu, J., Poly‐cytosine DNA as a High‐Affinity Ligand for Inorganic Nanomaterials. *Angew. Chem. Int. Ed.* **2017,** *56* (22), 6208-6212.

24. Ma, L.; Liu, B.; Huang, P.-J. J.; Zhang, X.; Liu, J., DNA Adsorption by ZnO Nanoparticles near Its Solubility Limit: Implications for DNA Fluorescence Quenching and DNAzyme Activity Assays. *Langmuir* **2016,** *32* (22), 5672-5680.

25. Wang, Q.; Tang, Z.; Wang, L.; Yang, H.; Yan, W.; Chen, S., Morphology Control and Electro catalytic Activity towards Oxygen Reduction of Peptide-Templated Metal Nanomaterials: A Comparison between Au and Pt. *ChemistrySelect* **2016,** *1* (18), 6044-6052.

26. Yan, F.; Liu, L.; Walsh, T. R.; Gong, Y.; El-Khoury, P. Z.; Zhang, Y.; Zhu, Z.; De Yoreo, J. J.; Engelhard, M. H.; Zhang, X.; Chen, C.-L., Controlled synthesis of highly-branched plasmonic gold nanoparticles through peptoid engineering. *Nature Communications* **2018,** *9* (1), 2327.

27. Chiu, C.-Y.; Ruan, L.; Huang, Y., Biomolecular specificity controlled nanomaterial synthesis. *Chem. Soc. Rev.* **2013,** *42* (7), 2512-2527.

28. Corra, S.; Shoshan, M. S.; Wennemers, H., Peptide mediated formation of noble metal nanoparticles—controlling size and spatial arrangement. *Curr. Opin. Chem. Biol.* **2017,** *40*, 138-144.

29. Rawlings, A. E.; Bramble, J. P.; Tang, A. A. S.; Somner, L. A.; Monnington, A. E.; Cooke, D. J.; McPherson, M. J.; Tomlinson, D. C.; Staniland, S. S., Phage display selected magnetite interacting Adhirons for shape controlled nanoparticle synthesis. *Chemical Science* **2015,** *6* (10), 5586-5594.

30. You, F.; Yin, G.; Pu, X.; Li, Y.; Hu, Y.; Huang, Z.; Liao, X.; Yao, Y.; Chen, X., Biopanning and characterization of peptides with Fe3O4 nanoparticles-binding capability via phage display random peptide library technique. *Colloids and Surfaces B: Biointerfaces* **2016,** *141*, 537-545.

31. Chiu, C.-Y.; Li, Y.; Ruan, L.; Ye, X.; Murray, C. B.; Huang, Y., Platinum nanocrystals selectively shaped using facet-specific peptide sequences. *Nature Chemistry* **2011,** *3*, 393.

32. Ramezani-Dakhel, H.; Ruan, L.; Huang, Y.; Heinz, H., Molecular Mechanism of Specific Recognition of Cubic Pt Nanocrystals by Peptides and of the Concentration-Dependent Formation from Seed Crystals. *Adv. Funct. Mater.* **2015,** *25* (9), 1374-1384.

33. Li, Y.; Cao, B.; Yang, M.; Zhu, Y.; Suh, J.; Mao, C., Identification of Novel Short BaTiO3-Binding/Nucleating Peptides for Phage-Templated in Situ Synthesis of BaTiO3 Polycrystalline Nanowires at Room Temperature. *ACS Applied Materials & Interfaces* **2016,** *8* (45), 30714-30721.

34. Koo, K. M.; Sina, A. A. I.; Carrascosa, L. G.; Shiddiky, M. J. A.; Trau, M., DNA–bare gold affinity interactions: mechanism and applications in biosensing. *Analytical Methods* **2015,** *7* (17), 7042-7054.

35. Carnerero, J. M.; Jimenez-Ruiz, A.; Castillo, P. M.; Prado-Gotor, R., Covalent and Non-Covalent DNA-Gold-Nanoparticle Interactions: New Avenues of Research. *Chemphyschem* **2017,** *18* (1), 17-33.

36. Petty, J. T.; Zheng, J.; Hud, N. V.; Dickson, R. M., DNA-Templated Ag Nanocluster Formation. *JACS* **2004,** *126* (16), 5207-5212.

37. Kondo, J.; Tada, Y.; Dairaku, T.; Hattori, Y.; Saneyoshi, H.; Ono, A.; Tanaka, Y., A metallo-DNA nanowire with uninterrupted one-dimensional silver array. *Nature Chemistry* **2017,** *9*, 956.

38. Weng, B.; Lu, K.-Q.; Tang, Z.; Chen, H. M.; Xu, Y.-J., Stabilizing ultrasmall Au clusters for enhanced photoredox catalysis. *Nature Communications* **2018,** *9* (1), 1543.

39. Ruan, L.; Ramezani-Dakhel, H.; Lee, C.; Li, Y.; Duan, X.; Heinz, H.; Huang, Y., A Rational Biomimetic Approach to Structure Defect Generation in Colloidal Nanocrystals. *ACS Nano* **2014,** *8* (7), 6934-6944.

40. De Yoreo, J. J.; Gilbert, P. U.; Sommerdijk, N. A.; Penn, R. L.; Whitelam, S.; Joester, D.; Zhang, H.; Rimer, J. D.; Navrotsky, A.; Banfield, J. F.; Wallace, A. F.; Michel, F. M.; Meldrum, F. C.; Colfen, H.; Dove, P. M., CRYSTAL GROWTH. Crystallization by particle attachment in synthetic, biogenic, and geologic environments. *Science* **2015,** *349* (6247), aaa6760.

41. Walsh, T. R., Pathways to Structure–Property Relationships of Peptide–Materials Interfaces: Challenges in Predicting Molecular Structures. *Acc. Chem. Res.* **2017,** *50* (7), 1617-1624.

42. Song, T.; Tang, L.; Tan Li, H.; Wang, X.; Satyavolu Nitya Sai, R.; Xing, H.; Wang, Z.; Li, J.; Liang, H.; Lu, Y., DNA‐Encoded Tuning of Geometric and Plasmonic Properties of Nanoparticles Growing from Gold Nanorod Seeds. *Angew. Chem. Int. Ed.* **2015,** *54* (28), 8114-8118.

43. Oh, J.-W.; Lim, D.-K.; Kim, G.-H.; Suh, Y. D.; Nam, J.-M., Thiolated DNA-Based Chemistry and Control in the Structure and Optical Properties of Plasmonic Nanoparticles with Ultrasmall Interior Nanogap. *JACS* **2014,** *136* (40), 14052-14059.

44. Pu, F.; Ran, X.; Guan, M.; Huang, Y.; Ren, J.; Qu, X., Biomolecule-templated photochemical synthesis of silver nanoparticles: Multiple readouts of localized surface plasmon resonance for pattern recognition. *Nano Research* **2017**.

45. Bedford, N. M.; Ramezani-Dakhel, H.; Slocik, J. M.; Briggs, B. D.; Ren, Y.; Frenkel, A. I.; Petkov, V.; Heinz, H.; Naik, R. R.; Knecht, M. R., Elucidation of Peptide-Directed Palladium Surface Structure for Biologically Tunable Nanocatalysts. *ACS Nano* **2015,** *9* (5), 5082-5092.

46. Bedford, N. M.; Showalter, A. R.; Woehl, T. J.; Hughes, Z. E.; Lee, S.; Reinhart, B.; Ertem, S. P.; Coughlin, E. B.; Ren, Y.; Walsh, T. R.; Bunker, B. A., Peptide-Directed PdAu Nanoscale Surface Segregation: Toward Controlled Bimetallic Architecture for Catalytic Materials. *ACS Nano* **2016,** *10* (9), 8645-8659.

47. Bedford, N. M.; Hughes, Z. E.; Tang, Z.; Li, Y.; Briggs, B. D.; Ren, Y.; Swihart, M. T.; Petkov, V. G.; Naik, R. R.; Knecht, M. R.; Walsh, T. R., Sequence-Dependent Structure/Function Relationships of Catalytic Peptide-Enabled Gold Nanoparticles Generated under Ambient Synthetic Conditions. *JACS* **2016,** *138* (2), 540-548.

48. Walsh, T. R.; Knecht, M. R., Biointerface Structural Effects on the Properties and Applications of Bioinspired Peptide-Based Nanomaterials. *Chem. Rev.* **2017,** *117* (20), 12641-12704.

49. Huang, H.; Yang, D.-P.; Liu, M.; Wang, X.; Zhang, Z.; Zhou, G.; Liu, W.; Cao, Y.; Zhang, W. J.; Wang, X., pH-sensitive Au–BSA–DOX–FA nanocomposites for combined CT imaging and targeted drug delivery. *International Journal of Nanomedicine* **2017,** *12*, 2829-2843.

50. Yang, W.; Wu, X.; Dou, Y.; Chang, J.; Xiang, C.; Yu, J.; Wang, J.; Wang, X.; Zhang, B., A human endogenous protein exerts multi-role biomimetic chemistry in synthesis of paramagnetic gold nanostructures for tumor bimodal imaging. *Biomaterials* **2018,** *161*, 256-269.

51. Pazos, E.; Sleep, E.; Rubert Pérez, C. M.; Lee, S. S.; Tantakitti, F.; Stupp, S. I., Nucleation and Growth of Ordered Arrays of Silver Nanoparticles on Peptide Nanofibers: Hybrid Nanostructures with Antimicrobial Properties. *JACS* **2016,** *138* (17), 5507-5510.

CHAPTER 2: QUANTITATIVE ANALYSIS OF DNA-MEDIATED FORMATION OF METAL NANOCRYSTALS[2]

2.1 Introduction

Metal nanocrystals have found wide applications in catalysis,[1] electronics,[2] sensing,[3] imaging[4] and medicine.[5] The structures of nanocrystals play important roles in determining their physical and chemical properties, which dictate their functions.[6-11] Predictive synthesis of metal nanocrystals towards desired structures thus holds the key to successful applications of nanomaterials. Despite the promise, predictive control over the structures of nanomaterials in solution-based synthesis is challenging. In a typical wet chemical synthesis, ion precursors are reduced by reductants to yield metal atoms to form nanocrystals. The choice of reagents and experimental conditions are largely empirical because it is difficult to quantify the outcome for each synthetic protocol. To achieve predictable synthesis of metal nanocrystals with desired structures, it is essential to attain quantitative understanding and then control the metal ion reduction process at the molecular level. Among various strategies, using a capping ligand is a versatile and proven method. Capping ligands may affect metal ion reduction in two different ways. On the one hand, the ligands can interact with the metal ion precursors through metal ion-ligand complexation,[12-13] which directly alters the electronic structure of the metal ion, and changes their reduction potentials and kinetics.[14] On the other hand, the ligands may interact with the surface of the crystals, altering the deposition and diffusion rate of adatoms, which changes

[2] Part of this chapter was published in "Wang, Y.; Counihan, M. J.; Lin, J. W.; Rodríguez-López, J.; Yang, H.; Lu, Y., Quantitative Analysis of DNA-Mediated Formation of Metal Nanocrystals. *Journal of the American Chemical Society* **2020,** *142* (48), 20368-20379."

the growth rate of different facets.[15-17] Despite many studies that explored different conditions, we are still far from comprehensive understanding of the role of the capping ligands in nanocrystal formation. Systematically tunable capping ligands that have predictable interactions with both the precursor and the surface of the nanocrystals[18] are indispensable for precisely controlling metal ion reduction and nanocrystal formation.

DNA is an especially promising class of capping ligand because of its well-defined molecular structures and conformations which are predictable from the sequences composed of the four-letter genetic codes. Single stranded DNA (ssDNA) with the same nucleotides or mixed nucleotides have been used in the synthesis of Au,[19-22] Ag[23] and Pd-Au bimetallic nanocrystals.[24] Nanocrystals with different morphologies formed when different DNA molecules were applied to the synthesis. To realize the full potential of DNA in predictive synthesis of nanostructures, one needs to understand the mechanism for DNA-controlled metal ion reduction and nanocrystal formation process.[21-22, 24] There is however, a general lack of quantitative experimental data, which is crucial in parameterizing the nanocrystal formation process. Quantitative description of the nanocrystal formation is challenging in not only DNA-mediated but also peptide- and other biomolecule-mediated processes.[25-26] Such challenge is largely due to the complexity of interactions between biomolecules and nanocrystals, as well as the limited characterization techniques available for probing the kinetic and thermodynamic parameters of the biomolecular-inorganic interface.[8, 18, 26] Therefore, quantitative experimental data and the corresponding theoretical frameworks are crucial in interpreting the mechanisms for biomolecule-controlled formation of nanocrystals.

DNA interacts with metal ions in definable binding modes. Metal cations generally interact with DNA either through electrostatic interaction of the negatively charged

phosphodiester backbone or the nitrogen and oxygen atoms on the bases.[27-28] Ag^+ is one of the few metal ions that interact with DNA exclusively through the nucleobases.[29-32] Therefore, DNA-controlled Ag^+ reduction and nanocrystal formation is an ideal model system to achieve quantitative understanding, because it eliminates possible interferences from the non-specific interactions with the phosphodiester backbones. Therefore, by using DNA-controlled formation of Au-Ag core-shell nanocrystals as a model system, we report herein quantitative analysis of the interaction between DNA and Ag^+ precursors, the reduction pathways of Ag^+, and the interaction between DNA and nanocrystal surfaces. We used the mechanistic insight of DNA controlled Ag^+ reduction kinetics to elucidate the morphological evolution of the resulting nanocrystals. This study demonstrated the predictive power of DNA sequence-specific control on the formation of metal nanocrystals.

2.2 Results and discussion

2.2.1 Morphology of DNA controlled metal nanocrystals

To understand the DNA-mediated growth of silver on gold nanoparticles (AuNPs) and their effects on the resulting morphologies, we chose to use Au decahedra with an average diameter of 74.8 ± 3.4 nm (Fig. 2.1) as the seed, based on a protocol reported previously.[33]

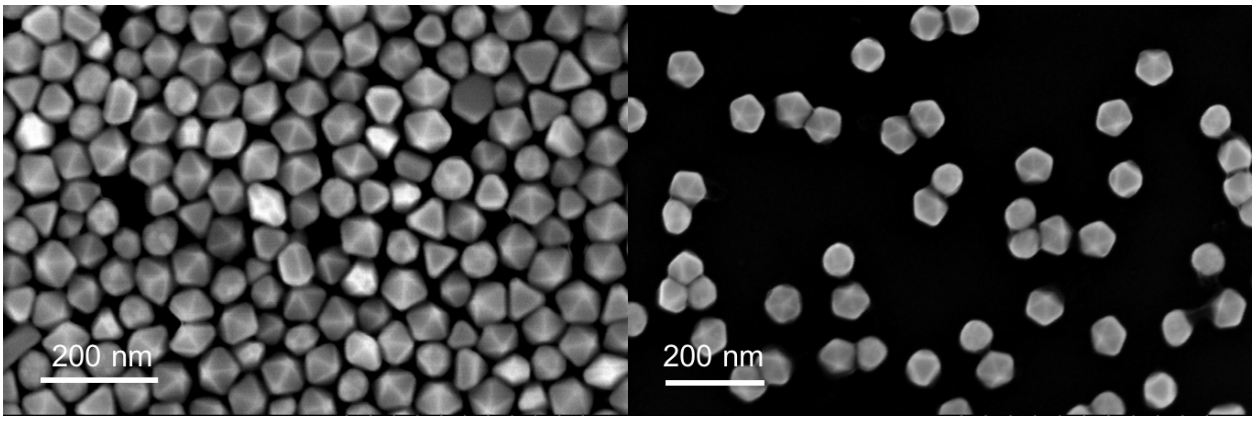


Figure 2.1: SEM images of Au decahedra seeds.

There are several advantages of selecting Au decahedra as the seed crystals. First, Au atoms have minimal lattice mismatch with that of Ag atoms.[34] Therefore, using AuNPs as the seed avoided lattice strain, which could result in complications in elucidating the mechanism of seed-mediated growth. Second, Au and Ag exhibit a large contrast under transmission electron microscope (TEM), making it easier to differentiate between the Au core and Ag shell of the hybrid or core-shell NPs. Finally, decahedra has a unique penta-twinned structure[35] that is expected to produce interesting defect-induced morphologies.[36]

To elucidate the effect of DNA molecules on the morphological growth of the NPs, ssDNA made of 20 units of all four nucleotides (C20, A20, T20, and G20) were used in the synthesis of Au-Ag core-shell NPs, while ascorbic acid was employed as the reducing agent and silver acetate (AgOAc) as the silver precursor. Overgrowth of Ag shells was found when C20, A20, or T20 was used as the DNA capping ligands, whereas no obvious overgrowth of Ag shell was detected when G20 was used (Fig. 2.2), which could be due to the effect of Ag^+ sequestering by a G-quadruplex.[23]

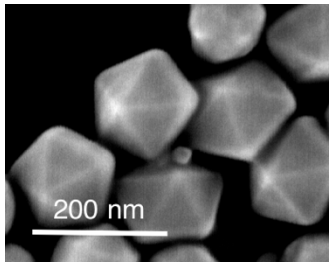


Figure 2.2: SEM image of the products of Ag^+ reduction on Au decahedra seeds with G20.

Fig. 2.3 shows the scanning electron microscope (SEM) images and TEM micrographs of Au-Ag core shell nanostructures synthesized with different DNA sequences. The SEM image shows uniform Ag shells grown on the decahedral Au seeds in the presence of C20 (Fig. 2.3a). The TEM images of Au-Ag NPs at representative time points were taken by sampling the NPs by

centrifugation to analyze their morphological evolution. The morphological evolution of the Ag shell grown with C20 followed the exact same structure as that of the Au decahedra core at all sampling time points (Fig. 2.3 b-e), which resulted in the enlarged decahedral shell that shared the common five-fold symmetrical axis with the core in the final structure (Fig. 2.3e). A20-mediated Ag^+ reduction generated a five-fold symmetrical face protruded structure (Fig. 2. 3f). The ten {111} facets of the decahedra core were symmetrically elevated, whereas the lateral growth along the equatorial plane was mostly restricted (Fig. 2.3). The overgrowth of the Ag shell in the presence of A20 initially took place on all five domains of the decahedron structure (Fig 2.3g, h), followed by a protrusion of each face (Fig. 2.3i), which resulted in the rounded particle morphology as viewed from the five-fold symmetrical axis (Fig. 2.3j, Fig. 2.4). More interestingly, the T20-mediated growth of Au-Ag NPs exhibited asymmetrical protrusions (Fig. 2.3k). The time-dependent TEM showed that the T20-mediated growth of the Ag shell selectively favored one of the five domains of the five-fold twin structure inherited from the Au decahedra seed (Fig. 2.3l-n), which led to the asymmetrical protrusion in the final structure (Fig. 2.3o). The automatic symmetry breaking in the T20-mediated nanostructure has rarely been reported previously.

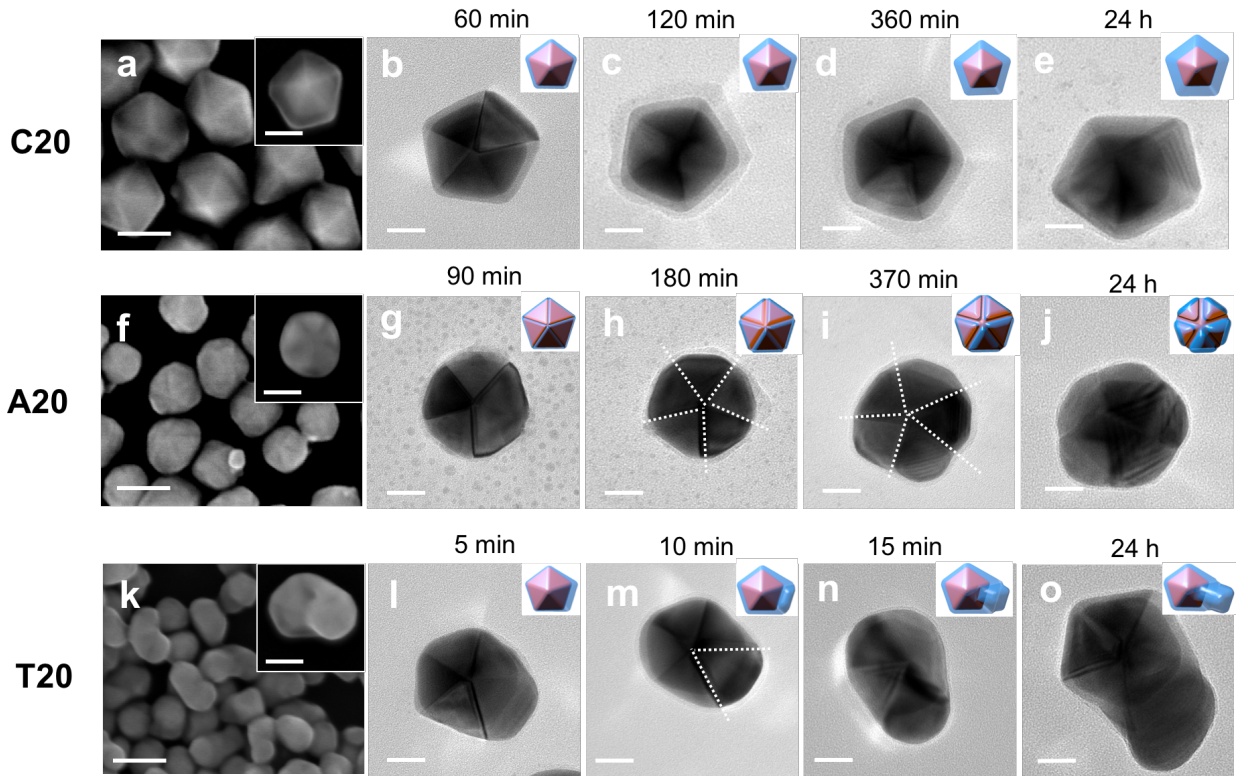


Figure 2.3: SEM images and TEM micrographs of Au-Ag core-shell NPs formed at different time points in the presence of C20 (a-e), A20 (f-j), and T20 (k-o), respectively. The insets in the SEM images are enlarged single particles. White dashed lines in TEM images highlight the twin boundary along which the Ag shells selectively grew. Scale bars are 50 nm in SEM (a,f,k) images and 20 nm in TEM micrographs (b-e, g-j, i-o).

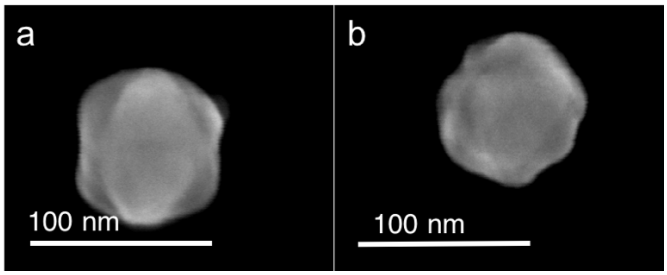


Figure 2.4: SEM images of Au-Ag nanostructures grown with A20 from different directions. (a) Parallel to the equatorial plane (b) a slanted angle between perspective in (a) and that of the five-fold symmetrical axis.

To elucidate the role of DNA in controlling the growth of the Au-Ag NPs towards different morphologies, we investigated these systems from three aspects. We first studied the interaction between DNA and Ag^+ precursors by quantifying the complexation between Ag^+ and DNA using electrochemical analysis. We then quantitatively analyzed the reduction of Ag^+ in the presence of DNA and derived the rate constants for different reduction pathways. Finally, we characterized the percentage of active surface sites remaining on the nanocrystals after DNA passivation. Our quantitative analyses suggest that DNA molecules of different sequences directly affect the kinetics and thermodynamics of Ag^+ reduction and nanocrystal formation processes, which lead to the sequence-specific atom deposition and NP formation that result in different morphologies.

2.2.2 Interaction between DNA and the Ag precursor:

Silver cation binds to the DNA nucleobases mostly by bridging two bases to function similarly to the hydrogen bonding interaction in Watson-Crick base pair.[31, 37-40] Silver-mediated bridging of base pairs can also take place in the presence of ssDNA containing the same nucleobases, particularly C-C.[41] Herein, the interaction between Ag^+ and the nucleobases in ssDNA can be described using a one-to-two binding model:

$$Ag^+ + 2Base \rightleftarrows Ag(Base)_2^+ \quad K_{eq} = \frac{[Ag(Base)_2^+]}{[Ag^+][Base]^2} \tag{1}$$

The reduction of Ag^+ in the presence of DNA could be described in the context of a metal-ligand equilibrium (2),[42] followed by a redox reaction (3).[43] We propose that the Ag^+ reduction went through the following reaction steps:

$$Ag(base)_2^+ \rightleftarrows Ag^+ + 2Base \tag{2}$$

$$Ag^+ + e \rightarrow Ag^0 \tag{3}$$

The reduction reaction (3) can be described using the Nernst equation:

$$E = E^O + \frac{RT}{F} \ln[Ag^+] \tag{4}$$

An effect of a metal-ligand complexation reaction (2) is to decrease the effective concentration of $[Ag^+]$ in equation (4). Thus, the reduction potential E of Ag^+ in (4) will be lower than that without the perturbation from DNA.[43]

To test the proposed model, we added solutions of A20, C20 and T20, respectively, into a 20 μM AgOAc solution and measured its open circuit potential (OCP) using a polycrystalline Ag working electrode (Fig. 2.5). The addition for each sequence was repeated three times and the error bar represents the standard deviation of the triplicated experiments. The final concentration of the DNA strands was 20 μM. The concentration of the DNA nucleobases was 400 μM, because each DNA strand contains 20 nucleobases. The concentration of nucleobases is in large excess (20 times) compared with that of the AgOAc solution. As shown in Fig. 2.5, the OCP in the presence of C20 dropped most significantly ($275.90 \pm 8.05\ m$V). A20 also caused the drop of OCP by $148.00 \pm 8.46\ m$V. Whereas the OCP only dropped by $3.30 \pm 0.96\ m$V in the presence of T20 sequence.

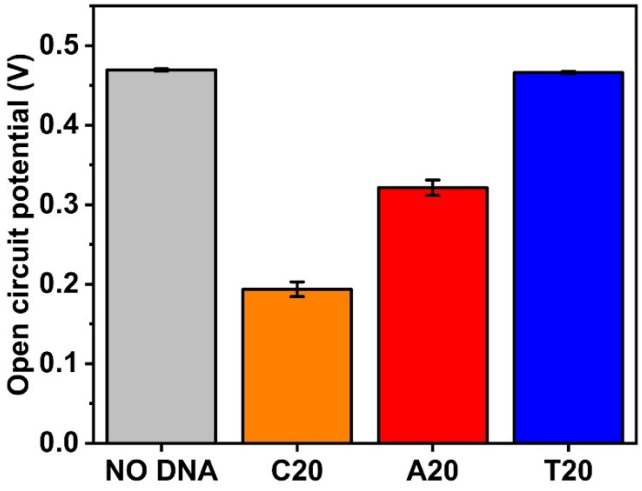


Figure 2.5: Open circuit potential of Ag^+ solution versus reference Ag/AgCl without and with adding DNA solutions of different sequences.

The drop in the *E* of the Ag^+/Ag^0 redox pair strongly suggests the complexation equilibrium (2). The degree of complexation varied between the DNA molecules of different sequences, which could be ascribed to the different binding ability between DNA nucleotides and Ag^+.[31, 40-41] Furthermore, the OCP could be converted into the concentration of C_O using the following Nernst equation:

$$E_{\mathrm{OCP}} = E^0{}_{\mathrm{Ag^+/Ag^0}} + \frac{RT}{F} \ln C_{Ag^+free} \qquad (5)$$

C_{Ag^+free} is the effective concentration of Ag^+ (unbound Ag^+) participating in the redox reaction and $\mathrm{E^0}_{\mathrm{Ag^+/Ag^0}}$ was determined experimentally using the OCP of 20 μM AgOAc solution without DNA. Using equation (5), the calculated Ag^+ concentration after DNA complexation was 4.37×10^{-4} μM for C20, 6.36×10^{-2} μM for A20 and 17.8 μM for T20. Because the total Ag^+ concentration in the solution was 20 μM, the remaining unbound Ag^+ concentration indicated that A20 and C20 sequestered more Ag^+ than T20 did. If we assume the concentration of free

Ag^+ equals the equilibrium concentration of Ag^+ ($[Ag^+]_{eq}$), the equilibrium constant between Ag^+ and DNA molecules of different sequences could be calculated as K_{eq} (C20) = 0.286 μM^{-2}, K_{eq} (A20) = 0.195μM^{-2} and K_{eq} (T20) = 7.72×10^{-7} μM^{-2}. Here are how the equilibrium constants were calculated:

$[Ag^+]_{eq}$ is determined from OCP measurements, $[Ag]_0$ and $[base]_0$ is the total concentration of Ag^+ and the base added into the solution. K_{eq} can be calculated using the following equation:

$$K_{eq}=\frac{[Ag(Base)_2^+]}{[Ag^+]\times[Base]^2} \quad (6)$$

Because $[base]_0$is 20 times that of $[Ag]_0$, assume the concentration of the base does not change significantly upon binding.

$$[base]_0 = [base]_{eq} \quad (7)$$

$$[Ag]_0 = [Ag^+]_{eq} + [Ag(base)_2^+]_{eq} \quad (8)$$

$$K_{eq}=\frac{[Ag]_0-[Ag^+]_{eq}}{[Ag^+]_{eq}\times[base]_0^{\,2}} \quad (9)$$

During the reduction process, the concentration of bases is no longer in great excess compared with that of Ag^+($[base]_0$: $[Ag]_0$= 2:1). Herein, an additional mass balance is considered.

$$[Ag]_0 = [Ag^+]_{eq} + [Ag(base)_2^+]_{eq} \quad (10)$$

$$[base]_0 = [base]_{eq} + 2[Ag(base)_2^+]_{eq} \quad (11)$$

$$K_{eq}=\frac{[Ag(base)_2^+]_{eq}}{[Ag^+]_{eq}\times[base]_{eq}} \quad (12)$$

The K_{eq} for T20 is six orders of magnitude smaller than those of A20 and C20, which indicates a weak binding between thymine and Ag^+.[41] An assumption of our model is that if the oxidized form of a redox couple is stabilized by a ligand, the free energy of the initial state of the

reduction reaction is lowered, hence the metal-ligand complex becomes difficult to be reduced. We also assumed that the DNA adsorption on the silver metal did not significantly affect the reduction potential of the Ag^+. We treated the DNA-complexed Ag^+ reduction as the dissociation of the complex and release of unbound Ag^+ followed by the reduction of the free Ag^+, which might not be the exact case if concerted reduction of the DNA-Ag^+ complex to free DNA and Ag^0 occurs. However, because the model only concerns the thermodynamic driving force of the reaction, the exact mechanistic path does not affect the conclusions drawn from the experimental result.[43]

2.2.3 DNA-mediated Ag^+ reduction pathways

The pathways of metal ion reduction determine the site and rate for metal atom generation and deposition. Hence studying reduction pathways of precursors is essential in mechanistic understanding of the growth pattern of metal nanocrystals. In seed-mediated synthesis, metal ion precursors could be reduced in two different pathways.[44] In the solution reduction pathway, metal ions are directly reduced by the reductant molecules in the solution. The corresponding reaction equation and rate expression of Ag^+ reduced by the reductant (Red), ascorbic acid, are as follows:

$$Ag^+ + \text{Red} \xrightarrow{k_1} Ag^0 + \text{Ox} \quad (13)$$

$$-\frac{d[Ag^+]}{dt} = k_1 [Ag^+] [\text{Red}] \quad (14)$$

k_1 is the rate constant for solution reduction.

In the surface reduction pathway, metal ions are first adsorbed onto the surface of the growing crystals, then reduced.[44-46]

$$Ag^0_n + Ag^+ + \text{Red} \xrightarrow{k_2} Ag^0_{n+1} + \text{Ox} \quad (15)$$

$$-\frac{d[Ag^+]}{dt} = k_2\,[Ag^+]\,[Red]\,[Ag^0{}_n] \quad (16)$$

k_2 is the rate constant for surface reduction and $Ag^0{}_n$ is the concentration of surface atoms on the nanocrystals. Notice that equation (13) and (15) are pseudo-elementary step,[45] each of which might include more steps in the actual reaction. For example, the reaction between Ag^+ and AA involves at least the following two steps:[47]

$AH_2 \leftrightarrow AH^- + H^+$ (fast)

$AH^- + Ag^+ \rightarrow AH\cdot + Ag^0$ (slow)

The second step is rate limiting. As a result, in the rate expression (14) and (16), the reaction order is one for both Ag^+ and AA. Using pseudo-elementary step to analyze complex kinetic mechanism has previously being demonstrated.[47] The total rate for Ag^+ reduction should include the contribution from both pathways:

$$-\frac{d[Ag^+]}{dt} = k_1\,[Ag^+]\,[Red] + k_2\,[Ag^+]\,[Red]\,[Ag^0{}_n] \quad (17)$$

As shown in the previous section, DNA binds to Ag^+ in a sequence-specific manner, thus certainly affecting the reduction kinetics by changing $[Ag^+]$ in the rate expression.

$$[Ag^+]_{eq} = \frac{[Ag^+]_{total}}{1+K_{eq}\,[Base]^2_{eq}} \quad (18)$$

Herein, the rate expression for DNA-controlled Ag^+ reduction reaction could be modified into the following equation:

$$-\frac{d[Ag^+]}{dt} = k_1'\,[Ag^+]_{total}\,[Red] + k_2'[Ag^+]_{total}\,[Red]\,[Ag^0{}_n] \quad (19)$$

$$k_1' = \frac{k_1}{1+K_{eq}\,[base]^2_{eq}},\ k_2' = \frac{k_2}{1+K_{eq}\,[base]^2_{eq}}$$

Table 2.1. Kinetic parameters for Ag^+ reduction with different DNA sequences in the absence of seed crystals. * Contribution of two-reduction pathways and absolute rate were calculated for the initial stage when first 5% of ascorbic acid (Red) was consumed.

DNA sequence	Solution reduction				Surface reduction			
	k_1' ($\times 10^{-5}$)	k_1 ($\times 10^{-6}$)	Percentage	Absolute rate ($\times 10^{-3}$)	k_2' ($\times 10^{-8}$)	k_2 ($\times 10^{-8}$)	Percentage	Absolute rate ($\times 10^{-3}$)
T20	0.0402 ± 0.0020 $s^{-1}\mu M^{-1}$	$0.444 \pm 0.002 s^{-1}\mu M^{-1}$	59.0%	7.26 ± 0.35 $s^{-1}\mu M$	6.96 ± 0.28 $s^{-1}\mu M^{-2}$	7.79 ± 0.31 $s^{-1}\mu M^{-2}$	41.0%	12.6 ± 0.05 $s^{-1}\mu M$
A20	1.53 ± 0.11 s^{-1}	2.24 ± 0.16 $s^{-1}\mu M^{-1}$	100.0%	1.45 ± 0.10 $s^{-1}\mu M$	-	-	0%	-
C20	$1.37 \pm 0.02 s^{-1}$	24.0 ± 3.50 $s^{-1}\mu M^{-1}$	100.0%	1.30 ± 0.02 $s^{-1}\mu M$	-	-	0%	-

To follow the DNA-mediated Ag^+ reduction kinetics, we used a UV-vis spectroscopy-based method[44, 46] to monitor the concentration of the reductant remaining in the solution at different time points.

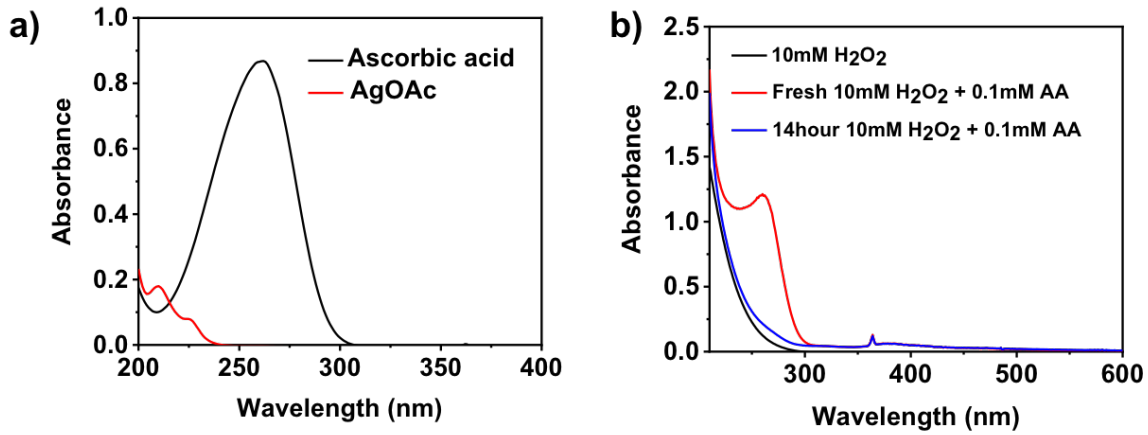


Figure 2.6: UV-vis absorbance of a) ascorbic acid (100 μM) and AgOAc (200 μM) and b) ascorbic acid oxidized by H_2O_2.

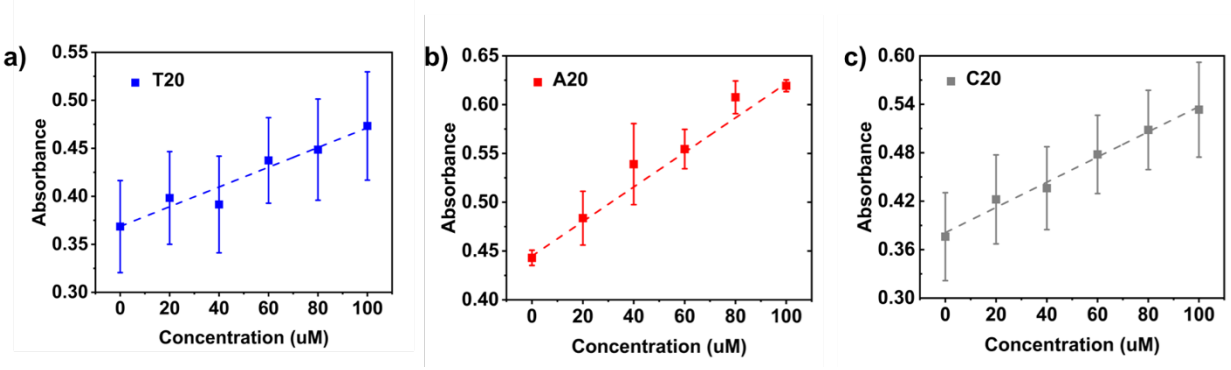


Figure 2.7: Calibration curve of UV-vis absorbance at 266 nm as a function of concentration of ascorbic acid.

As shown in Fig. 2.6a, ascorbic acid has signature peak at 266 nm, and this peak does not overlap with that of AgOAc. From Fig. 2.6b, the oxidized product of ascorbic acid does not have absorbance at 266 nm. Therefore, the absorbance change in 266 nm in the reaction solution could only be induced by the change in the concentration of ascorbic acid. Another possible complexation is that most of the DNA has absorbance at 266 nm. Because DNA is not being consumed during the reduction process, we consider the absorbance contribution from DNA is a constant throughout the reduction process, which was subtracted to retrieve the absorbance from ascorbic acid alone. Considering the complexation between DNA and Ag^+ might induce some changes to the absorbance of the DNA, for each point in the calibration curve (Fig. 2.7), we added the stoichiometry ratio (1:2) of ascorbic acid and Ag^+ together with 20 μM DNA to simulate the actual complexation condition in the reaction solution, so the minor change in DNA peak induced by Ag^+ could be mitigated. The absorbance of reaction solution without preformed seed was directly measured in a cuvette that is 1 mm in path length. Aliquot was taken from reaction solution with preformed seed at certain time points, and centrifuged at 8k rpm, 2min to remove nanocrystals. The absorbance of resulting supernatant was measured. Absorbance was converted to the concentration of ascorbic acid using the calibration curve

Ascorbic acid can react with both Ag^+ and oxygen in air. We thus analyzed and decoupled the reaction between ascorbic acid and oxygen to accurately determine the reaction kinetic between Ag^+ and ascorbic acid. The change of concentration of ascorbic acid in air without Ag^+ precursor was measured as the control experiment. The concentration of ascorbic acid solution (100 μM) was monitored in the same container used for the synthesis by the UV-vis spectroscopic method. As shown in Fig. 2.8, the concentration of ascorbic acid was only decreased by 7% after 25 h. Therefore, for reactions much shorter than 25 h, the ascorbic acid consumption by oxygen is negligible. The only reaction that has similar timescale as that of ascorbic acid decay is C20-mediated reduction with seed (See next section). However, even in this case, the contribution of oxygen oxidation of ascorbic acid is less than 10% (9.27%) of the total consumption of ascorbic acid by the reduction reaction.

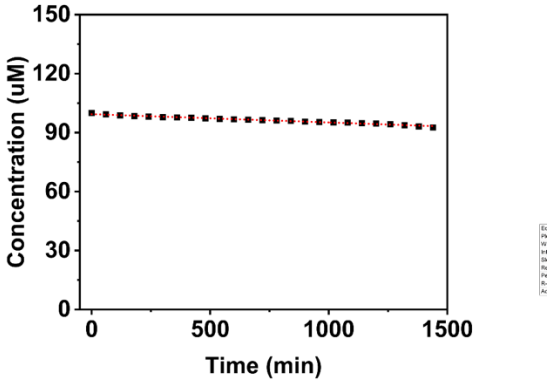


Figure 2.8: Concentration of ascorbic acid solution in air as a function of time. The initial concentration was 100 μM.

Regardless, in the following analysis, [red] has been calibrated prior to curve fitting by subtracting the ascorbic acid consumed by air for an accurate estimation of reaction rate between Ag^+ and ascorbic acid.

We conducted two parallel experiments in both absence and presence of pre-formed seed nanocrystals. While we focus on seed-mediated synthesis in this work, reduction kinetics without the pre-formed seeds provide important information on the solution reduction pathway, because without the preexisting surface of the seeds, solution reduction is dominant.[44-45] Furthermore, the sequence-specific reduction pathways in response to the absence and presence of seed also shed light on the interaction between DNA ligands and the surface of the crystals.

2.2.4 Kinetic analyses of the DNA-mediated Ag^+ reduction pathways in the absence of pre-synthesized seed

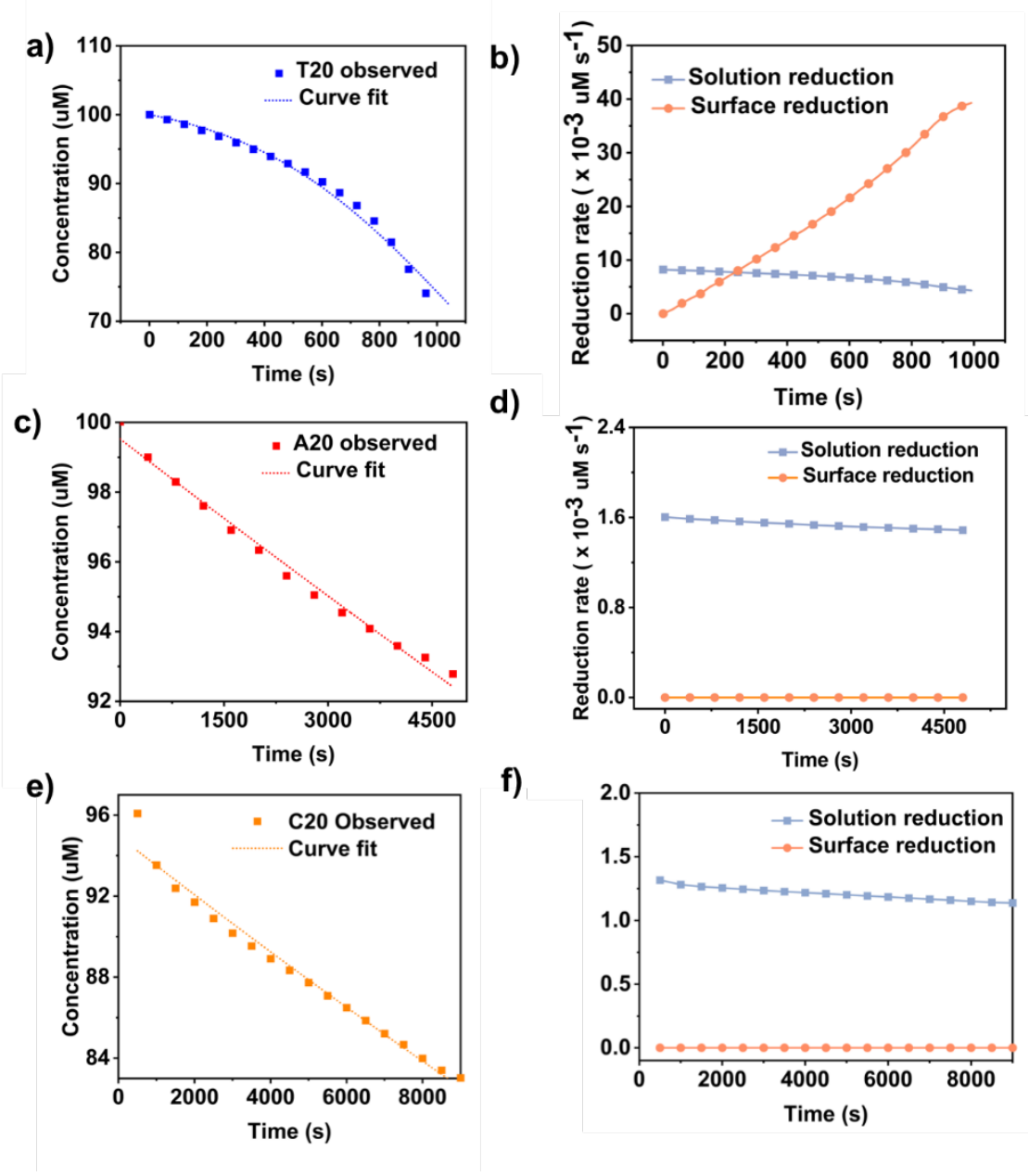


Figure 2.9: Quantitative analysis of the reduction of Ag precursor by ascorbic acid without seeds in the presence of a, b) T20, c, d) A20, and e, f) C20. a, c, e) The concentration of ascorbic acid in the reaction solution and b, d, f,) rates of solution reduction and surface reduction as a function of time in the presence of the three DNA sequences.

Fig. 2.9a, 2.9c, and 2.9e show the remaining concentration of the reductant during the Ag^+ reduction process without seeds. The reduction reaction in the presence of T20 (Fig. 2.9a) proceeded much faster than that with A20 (Fig. 2.9c) and C20 (Fig. 2.9e). Moreover, only the curve with T20 exhibited a self-catalyzed behavior.[45] We derived the kinetic model for T20 mediated reaction as follows.

$$-\frac{d[RED]}{dt} = k_1[Ag^+]_{eq}[Red] + k_2[Ag^+]_{eq}[Red][Ag^0{}_n] \quad (20)$$

$[Ag^+]_{eq} = \frac{[Ag^+]_t}{1+K_{eq}\,[base]_{eq}^2}$ ($[Ag^+]_t$ is the total $[Ag^+]$ in the solution at time t after the reaction started)

$[Ag^0{}_n] = [Ag^+]_0 - [Ag^+]_t$ ($[Ag^+]_0$ is the total $[Ag^+]$ at the beginning of the reaction[44])

According to the stoichiometry of the reaction:

$d[Ag^+]_t = 2d[Red]_t$

Initial concentration $[Ag^+]_0 = 2[Red]_0$

Substituting $[Ag^0{}_n] = [Ag^+]_0 - [Ag^+]_t$

$[Ag^+]_t = 2[Red]_t$ (the subscript t was omitted in the following equations for simplicity)

$$-\frac{d[Red]}{dt} = k_1 \frac{2[Red]}{1+K_{eq}\,[DNA]_{eq}^2}[Red] + k_2 \frac{2[Red]}{1+K_{eq}\,[DNA]_{eq}^2}[Red]\times 2([Red]_0\text{-}[Red])$$

Let $k_1' = \frac{k_1}{1+K_{eq}\,[base]_{eq}^2}$, $k_2' = \frac{k_2}{1+K_{eq}\,[base]_{eq}^2}$, $[base]_{eq} = 366.10\ \mu M$ (see following for calculation method)

$$-\frac{d[RED]}{dt} = 2k_1'[Red]^2 + 4k_2'[Red]^2\ ([Red]_0\text{-}[Red])$$

$$\int_{[Red]_O}^{[Red]} \frac{d[Red]}{(2k_1' + 4[Red]_O\,k_2'[Red]^2 - 4k_2'[Red]^3} = \int_0^t dt$$

$$t = \frac{2[\mathrm{Red}]_0[\mathrm{Red}]\times k_2' \ln\left(\frac{\left(2[\mathrm{Red}]_0 k_2'([\mathrm{Red}]_0-[\mathrm{Red}])+[\mathrm{Red}]_0 k_1'\right)}{k_1'[\mathrm{Red}]}\right)+2k_2'[\mathrm{Red}]_0^2+k_1'[\mathrm{Red}]_0-\left(2k_2'[\mathrm{Red}]_0+k_1'\right)[\mathrm{Red}]}{2[\mathrm{Red}]_0(2[\mathrm{Red}]_0 k_2'+k_1')^2[\mathrm{Red}]}$$

(21)

Based on the above analyses, the model for the T20-mediated Ag^+ reduction without preformed seeds could be described using a two-step model:

$$Ag^+ + \mathrm{Red} \xrightarrow{k_1} Ag^0 + \mathrm{Ox} \quad (22)$$

$$nAg^0 \rightarrow Ag_n^0 \quad (23)$$

$$Ag^0_n + Ag^+ + \mathrm{Red} \xrightarrow{k_2} Ag^0_{n+1} + \mathrm{Ox} \quad (24)$$

$$-\frac{d[\mathrm{Red}]}{dt} = 2k_1'[\mathrm{Red}]^2 + 4k_2'[\mathrm{Red}]^2\ ([\mathrm{Red}]_0\text{-}[\mathrm{Red}]) \quad (25)$$

$$k_1' = \frac{k_1}{1+K_{eq}\,[\mathrm{base}]_{eq}^2}\ ,\ k_2' = \frac{k_2}{1+K_{eq}\,[\mathrm{base}]_{eq}^2}$$

Equation (22) describes the solution reduction and equation (24) describes the autocatalytic surface reduction[44-46] on the formed nuclei (Ag^0_n represents the surface atoms on the just-formed nuclei). the homogeneous nucleation step (14) was excluded when considering the reduction rate of Ag^0 because the process is much faster compared with the rate for Ag^+ reduction.[48]

This model was used to analyze the growth curve with T20 (Fig. 2.9a). Rate constants k_1' and k_2' were derived from the fitting to be 4.02×10^{-7} $s^{-1}\mu M^{-1}$ and 6.96×10^{-8} $s^{-1}\mu M^{-2}$, respectively. Based on these kinetic parameters, we came up the rates for solution reduction and surface reduction as a function of time. As shown in Fig. 2.9b, the rate for surface reduction was slower than that of solution reduction in the first 200 s, which could be ascribed to the limited surface sites on the newly generated nucleus (Ag^0_n). As the reaction progressed, the rate for surface reduction increased until it surpassed the rate for solution reduction.

The kinetic model needs to be further developed to be applied to A20- and C20-mediated Ag^+ reduction reactions, because these two DNA strands bind stronger to Ag^+ than T20. Using the K_{eq} derived from the OCP measurements, we calculated the concentrations of unbound $[Ag^+]$ at given times during the reduction process using the following method.

Calculation of K_{eq}, $[Ag^+]_{eq}$ and $[base]_{eq}$

$$Ag^+ + 2Base \rightleftarrows Ag(Base)_2^+$$

1. Determine K_{eq}

$[Ag^+]_{eq}$ is determined from OCP measurements, $[Ag]_0$ and $[base]_0$ is the total concentration of Ag^+ and the base added into the solution. K_{eq} can be calculated using the following equation

$$K_{eq} = \frac{[Ag(Base)_2^+]}{[Ag^+] \times [Base]^2}$$

Because $[base]_0$ is 20 times that of $[Ag]_0$, assume the concentration of the base does not change significantly upon binding

$$[base]_0 = [base]_{eq} \quad (26)$$

$$[Ag]_0 = [Ag^+]_{eq} + [Ag(base)_2^+]_{eq} \quad (27)$$

$$K_{eq} = \frac{[Ag]_0 - [Ag^+]_{eq}}{[Ag^+]_{eq} \times [base]_0^2} \quad (28)$$

2. Determine $[Ag^+]_{eq}$ and $[base]_{eq}$ during the reduction process with known K_{eq}

During the reduction process, the concentration of bases is no longer in great excess compared with that of Ag^+ ($[base]_0$: $[Ag]_0$=2:1). Herein, an additional mass balance is considered,

$$[Ag]_0 = [Ag^+]_{eq} + [Ag(base)_2^+]_{eq}$$

$$[base]_0 = [base]_{eq} + 2[Ag(base)_2^+]_{eq} \quad (29)$$

$$K_{eq}=\frac{[\mathrm{Ag(base)_2^+}]_{\mathrm{eq}}}{[\mathrm{Ag^+}]_{\mathrm{eq}}\times[\mathrm{base}]_{\mathrm{eq}}}$$

Based on the above equations, the values for $[\mathrm{Ag^+}]_{\mathrm{eq}}$ and $[\mathrm{base}]_{\mathrm{eq}}$ are difficult to be solved mathematically, but can be solved by an exhaustive algorithm. To repeat the same calculation for a series value of $[\mathrm{Ag}]_{eq}$ and $[\mathrm{base}]_{\mathrm{eq}}$, we used a Macro in Excel that can perform goal seek in multiple cells. The calculations were performed for Ag^+ kinetic data for all DNA sequences both in the absence and presence of seeds. The average values of $[\mathrm{Ag}]_{eq}$ and $[\mathrm{base}]_{\mathrm{eq}}$ for the time scale in corresponding kinetic curves in Fig. 2.9 and Fig. 2.11 are listed in Table 2.2. Percent error is calculated by dividing the standard deviation by $[\mathrm{Ag}]_0$ or $[\mathrm{base}]_0$.

Table 2.2: Average values of $[\mathrm{Ag}]_{eq}$ and $[\mathrm{base}]_{\mathrm{eq}}$ in the Ag^+ reduction processes with different DNA sequences.

	C20		A20		T20	
	No seed	With seed	No seed	With seed	No seed	With seed
$[\mathrm{Ag^+}]_{\mathrm{eq}}$	0.57 μM $\pm$ 0.46%	1.02 μM $\pm$ 0.83%	6.83 μM $\pm$ 1.65%	0.48 μM $\pm$ 0.75%	164.00 μM $\pm$ 7.26%	26.14 μM $\pm$ 12.11%
$[\mathrm{base}]_{\mathrm{eq}}$	38.20 μM $\pm$ 2.46%	108.21 μM $\pm$ 26.56%	13.10 μM $\pm$ 0.78%	122.65 μM $\pm$ 19.12%	366.10 μM $\pm$ 0.64%	394.26 μM $\pm$ 2.52%

The standard deviations for $[\mathrm{Ag^+}]_{\mathrm{eq}}$ with C20 and A20 are relatively small compared with that of T20, which agrees with the stronger binding of C20 and A20 towards Ag^+. If we consider DNA - Ag^+ complex as a buffer system, the variation of Ag^+ during the reduction process will be affected by Ag^+ / DNA-Ag^+ equilibrium. A20 and C20 demonstrated superior buffering capability compared with that of T20. Herein, in all the kinetic models with A20 and C20,

$[Ag^+]_{eq}$ is assumed to be a constant throughout the reduction process. In contrast, $[Ag^+]_{eq}$varies significantly in the presence of T20 due to the weak buffering effect. Therefore, $[Ag^+]_{eq} = \frac{[Ag^+]_{total}}{1+K_{eq}\,[Base]_{eq}^2}$ (30) is used to account for the change of the Ag^+ in the reduction process with T20. $[base]_{eq}$ is assumed to be a constant in equation (30) because the standard deviation of $[base]_{eq}$ is much smaller than that of $[Ag^+]_{eq}$ as shown in Table 2.2**.**

The average concentrations of unbound $[Ag^+]$ were 0.57 μM $\pm$ 0.46% with C20 and 6.83 μM $\pm$ 1.65% with A20 within the timescale of the investigation. These values were two to three orders of magnitude lower than that with T20 (164.00 μM $\pm$ 7.26%), which was consistent with the observations that A20 and C20 bound strongly with Ag^+. The DNA molecules whose sequences bound more strongly to Ag^+ shifted the equilibrium towards the DNA-Ag^+ complex, resulting in a low supersaturation of the metal ion precursor throughout the reduction process. Consequently, the solution reduction became the rate-limiting step because the surface reduction relied on Ag_n^0 generated from solution reduction. The whole process thus can be approximated as a first order reaction where only the solution reduction of Ag^+ is considered:[12]

$$2Ag^+ + Red \xrightarrow{k_1} 2Ag^0 + Ox \quad (31)$$

$$nAg^0 \rightarrow Ag_n^0 \quad (32)$$

$$-\frac{d[AA]}{dt} = k_1'\,[Red] \qquad (k_1' = k_1[Ag^+]_{eq}) \quad (33)$$

To test this hypothesis, we fitted the kinetic curve in the presence of A20 and C20 with both one- and two-step models. The models were developed as follows.

A20 and C20-mediated Ag^+ reduction without preformed seed

One step analysis

$$-\frac{d[Red]}{dt} = k_1[Ag^+]_{eq}[Red] = k_1'[Red] \quad (34)$$

Let $k_1' = k_1[Ag^+]_{eq}$, $k_2' = k_2[Ag^+]_{eq}$

$[Ag^+]_{eq}$ for A20 is 6.83 μM, for C20 is 0.57 μM (Table 2.2)

$$-\frac{d[Red]}{dt} = k_1'[Red]$$

$$\int_{[Red]_O}^{[Red]} -\frac{d[Red]}{k_1'[Red]} = \int_0^t dt$$

$$ln\frac{[Red]_0}{[Red]} = k_1't$$

Rearrange the equation

$$[Red] = [Red]_0 exp^{-k_1't} \quad (35)$$

Two step analysis:

$$-\frac{d[Red]}{dt} = k_1[Ag^+]_{eq}[Red] + k_2[Ag^+]_{eq}[Red][Ag^0{}_n] \quad (36)$$

Let $k_1' = k_1[Ag^+]_{eq}$, $k_2' = k_2[Ag^+]_{eq}$

$[Ag^+]_{eq}$ for A20 is 6.83 μM, for C20 is 0.57 μM (Table 2.2)

$$-\frac{d[Red]}{dt} = k_1'[Red] + k_2'[Red]\,2([Red]_0-[Red])$$

$$\int_{[Red]_0}^{[Red]} -\frac{d[Red]}{[Red](k_1' + 2k_2'([Red]_0 - [Red]))} = \int_0^t dt$$

$$t = \frac{\ln((2k_2'([Red]_0-[Red])+k_1')[Red]_0)-\ln(k_1'[Red])}{2k_2'[Red]_0+k_1'} \quad (37)$$

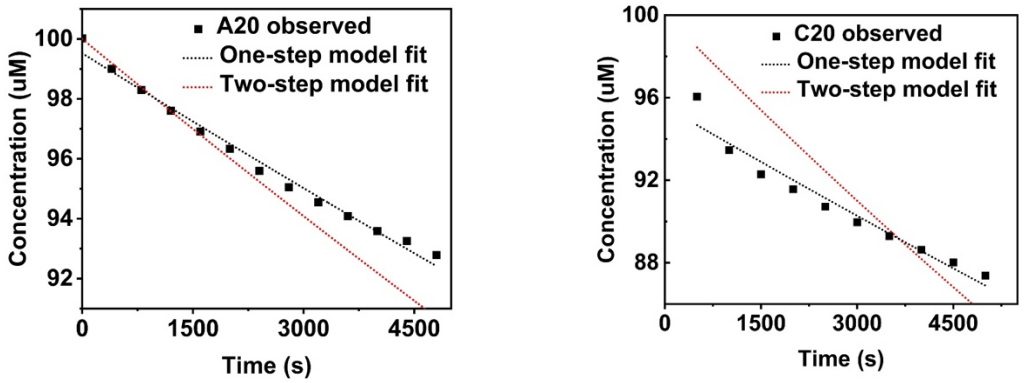


Figure 2.10. One-step and Two-step model fitting for reduction of Ag precursor by ascorbic acid in the presence of A20 and C20 without preformed seeds.

As shown in Fig. 2.10, the two-step model significantly deviated from the experimental data (R^2 value is 0.79 for A20 and 0.26 for C20), whereas the one-step model matched well with the kinetic results with the R^2 value of 0.99 for A20 and 0.95 for C20. The rate constants k_1' derived from the one-step model were 1.53×10^{-5} $s^{-1}\mu M^{-1}$ for A20 and 1.37×10^{-5} $s^{-1}\mu M^{-1}$ for C20. Compared with the two-step model, the one step-model for A20- and C20-mediated reduction kinetics did not involve the surface reduction. We calculated further the reduction rates in the presence of A20 and C20 using the kinetic parameters derived from the fitting, (Fig. 2.9d and 2.9f). Our results showed that the solution reduction dominated the A20- (Fig. 2.9d) and C20- (Fig. 2.9f) mediated Ag^+ reductions. In contrast, in the presence of T20, surface reduction became the dominate reduction pathway over time (Fig. 2.9b). The reduction rate with T20 was also much larger than those with A20 and C20. Table 1 lists all the kinetic parameters derived from the fitting.

There was a clear correlation between DNA-Ag^+ interactions and reduction pathways of Ag^+ based on the above quantitative analyses, particularly in two aspects. Macroscopically, solution and surface reductions were two consecutive steps when Ag^+ was reduced without

seeds. The product of the solution reduction (Ag^0_n) became the reactant for the surface reduction. The strong binding of Ag^+ with A20 and C20 limited the concentration of free Ag^+ thus the product (Ag^0_n) generated from the solution reduction. In the corresponding rate expression, the solution reduction became the rate-limiting step that dominated the reduction process. From a molecular perspective, the surface reduction required at least termolecular collision (equation 15), which was unlikely to happen unless the concentrations of the reactants were extremely high.[49] Such conditions could however be achieved by tuning the reaction parameters, as have been demonstrated previously in cases where the reductant was in large excess compared with the precursor.[44-45] In the case of T20 in this work, free Ag^+ concentration did not significantly decrease because of the weak DNA binding. In the two-step growth of T20-mediated kinetics, concentrations of both Ag^+ and reductant were high enough for the termolecular collision to take place in the microenvironment near the surface of nuclei. However, in the presence of A20 and C20, the possibility for termolecular collision was low because of the limited amount of Ag^+. As a result, the solution reduction dominated the A20- and C20-mediated reductions because this reaction only required bimolecular collision (equation 17). In other words, even though the rate for autocatalytic surface reduction was much faster than that of solution reduction,[44-46] the surface reduction did not contribute significantly to the overall reduction rate in the presence of A20 and C20 because it was a rare event.

2.2.5 Kinetic analyses of the DNA-mediated Ag+ reduction pathways in the presence of pre-synthesized seed.

Having analyzed the kinetics in the absence of pre-synthesized seed, we extended the kinetic study to the reduction of Ag^+ in the presence of seeds. Similar to the curve fitting in the

absence of seeds, the kinetic curve of Ag^+ reduction in the presence of T20 and the Au decahedra fitted to the two-step model (Fig. 2.11a).

To use the model developed, we made one modification to replace the concentration of surface atoms of nuclei (Ag^0_n in equation 8) with the concentration of surface atoms of the preformed seeds (Ag_n^0 (seed) in the following equations:

$$Ag^+ + Red \xrightarrow{k_1} Ag^0 + Ox \quad (38)$$

$$Ag^0 + Ag_n^0\,(seed) \rightarrow Ag_{n+1}^0\,(seed) \quad (fast) \quad (39)$$

$$Ag^0_n\,(seed) + Ag^+ + Red \xrightarrow{k_2} Ag^0_{n+1}\,(seed) + Ox \quad (40)$$

$$-\frac{d[AA]}{dt} = 2k_1'[Red]^2 + 2k_2'[Red]^2\,[Ag^0_n(seed)] \quad (41)$$

Based on this analysis, the rate constant for surface reduction k_2' was determined to be $8.96 \times 10^{-6}\ s^{-1}\mu M^{-2}$ assuming the observed rate constant for solution reduction (k_1') was the same as that in the reduction kinetic without seeds.[44] The models were derived as follows.

T20-mediated Ag^+ reduction with preformed seed: two step analysis

$$-\frac{d[AA(re)]}{dt} = k_1[Ag^+]_{eq}[Red] + k_2[Ag^+]_{eq}[Red][Ag^0_n(seed)] \quad (42)$$

where $[Ag^0_n(seed)]$ is the total concentration of the surface atoms on the seed. It was assumed $[Ag^0_n(seed)]$ does not change over time, because the overall size of the final particle was similar to that of the seed.[1] $[Ag^0_n(seed)]$ was calculated to be 4.5 μM using the method described previously.[44] The concentration of available surface sites for Ag atom deposition is less than the total concentration of surface atoms due to the surface passivation by DNA. The ligand replacement assay in the remaining active surface sites was determined by the following equations:

$[Ag^0_n(seed)]_{T20} = 4.5\ \mu M \times 98.71\% = 4.4\ \mu M$

$$[Ag^+]_{eq} = \frac{[Ag^+]_t}{1+K_{eq}\,[DNA]_{eq}^2}$$

According to the stoichiometry of the reaction, we can obtain the following relationship: $d[Ag^+]_t = 2d[Red]_t$

where the initial Ag^+ concentration $[Ag^+]_0$ is equal to $2[Red]_0$, and $[Ag^+]_t$ is equal to $2[Red]_t$. For simplicity, the subscript t was omitted in the following equations:

$$-\frac{d[Red]}{dt} = k_1 \frac{2[Red]}{1+K_{eq}\,[base]_{eq}^2}[Red] + k_2 \frac{2[Red]}{1+K_{eq}\,[base]_{eq}^2}[Red]\,[Ag^0{}_n(seed)]$$

Let $k_1' = \frac{k_1}{1+K_{eq}\,[base]_{eq}^2}$, $k_2' = \frac{k_2}{1+K_{eq}\,[base]_{eq}^2}$, $[base]_{eq} = 394.26\ \mu M$ (Table 2.2)

$$[Red] = \frac{1}{2\left(k_1' + k_2'[Ag_n^0(seed)]\right)t + 1/[Red]_0} \quad (43)$$

The reduction rate with T20 was then calculated using the obtained rate constant (Fig. 2.11b). The rate for surface reduction was the highest at the early stage of the reaction, because of the abundant seeds in the solution, and quickly dropped due to the depletion of the reagents. Overall, surface reduction had a much higher rate than solution reduction in T20-mediated Ag^+ reduction with the seeds.

In the presence of A20 and C20, the seed-mediated growth was no longer a simple one-step as in the case without seeds. In the one-step growth, the solution reduction was the rate limiting step because the concentration of precursor, reductant and reactive surface sites were limited. However, when seeds were introduced, the concentration of surface sites available for the reductive adsorption of Ag^+ was greatly increased. Moreover, the solution and surface reductions occurred simultaneously with seeds, instead of consecutively as without the seeds. The solution reaction and surface reaction were no longer interdependent because the surface reduction also took place on the seeds rather than just the nuclei. Therefore, in the presence of the seeds, the A20- and C20-mediated reaction should be analyzed using the two-step models.

We used the two-step model to fit the kinetic curve with A20. The two step model was derived as follows.

A20 and C20-mediated Ag^+ reduction with preformed seed: two-step process

For a two-step process, the reaction can be determined by the following equations:

$$-\frac{d[AA(re)]}{dt} = k_1[\mathrm{Ag^+}]_{eq}[\mathrm{Red}] + k_2[\mathrm{Ag^+}]_{eq}[\mathrm{Red}][\mathrm{Ag^0_n(seed)}] \quad (44)$$

$$[\mathrm{Red}] = [\mathrm{Red}] = [Red]_0 exp^{-(k_1' + k_2'[Ag_n^0(seed)])t} \quad (45)$$

where $k_1' = k_1[\mathrm{Ag^+}]_{eq}$ and $k_2' = k_2[\mathrm{Ag^+}]_{eq}$. $[\mathrm{Ag^+}]_{eq}$ is 0.48 μM for A20 and 1.02 μM for C20 (Table 2.2). $[\mathrm{Ag^0_n(seed)}]_{A20}$ is equal to 4.5 μM × 95.63% or 4.3 μM, and $[\mathrm{Ag^0_n(seed)}]_{C20}$ is equal to 4.5 μM × 93.77% or 4.2 μM.

In this two-step analysis, the surface reduction reaction on the nuclei was not included in the calculations because in the reduction without the seed, the surface reduction on the just-formed nuclei does not contribute to the overall reduction rate. The growth curves in the presence of A20 and C20 were fitted with both one- and two-step models. The two-step model significantly deviated from the experimental data (R^2 value is 0.79 for A20 and 0.26 for C20), whereas the one-step model matched well with the kinetic results with the R^2 value of 0.99 for A20 and 0.95 for C20. The k_1' value derived from the one-step model was 1.53×10^{-5} $s^{-1}\mu M^{-1}$ for A20 and 1.37×10^{-5} $s^{-1}\mu M^{-1}$ for C20. Unlike the two-step model, the one step-model did not involve the surface reduction for either A20- or C20-mediated reduction. The result from the model fitting suggested that even though there existed self-nucleation in the seed-mediated synthesis, those nuclei did not lead to additional surface reduction reaction. The inhibition of surface reduction on the nuclei could originate from passivating the surface of the nuclei by DNA. The formed nuclei are much smaller in size (3.0 ± 1.0 nm) than the nanocrystals formed with the seed (74.8 ± 3.4 nm), thus have larger surface-to-volume ratio and higher surface energy. The active surface sites on the

nuclei therefore might be passivated to a larger extent than the seeded crystals due to their interaction with DNA. Formation of smaller nanoparticles with poly-A DNA sequences was also previously observed in the seed-mediated synthesis of Au NPs.[24] This phenomenon appears to be common among different systems, which suggests adenosine should stabilize small nanocrystals, presumably due to its ability to bind to the high index facets.[22]

The fitted curve was in excellent agreement with the experimental data (Fig. 2.11a, R^2=0.99). The rate constant for surface reduction k_2' was determined to be 6.93×10^{-6} $s^{-1}\mu M^{-2}$. We also calculated the reduction rate for the A20-mediated reaction kinetic as a function of time. As shown in Fig. 2.11d, both solution and surface reduction pathways were present in A20-mediated reaction, with the surface reduction pathway contributed more significantly in the overall reduction rate.

Similarly, the two-step model was used to analyze the kinetics in the presence of C20. The rate constant for solution reduction k_1' derived from fitting was 1.29×10^{-5} s^{-1} (Fig. 2.11e, R^2 = 0.99), which was strikingly consistent to the k_1' in the absence of seed (5.8% difference), suggesting the absence of the surface reduction as in the one-step growth mechanism as follows.

C20-mediated Ag^+ reduction with preformed seed: one step process

$$-\frac{d[Red]}{dt} = k_1[Ag^+]_{eq}[Red] = k_1'[Red] \quad (46)$$

$[Ag^+]_{eq}$ for C20 is 1.02 μM (Table 2.2)

$$\int_{[Red]_0}^{[Red]} -\frac{d[Red]}{[Red]} = \int_0^t dt$$

$$\ln\frac{[Red]_0}{[Red]} = k_1't$$

Rearrange

$$[Red] = [Red]_0 exp^{-k_1't} \quad (47)$$

Therefore, one-step model was a better fit for C20. Unlike A20, introducing seeds did not alter the reduction pathway in the C20-coupled growth. We also calculated the reduction rate using the kinetic parameter derived from the one-step model (Fig. 2.11f). A summary of all the kinetic parameters obtained from the above analyses is listed in Table 2.3.

Table 2.3: Kinetic parameters for Ag+ reduction with different DNA sequences in the presence of pre-formed seed. *Contribution of two reduction pathways and absolute rate were calculated when first 5% of ascorbic acid (Red) was consumed.

DNA sequence	Solution reduction				Surface reduction			
	k_1' ($\times 10^{-5}$)	k_1 ($\times 10^{-6}$)	Contribution	Absolute rate ($\times 10^{-3}$)	k_2' ($\times 10^{-6}$)	k_2 ($\times 10^{-5}$)	Contribution	Absolute rate($\times 10^{-3}$)
T20	0.0402 ± 0.0020 $s^{-1}\mu M^{-1}$	0.444 ± 0.022 $s^{-1}\mu M^{-1}$	0.01%	7.26 ± 0.36 $s^{-1}\mu M$	8.96 ± 0.89 $s^{-1}\mu M^{-2}$	1.00 ± 0.01 $s^{-1}\mu M^{-2}$	99.9%	359 ± 35.5 $s^{-1}\mu M$
A20	1.53 ± 0.11 s^{-1}	2.24 ± 0.16 $s^{-1}\mu M^{-1}$	40.3 %	1.45 ± 0.10 $s^{-1}\mu M$	5.28 ± 0.18 $s^{-1}\mu M^{-1}$	0.77 ± 0.03 $s^{-1}\mu M^{-2}$	59.7%	2.16 ± 0.07 $s^{-1}\mu M$
C20	1.29 ± 0.05 s^{-1}	1.26 ± 0.05 $s^{-1}\mu M^{-1}$	100%	1.23 ± 0.15 $s^{-1}\mu M$	-	-	0%	-

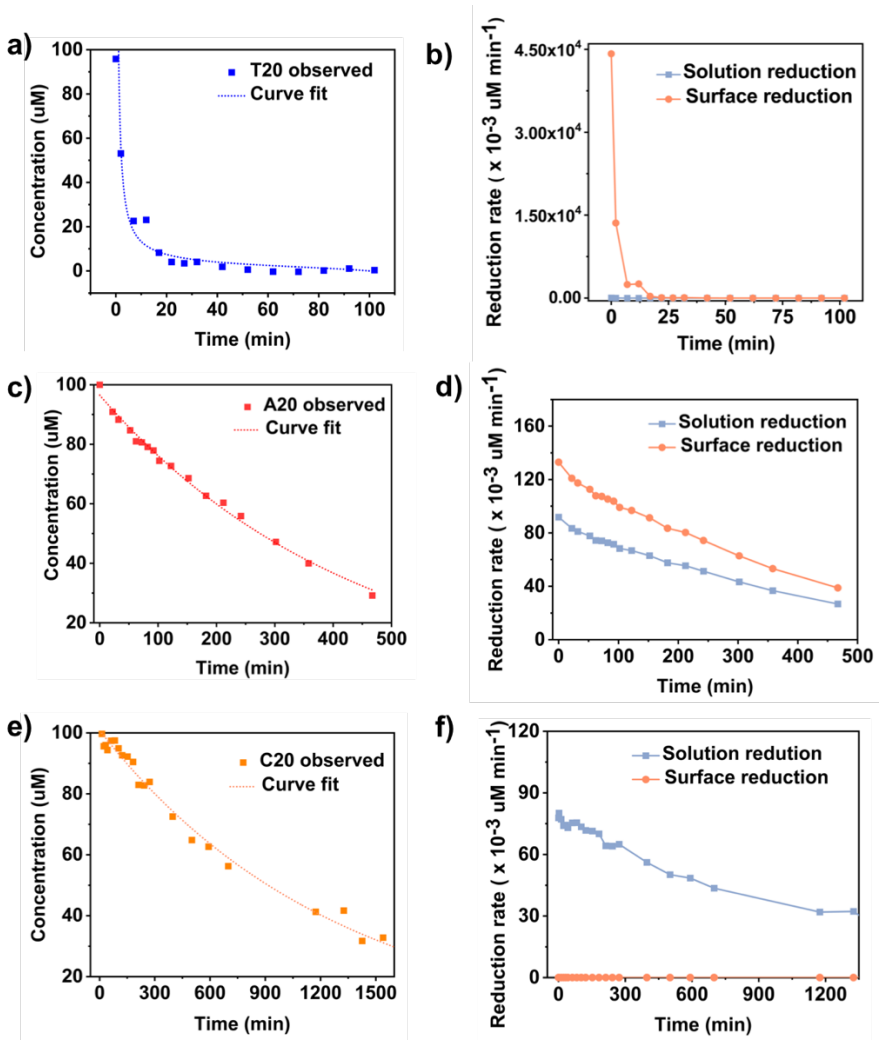


Figure 2.11: Quantitative analysis of the reduction of Ag precursor by ascorbic acid with Au decahedra seeds in the presence of a, b) T20, c, d) A20, and e, f) C20. a, c, e) The concentration of ascorbic acid in the reaction solution and b, d, f,) rates of solution reduction and surface reduction as a function of time in the presence of the three DNA sequences.

To compare the reduction pathways of DNA with all three sequences, we calculated the percentage of solution and surface reductions by integrating the reaction rates over time (Fig. 5a, Table 1 and Table 2). For C20, the solution reduction accounted for 100% of the particle formation with or without the seeds. Similarly, solution reduction dominated the seedless reduction kinetic in the case of A20. However, when the seeds were introduced, surface

reductions (59.7%) became the dominate reduction pathway. On the other hand, when using T20, both solution (59.0%) and surface reduction (41.0%) contributed to the crystal growth in the absence of seeds, whereas the surface reduction (99.9%) dominated with the seeds.

We further analyzed the absolute reduction rate for all three sequences for the initial period of the reaction, that was, until 5% of ascorbic acid was consumed (Fig. 2.12b, Table 2.1 and Table 2/3). The rate for solution reduction was comparable between A20 (1.45×10^{-3} s^{-1} μM) and C20 (1.23×10^{-3} s^{-1} μM) but 5~9 times higher for that with T20 (7.26×10^{-3} s^{-1} μM). Moreover, the rate for surface reduction when using T20 without seed reached 1.26×10^{-2} s^{-1} μM while there was no observable surface reduction for A20 and C20. More significantly, the rate for surface reduction for T20 with seed (3.59×10^{-1} s^{-1} μM) was almost two orders of magnitude higher than that of A20 (2.16×10^{-3} s^{-1} μM).

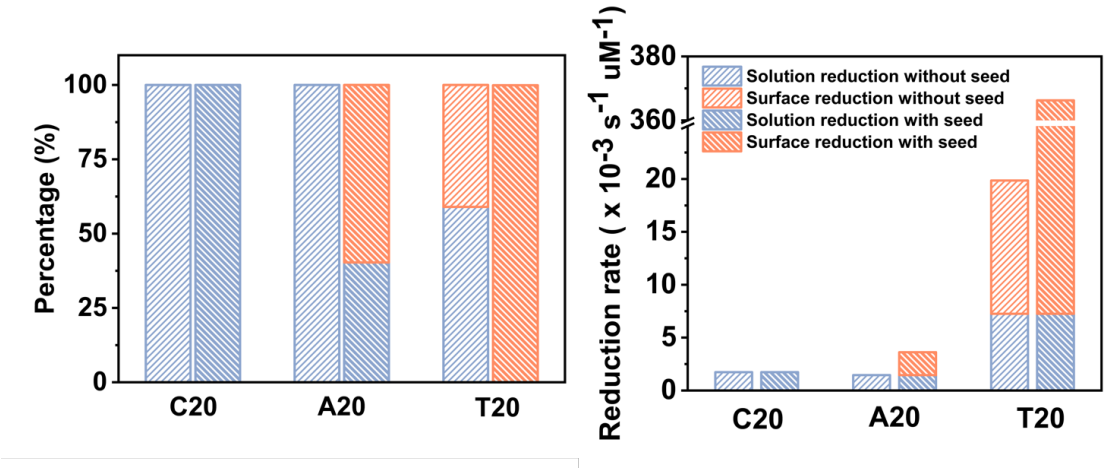


Figure 2.12: a) Percentage and b) the corresponding rates of solution and surface reductions with and without seeds when 5% of AA is reacted.

2.2.6 Interactions between DNA and the surface of nanocrystals

Unlike A20, surface reduction did not become the dominate reduction pathway when we introduced the pre-formed seeds in the C20-mediated Ag^+ reduction. What caused the difference

in the sequence-specific reduction pathways in the presence of the seed? Besides the difference in the DNA-Ag^+ binding, could DNA sequences also interact differently with the surface of the nanocrystals? We hypothesize that C20 might have passivated the surface of the nanocrystals more than A20 did, which prevented the active sites on the surface from participating in the surface reduction. To test this hypothesis, we designed a mercaptoethanol (ME) replacement assay to test the relative binding affinity of DNA to the surface of nanocrystals. Previously, Demers *et al*. developed a method to use ME to replace thiolated DNA on the surface of Au nanocrystals for DNA quantification.[50] However, unlike the DNA conjugated onto the nanocrystals through thiol-metal bonding, the DNA attached on the surface of nanocrystals during the synthesis could not be completely removed by ME replacement, even if it did not have the thiol modification.[19,23] Based on these observations, we reasoned that ME could be used as a reference for binding affinity of DNA towards the surface of nanocrystals. Upon exchange with ME, the DNA whose sequences have high affinity towards the surface of the crystals should be replaced to a lesser extent than the ones with low affinity.

Using a modified fluorescence-based DNA quantification method, we quantified the percentage of DNA strands being replaced (%Re) after the ME exchange, and obtained $93.77 \pm 1.27\%$ for C20, $95.63 \pm 0.31\%$ for A20, and $98.71 \pm 0.40\%$ for T20. The quantification method was as follows.

Fluorescence-based DNA quantification method using ME replacement

Experiments of DNA quantification were performed using fluorescein-labeled DNA to replace unlabeled DNA for the nanoparticle growth. The formed particles were washed by washed and then centrifuged to remove the excess DNA in the solution. Each batch of synthesized particles was separated into two equal portions. Half of the particles was added to 1ml of 10-mM KCN to

etch the particles and release DNA. The reaction took 6 h to complete. The concentration of DNA was determined through fluorescence measurements of the KCN solution. The concentration of DNA attached on the particles is designated as C_{total}. The other half of the particles was dispersed in 1ml of 14-mM ME for ligand exchange. The reaction was left for 12 hours for completion. The particles were thoroughly washed to remove the excess ME after the ligand exchange. The washed particles were redispersed in 1ml of 10-mM KCN for etching particles and release DNA. The reaction was left for 6 h for completion. The concentration of DNA was determined through fluorescence measurements of the etched solution. The concentration of the original DNA on the particles after ligand exchange is herein designated as C_{un}. The concentration of replaced DNA (C_{re}) was calculated by the following equation:

$$C_{re} = C_{total} - C_{un} \quad (48)$$

The percentage of replacement %Re could be calculated based on the following equation:

$$\%Re = C_{re} / C_{total} \times 100\%$$

We performed the quantitative analysis for both Ag shells and Au cores. The percentage of replacement is listed in Table S2.

Table 2.4: Percentage of DNA on both Ag shells and Ag cores replaced by ME.

%Re	C20	A20	T20
Ag shell	93.77 ± 1.27%	95.63 ± 0.31%	98.71 ± 0.40%
Au core	92.12 ± 3.26%	96.98 ± 2.05%	98.33 ± 1.30%

The percentage of DNA replacement on both Ag shells and Au cores follows the order: C20 < A20 < T20, which indicates the similar order on the available active sites on these two types of nanostructures. Ag and Au are in the same group in the periodic table, and both crystals have the

FCC structures with similar lattice constants.[34] The similarity in the trend of DNA binding can be ascribed to the similar physicochemical properties between Ag and Au. The data indicates that the diffusivity of Ag atoms on the Au core follows the same trend as that on the Ag shell, which results in similar deposition and diffusion patterns. Note that all the relative DNA binding affinity were compared with ME. We could compare the relative affinity across different sequences but we could not compare the binding affinity of the same sequence to both Ag shell and Au core, because the binding affinity of ME to the Ag shell and the Au core might be different. However, such discrepancy does not affect the conclusion drawn from the data because the deposition and diffusion of Ag atoms on the Ag crystal surfaces are the determining factors in the analysis. This method is reasonable because after the first layer was deposited onto the Au seed (either complete or partial coverage), Ag adatoms would be preferably deposited on the formed Ag layers. Therefore, the following process should be deposition of Ag on the surface of the same metal.

The concentration of available surface sites ($[Ag^0_n(seed)]_{available}$) for Ag atom deposition was less than the total concentration of surface atoms ($[Ag^0_n(seed)]$) due to DNA passivation. The percentage of DNA strands being replaced (%Re) after the ME exchange indicated the remaining active sites on the nanocrystal surfaces. Therefore, the active surface sites on the nanocrystals in the presence of DNA was described by the following equation.

$$[Ag^0_n(seed)]_{available} = [Ag^0_n(seed)] \times \%Re \quad (49)$$

The above quantitative analysis was further incorporated into the kinetic models in the previous sections. The rate constants for surface reduction in the presence of seed (k_2) could be derived as 1.03×10^{-5} $s^{-1}\mu M^{-2}$ for A20- and 1.00×10^{-5} $s^{-1}\mu M^{-2}$ for T20-mediated growth. The derived rate constants are summarized in Table 2.

We used ME as a reference for binding affinity to quantify the active sites on nanocrystals that have not been permanently blocked by the DNA binding. A variety of capping ligands have been proposed to bind to the surface of the nanocrystals.[51-53] If the binding is weak, the ligands can then dynamically adsorb and desorb from the surface, which might not prevent the adatom from incorporating into the nanocrystals. However, capping ligands that bound strongly to the surface could irreversibly passivate the reactive sites and reduce the accessibility of the surface. Mercaptoethanol forms covalent bonds with Au and Ag surfaces though its S atom.[54-55] Therefore, we used ME to estimate the extent by which the DNA irreversibly bound the surface-active sites, though we recognize there exists an uncertainty of using the affinity of ME to the surface as a reference, and the number of surface sites occupied by each DNA strand could be hard to determine. Despite of the limitations, such essay provides important insights for studying the binding of capping ligand to nanocrystal surfaces.

2.2.7 Proposed mechanism for morphology evolution

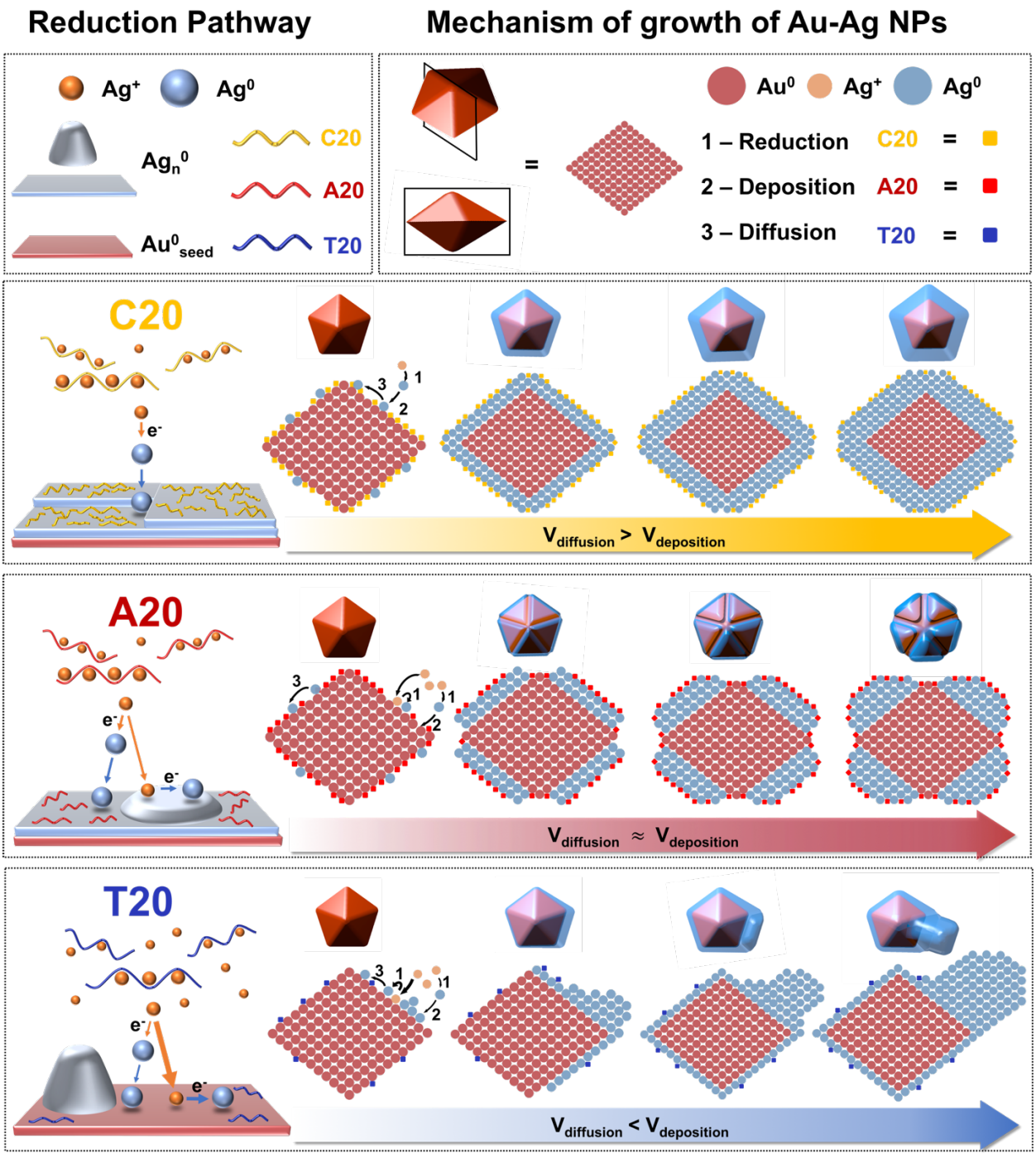


Figure 2.13: Proposed mechanism of the Ag^{+} reduction pathway and morphology evolution of Au-Ag core-shell NPs influenced by different DNA sequences.

Based on the above quantitative analysis, we analyzed the effects of the DNA molecules on the precursor complexation, reduction pathways, and surface passivation. All three factors synergistically affected atom deposition and diffusion on the growing nanocrystals, which resulted in different morphologies. Specifically, the binding between the DNA and Ag^+ precursor determined the supersaturation level of Ag^+ available for reduction; the corresponding reduction pathways of Ag^+ dictated the location and rate for Ag^0 generation and deposition; and the interactions between DNA and the surfaces of nanocrystals determined the diffusion pattern of adatoms. Based on these insights gained from quantitative analysis, we propose the following mechanisms for DNA-mediated Ag^+ reduction pathways and morphological evolution of Au-Ag NPs (Fig. 2.13).

First, the strong binding between C20 and Ag^+ limited the free Ag^+ for reduction, while slow solution reduction dominated under this C20-mediated Ag^+ reduction pathway. Both factors resulted in the slow rate of Ag^0 deposition (V_{dep}). C20 also passivated the surface the most among the three sequences, which reduced the rate for atom diffusion on the nanocrystals (V_{dif}). However, the reduced V_{dif} was still larger than V_{dep}, resulting in adatoms to migrate to low surface energy sites. The corresponding morphological evolution of the Au-Ag structure synthesized with C20 exhibited well-controlled epitaxial deposition on the decahedral core. The final structures exhibited primarily {111} facets, which are thermodynamically favorable. The growth kinetics and resulting structures indicate the growth process of C20 was likely to be thermodynamically controlled. Besides, the stabilization of {111} facets by C20 might have also contributed to the exposure of {111} facets in the final structures. Stabilization of {111} facets by C20 was also reported previously in the synthesis of Ag nanocrystals.[23]

A20 had a weaker Ag^+ binding affinity than C20. As a result, A20-mediated Ag^+ reduction went through a mixed reduction pathway with surface reduction being the dominant. The weaker Ag^+ binding affinity and surface reduction dominated pathway resulted in higher V_{dep} for A20-mediated Ag^+ reduction than that of C20. In the meantime, A20 also occupied less surface-active sites on the nanocrystal surfaces, leading to higher V_{dif} than that of C20. The morphology of nanocrystals synthesized with A20 maintained the five-fold symmetric structures that retained the thermodynamically favorable {111} facets, while exhibited grooves and ridges along the twin edges. The A20-mediated structures were likely the result of a mixed thermodynamic and kinetic controlled growth. Reentrant groves appeared during the growth of penta-twinned structures due to the lattice strain stemmed from the symmetrical axis.[56] If V_{dif} is much larger than V_{dep}, those high-energy grooves and ridges would be filled by the adatoms moving over from other regions of the surface. However, when V_{dif} is comparable with V_{dep}, the reentrant grooves are preserved. Under this mode of formation, the crystals grew along the direction parallel to the central axis to minimize the increase of lattice strain. The observation of partially preserved {111} facets suggests A20-mediated structure was the result of the mixed thermodynamically and kinetically controlled growth. Besides, A20 might also preferentially bind to the high-index facets in the grooves and ridges. Previously, it was reported A30 was used to stabilize the high-index facets of Au prisms, facilitated the disappearance of {111} facets in the final structures.

2.3 Conclusion

In summary, we have quantitatively analyzed the effects of DNA on the formation of Au-Ag nanocrystals in a sequence-specific manner. Three major factors contributed to the sequence-specific controlled growth of Au-Ag core-shell nanocrystals. First, the complexation between the

DNA and Ag^+ precursor modified the supersaturation level of the ion precursors. Second, the DNA-mediated Ag^+ reduction pathways determined the sites and rates for the generation and deposition of Ag atoms. Finally, the passivation of DNA towards the surface determined the diffusion of the adatoms on nanocrystal surface. The synergistic effect from these three factors controls the thermodynamics and kinetics of the growth process, which led to sequence-specific morphologies.

The analyses of the growth mechanism and morphology evolution of the penta-twinned decahedra-derived structures have furthered our understanding for the growth process of nanocrystals with complex structures and demonstrate the possibility to use DNA-based crystallization mechanisms to predict the final structure of the nanocrystals. The rules we have learned from this DNA ligand-based study should be applicable in identifying and understanding other biomolecular ligands for nanocrystal synthesis. Moreover, the findings from this study can also facilitate precise thermodynamic and kinetic control by rational design of metal-ligand interactions. Finally, the methods developed in this study for the interaction between DNA sequences with the precursor and the surface of nanocrystals are suited for other ligands and other types of nanomaterials, which helps moving towards the goal of predictable synthesis of nanomaterials.

2.4 Experimental section

2.4.1 Chemicals and Materials

All single stranded DNA sequences were purchased from Integrated DNA Technologies (Coralville, IA) with standard desalting and without further purification. Gold(III) chloride trihydrate (≥99.9% trace metals basis), benzyldimethylhexadecyl-ammonium chloride (BDAC, cationic surfactant), sodium borohydride (99.99% trace metals basis), silver acetate (AgOAc,

99.99% trace metals basis), L-ascorbic acid (≥99%), 2-mercaptoethanol (≥99%), cetyltrimethylammonium chloride (CTAC) and citric acid were purchased from Sigma-Aldrich. Deionized water (18.2 MΩ) was used to dissolve all chemicals.

2.4.2 Preparation of Au Decahedra NPs

Au decahedra NPs were synthesized using previously published seed-mediated procedure.[33] The seed for Au decahedra was synthesized by reducing $HAuCl_4$ (10 mL, 0.25 mM) with $NaBH_4$ (0.25 mL, 25 mM) in the presence of CTAC (50 mM) and citric acid (5 mM) under vigorous stirring at room temperature. The seed solution was then heated in an oil bath at 80 ºC for 90 min under gentle stirring. 45$\boldsymbol{\mu}$L of gold seeds was added to a growth solution containing BDAC (12.5 mL, 100 mM), $HAuCl_4$ (125 $\boldsymbol{\mu}$L, 50 mM) and ascorbic acid (93.75 $\boldsymbol{\mu}$L, 100 mM) at 30 ºC. The mixture was left undisturbed at 30 °C for 30 min.

2.4.3 DNA-Mediated Synthesis of Au-Ag Core-Shell NPs

The Au decahedra seed was washed by centrifugation (6k rpm, 5 min) for three times to remove as much BDAC as possible (SI Note 10). The washed decahedra solution was diluted with DI water until the absorbance at 557 nm reached 0.7. Concentration of Au decahedra was calculated to be 3.27×10^9 particles/mL based on the Au concentration determined by ICP-MS. 97 $\boldsymbol{\mu}$L of the diluted solution were incubated with 20 $\boldsymbol{\mu}$M single stranded DNA (C20, A20, T20) for 15 minutes. Then 1 $\boldsymbol{\mu}$L of 10 mM ascorbic acid solution and 2 $\boldsymbol{\mu}$L of 10 mM AgOAc solution were added, followed by vortex of the solution. Then the reaction is left to completion.

2.4.4 Measurement of open circuit potential of AgOAc Solution with different DNA sequences

Open circuit potential was measured on a CHI 760 potentiostat. A polycrystalline silver wire was used as the working electrode and Ag/AgCl as the reference electrode. The reference was separated from solution via an agar-0.1 M $NaClO_4$ salt bridge to prevent chloride crossover

into the working solution. Twenty microliters of 1 mM of single stranded DNA solution of a certain sequence (C20, A20, T20) was added into 1 mL of 20-μM AgOAc solution. The solution was left undisturbed for 30 minutes to reach equilibrium. Each experiment was repeated three times with different batches of DNA solution to ensure reproducibility. No supporting electrolyte was added during the titration.

2.4.5 Instrumentation and Characterization

The synthesized nanostructures were analyzed using a JEOL 2100 cryo TEM operated at 200 kV or a Hitachi S4800 SEM at 10 kV and 10 μA. UV-vis spectroscopy was performed on an HP 8453 UV-Vis spectrometer.

2.5 References

1. Stamenkovic, V. R.; Fowler, B.; Mun, B. S.; Wang, G.; Ross, P. N.; Lucas, C. A.; Markovic, N. M., Improved Oxygen Reduction Activity on Pt3Ni(111) via Increased Surface Site Availability. *Science* **2007,** *315* (5811), 493-497.

2. Leenders, S. H. A. M.; Gramage-Doria, R.; de Bruin, B.; Reek, J. N. H., Transition metal catalysis in confined spaces. *Chemical Society Reviews* **2015,** *44* (2), 433-448.

3. Bogart, L. K.; Pourroy, G.; Murphy, C. J.; Puntes, V.; Pellegrino, T.; Rosenblum, D.; Peer, D.; Lévy, R., Nanoparticles for Imaging, Sensing, and Therapeutic Intervention. *ACS Nano* **2014,** *8* (4), 3107-3122.

4. Smith, B. R.; Gambhir, S. S., Nanomaterials for In Vivo Imaging. *Chemical Reviews* **2017,** *117* (3), 901-986.

5. Giljohann, D. A.; Seferos, D. S.; Daniel, W. L.; Massich, M. D.; Patel, P. C.; Mirkin, C. A., Gold Nanoparticles for Biology and Medicine. *Angewandte Chemie International Edition* **2010,** *49* (19), 3280-3294.

6. Xia, Y.; Xiong, Y.; Lim, B.; Skrabalak, S. E., Shape-controlled synthesis of metal nanocrystals: simple chemistry meets complex physics? *Angew Chem Int Ed Engl* **2009,** *48* (1), 60-103.

7. Gu, J.; Zhang, Y.-W.; Tao, F., Shape control of bimetallic nanocatalysts through well-designed colloidal chemistry approaches. *Chemical Society Reviews* **2012,** *41* (24), 8050-8065.

8. Xia, Y.; Xia, X.; Peng, H.-C., Shape-Controlled Synthesis of Colloidal Metal Nanocrystals: Thermodynamic versus Kinetic Products. *Journal of the American Chemical Society* **2015,** *137* (25), 7947-7966.

9. Xia, Y. N.; Gilroy, K. D.; Peng, H. C.; Xia, X. H., Seed-Mediated Growth of Colloidal Metal Nanocrystals. *Angew. Chem.-Int. Edit.* **2017,** *56* (1), 60-95.

10. Zhan, G.; Zeng, H. C., Smart Nanocatalysts with Streamline Shapes. *ACS Central Science* **2017,** *3* (7), 794-799.

11. Zheng, K.; Loh, K. Y.; Wang, Y.; Chen, Q.; Fan, J.; Jung, T.; Nam, S. H.; Suh, Y. D.; Liu, X., Recent advances in upconversion nanocrystals: Expanding the kaleidoscopic toolbox for emerging applications. *Nano Today* **2019,** *29*, 100797.

12. Yin, X.; Shi, M.; Wu, J.; Pan, Y. T.; Gray, D. L.; Bertke, J. A.; Yang, H., Quantitative Analysis of Different Formation Modes of Platinum Nanocrystals Controlled by Ligand Chemistry. *Nano Lett.* **2017,** *17* (10), 6146-6150.

13. Ortiz, N.; Skrabalak, S. E., On the Dual Roles of Ligands in the Synthesis of Colloidal Metal Nanostructures. *Langmuir* **2014,** *30* (23), 6649-6659.

14. Langille, M. R.; Personick, M. L.; Zhang, J.; Mirkin, C. A., Defining Rules for the Shape Evolution of Gold Nanoparticles. *Journal of the American Chemical Society* **2012,** *134* (35), 14542-14554.

15. Murphy, C. J.; Jana, N. R., Controlling the Aspect Ratio of Inorganic Nanorods and Nanowires. *Advanced Materials* **2002,** *14* (1), 80-82.

16. Burrows, N. D.; Vartanian, A. M.; Abadeer, N. S.; Grzincic, E. M.; Jacob, L. M.; Lin, W.; Li, J.; Dennison, J. M.; Hinman, J. G.; Murphy, C. J., Anisotropic Nanoparticles and Anisotropic Surface Chemistry. *The Journal of Physical Chemistry Letters* **2016,** *7* (4), 632-641.

17. Xia, X.; Xie, S.; Liu, M.; Peng, H.-C.; Lu, N.; Wang, J.; Kim, M. J.; Xia, Y., On the role of surface diffusion in determining the shape or morphology of noble-metal nanocrystals. *Proceedings of the National Academy of Sciences* **2013,** *110* (17), 6669.

18. Wang, Y.; Reddy Satyavolu, N. S.; Lu, Y., Sequence-specific control of inorganic nanomaterials morphologies by biomolecules. *Current Opinion in Colloid & Interface Science* **2018,** *38*, 158-169.

19. Wang, Z.; Zhang, J.; Ekman, J. M.; Kenis, P. J. A.; Lu, Y., DNA-Mediated Control of Metal Nanoparticle Shape: One-Pot Synthesis and Cellular Uptake of Highly Stable and Functional Gold Nanoflowers. *Nano Lett.* **2010,** *10* (5), 1886-1891.

20. Wang, Z.; Tang, L.; Tan Li, H.; Li, J.; Lu, Y., Discovery of the DNA "Genetic Code" for Abiological Gold Nanoparticle Morphologies. *Angew. Chem. Int. Ed.* **2012,** *51* (36), 9078-9082.

21. Song, T.; Tang, L.; Tan Li, H.; Wang, X.; Satyavolu Nitya Sai, R.; Xing, H.; Wang, Z.; Li, J.; Liang, H.; Lu, Y., DNA‐Encoded Tuning of Geometric and Plasmonic Properties of Nanoparticles Growing from Gold Nanorod Seeds. *Angew. Chem. Int. Ed.* **2015,** *54* (28), 8114-8118.

22. Tan, L. H.; Yue, Y.; Satyavolu, N. S. R.; Ali, A. S.; Wang, Z.; Wu, Y.; Lu, Y., Mechanistic Insight into DNA-Guided Control of Nanoparticle Morphologies. *JACS* **2015,** *137* (45), 14456-14464.

23. Wu, J.; Tan, L. H.; Hwang, K.; Xing, H.; Wu, P.; Li, W.; Lu, Y., DNA Sequence-Dependent Morphological Evolution of Silver Nanoparticles and Their Optical and Hybridization Properties. *JACS* **2014,** *136* (43), 15195-15202.

24. Satyavolu, N. S. R.; Tan, L. H.; Lu, Y., DNA-Mediated Morphological Control of Pd–Au Bimetallic Nanoparticles. *JACS* **2016,** *138* (50), 16542-16548.

25. Chiu, C.-Y.; Ruan, L.; Huang, Y., Biomolecular specificity controlled nanomaterial synthesis. *Chemical Society Reviews* **2013,** *42* (7), 2512-2527.

26. Walsh, T. R.; Knecht, M. R., Biointerface Structural Effects on the Properties and Applications of Bioinspired Peptide-Based Nanomaterials. *Chem. Rev.* **2017,** *117* (20), 12641-12704.

27. Chen, Z.; Liu, C.; Cao, F.; Ren, J.; Qu, X., DNA metallization: principles, methods, structures, and applications. *Chem. Soc. Rev.* **2018**.

28. Pu, F.; Ren, J.; Qu, X., Nucleobases, nucleosides, and nucleotides: versatile biomolecules for generating functional nanomaterials. *Chem. Soc. Rev.* **2018,** *47* (4), 1285-1306.

29. Yamane, T.; Davidson, N., On the complexing of deoxyribonucleic acid by silver(I). *Biochimica et Biophysica Acta (BBA) - Specialized Section on Nucleic Acids and Related Subjects* **1962,** *55* (5), 609-621.

30. Berti, L.; Burley, G. A., Nucleic acid and nucleotide-mediated synthesis of inorganic nanoparticles. *Nature Nanotechnology* **2008,** *3*, 81.

31. Kondo, J.; Tada, Y.; Dairaku, T.; Hattori, Y.; Saneyoshi, H.; Ono, A.; Tanaka, Y., A metallo-DNA nanowire with uninterrupted one-dimensional silver array. *Nature Chemistry* **2017,** *9*, 956.

32. Izatt, R. M.; Christensen, J. J.; Rytting, J. H., Sites and thermodynamic quantities associated with proton and metal ion interaction with ribonucleic acid, deoxyribonucleic acid, and their constituent bases, nucleosides, and and nucleotides. *Chemical Reviews* **1971,** *71* (5), 439-481.

33. Sanchez-Iglesias, A.; Winckelmans, N.; Altantzis, T.; Bals, S.; Grzelczak, M.; Liz-Marzan, L. M., High-Yield Seeded Growth of Monodisperse Pentatwinned Gold Nanoparticles through Thermally Induced Seed Twinning. *J Am Chem Soc* **2017,** *139* (1), 107-110.

34. Davey, W. P., Precision Measurements of the Lattice Constants of Twelve Common Metals. *Physical Review* **1925,** *25* (6), 753-761.

35. Zhou, S.; Zhao, M.; Yang, T.-H.; Xia, Y., Decahedral nanocrystals of noble metals: Synthesis, characterization, and applications. *Materials Today* **2018**.

36. Xia, Y.; Gilroy, K. D.; Peng, H.-C.; Xia, X., Seed-Mediated Growth of Colloidal Metal Nanocrystals. *Angewandte Chemie International Edition* **2017,** *56* (1), 60-95.

37. Clever, G. H.; Kaul, C.; Carell, T., DNA–Metal Base Pairs. *Angewandte Chemie International Edition* **2007,** *46* (33), 6226-6236.

38. Ono, A.; Cao, S.; Togashi, H.; Tashiro, M.; Fujimoto, T.; Machinami, T.; Oda, S.; Miyake, Y.; Okamoto, I.; Tanaka, Y., Specific interactions between silver(i) ions and cytosine–cytosine pairs in DNA duplexes. *Chemical Communications* **2008,** (39), 4825-4827.

39. Ono, A.; Torigoe, H.; Tanaka, Y.; Okamoto, I., Binding of metal ions by pyrimidine base pairs in DNA duplexes. *Chemical Society Reviews* **2011,** *40* (12), 5855-5866.

40. Takezawa, Y.; Shionoya, M., Metal-Mediated DNA Base Pairing: Alternatives to Hydrogen-Bonded Watson–Crick Base Pairs. *Accounts of Chemical Research* **2012,** *45* (12), 2066-2076.

41. Swasey, S. M.; Leal, L. E.; Lopez-Acevedo, O.; Pavlovich, J.; Gwinn, E. G., Silver (I) as DNA glue: Ag+-mediated guanine pairing revealed by removing Watson-Crick constraints. *Scientific Reports* **2015,** *5*, 10163.

42. DeFord, D. D.; Hume, D. N., The Determination of Consecutive Formation Constants of Complex Ions from Polarographic Data. *Journal of the American Chemical Society* **1951,** *73* (11), 5321-5322.

43. Bard, A. J.; Faulkner, L. R.; Leddy, J.; Zoski, C. G., *Electrochemical methods: fundamentals and applications*. wiley New York: 1980; Vol. 2.

44. Yang, T. H.; Peng, H. C.; Zhou, S.; Lee, C. T.; Bao, S.; Lee, Y. H.; Wu, J. M.; Xia, Y., Toward a Quantitative Understanding of the Reduction Pathways of a Salt Precursor in the Synthesis of Metal Nanocrystals. *Nano Lett* **2017,** *17* (1), 334-340.

45. Watzky, M. A.; Finke, R. G., Transition Metal Nanocluster Formation Kinetic and Mechanistic Studies. A New Mechanism When Hydrogen Is the Reductant: Slow, Continuous Nucleation and Fast Autocatalytic Surface Growth. *Journal of the American Chemical Society* **1997,** *119* (43), 10382-10400.

46. Yang, T. H.; Zhou, S.; Gilroy, K. D.; Figueroa-Cosme, L.; Lee, Y. H.; Wu, J. M.; Xia, Y., Autocatalytic surface reduction and its role in controlling seed-mediated growth of colloidal metal nanocrystals. *Proc Natl Acad Sci U S A* **2017,** *114* (52), 13619-13624.

47. Stathis, E., Determination of silver with ascorbic acid. *Analytical Chemistry* **1948,** *20* (3), 271-271.

48. Yang, T.-H.; Peng, H.-C.; Zhou, S.; Lee, C.-T.; Bao, S.; Lee, Y.-H.; Wu, J.-M.; Xia, Y., Toward a Quantitative Understanding of the Reduction Pathways of a Salt Precursor in the Synthesis of Metal Nanocrystals. *Nano Letters* **2017,** *17* (1), 334-340.

49. Ingold, C. K., *Structure and mechanism in organic chemistry*. Cornell University Press; Ithaca; New York: 1953.

50. Demers, L. M.; Mirkin, C. A.; Mucic, R. C.; Reynolds, R. A.; Letsinger, R. L.; Elghanian, R.; Viswanadham, G., A Fluorescence-Based Method for Determining the Surface Coverage and Hybridization Efficiency of Thiol-Capped Oligonucleotides Bound to Gold Thin Films and Nanoparticles. *Analytical Chemistry* **2000,** *72* (22), 5535-5541.

51. Sun, Y.; Mayers, B.; Herricks, T.; Xia, Y., Polyol Synthesis of Uniform Silver Nanowires: A Plausible Growth Mechanism and the Supporting Evidence. *Nano Letters* **2003,** *3* (7), 955-960.

52. Feng, J.; Pandey, R. B.; Berry, R. J.; Farmer, B. L.; Naik, R. R.; Heinz, H., Adsorption mechanism of single amino acid and surfactant molecules to Au {111} surfaces in aqueous solution: design rules for metal-binding molecules. *Soft Matter* **2011,** *7* (5), 2113-2120.

53. Park, J.-W.; Shumaker-Parry, J. S., Structural Study of Citrate Layers on Gold Nanoparticles: Role of Intermolecular Interactions in Stabilizing Nanoparticles. *Journal of the American Chemical Society* **2014,** *136* (5), 1907-1921.

54. Jadzinsky, P. D.; Calero, G.; Ackerson, C. J.; Bushnell, D. A.; Kornberg, R. D., Structure of a Thiol Monolayer-Protected Gold Nanoparticle at 1.1 Å Resolution. *Science* **2007,** *318* (5849), 430.

55. Battocchio, C.; Meneghini, C.; Fratoddi, I.; Venditti, I.; Russo, M. V.; Aquilanti, G.; Maurizio, C.; Bondino, F.; Matassa, R.; Rossi, M.; Mobilio, S.; Polzonetti, G., Silver Nanoparticles Stabilized with Thiols: A Close Look at the Local Chemistry and Chemical Structure. *The Journal of Physical Chemistry C* **2012,** *116* (36), 19571-19578.

56. Lofton, C.; Sigmund, W., Mechanisms Controlling Crystal Habits of Gold and Silver Colloids. *Advanced Functional Materials* **2005,** *15* (7), 1197-1208.

CHAPTER 3: KINETIC RECONSTRUCTION OF DNA PROGRAMMED PLASMONIC METAL NANOSTRUCTURES WITH PREDICTABLE SHAPES AND OPTICAL PROPERTIES

3.1 Introduction

Plasmonic metal nanostructures have found wide applications in sensing,[1-2] catalysis,[3] spectroscopy[4] and therapy.[5] The functional properties of those nanostructures are closely related to their structural features such as size, shape and composition.[6-7] The ultimate goal is to rationally engineer plasmonic metal nanostructures with sets of structural parameters that lead to desired functions for the specific application. However, there are two major challenges to achieve this goal. On the one hand, it has been difficult to predict the exact structural outcome of a synthetic method, because the synthetic reactions often have kinetic complications, which cause the prediction to deviate from the set of parameters determined by the thermodynamic equilibrium state.[8] Significant challenges remain in controlling and predicting the entire kinetic process of the structural evolution. On the other hand, it has been difficult to precisely predict the functions of the resulting nanostructures because one functional parameter often relates with multiple structural parameters, and those structural parameters often evolve concurrently during the growth of nanostructures.[9-10] For example, the increase of the longitudinal dimension of Au nanorods is accompanied by the increase in diameter and constant changing in surface concaveness,[11] all of which are closely related with their longitudinal localized surface plasmon resonances (LSPR).[12] To predict the combinations of the structural and functional parameters in the final products, we need to understand and control their kinetic evolution pathways. While there were many studies on the effect of structural parameters such as size, aspect ratios, and shell thickness of plasmonic nanostructures on one functional parameter,[6-7, 13-16] more research is

needed to deconvolute the tangled relationships between each functional parameter and multiple relevant structural parameters as the nanostructures grow. Understanding and predicting the co-evolution of structures and functions during nanostructure growth will not only allow us to design the precise functions of the final nanostructures, but also give us access to numerous combinations of structural and functional parameters in the kinetic intermediate structures.

Using capping ligands is proven to be an effective way to control the kinetic process during the synthesis of metal nanostructures.[17-18] However, predictive control of the kinetic evolution of nanostructures using capping ligand is yet to be achieved. Among variety of capping ligands, DNA has been shown to have superior control over the evolution of metal nanostructures.[19-24] The programmability of DNA enables it to tune the reduction potential and the reduction kinetics of the metal ion precursors, as well as the rate for atom addition and diffusion on the metal surface by varying the DNA sequence.[24-25] Herein, we used DNA controlled growth of Au-Ag core-shell nanostructures as a model system to showcase the power of kinetic control in generating novel nanostructures with predictable shapes and plasmonic properties. Au supported Ag nanostructures have been intensively studied in the past few years because it combined the superior electric field enhancement of Ag and great size and shape tunability of Au nanostructures.[26-28] We systematically analyzed the evolution of two structural parameters - tip angle and aspect ratio, in the growth of Au-Ag nanostructures controlled by two different DNA sequences. We also established the relationships between the evolving structures with several functional parameters related to their plasmonic properties. The structure-function relationship of the evolving nanostructures allowed us to access a continuous spectrum of functional features controlled by the time of reaction progression. The kinetic evolution pathways of the two structural parameters were found to be both concurrently and independently

controlled by DNA at different phases of the growth. As a result, we could produce new nanostructures by exchanging DNA sequences in the growth environment which also exchanged their kinetic evolution pathways. The structural and functional parameters of the resulting structures could be predictively tuned by the timing of the exchange. The results demonstrated that by understanding the kinetic evolution of the structural parameters and their relationships with the function parameters, it is possible to design the precise combination of structural and functional parameters in the nanostructured products of a synthesis reaction.

3.2 Results and discussion

3.2.1 Structural descriptions of DNA controlled Au-Ag nanostructures

The Au-Ag nanostructures were synthesized by a seed-mediated method. We chose Au bipyramid as seeds for two reasons. On the one hand, compared with simpler crystal structures, bipyramids have highly stepped facets and twin planes.[29-30] The structural defects in bipyramids can act as powerful kinetic driving forces for the crystals to develop into structures that are out of thermodynamic equilibrium. On the other hand, bipyramids also have strong local field enhancement owning to their sharp tips.[15, 26] Therefore, to use bipyramids as the base for silver structure growth also opens up the opportunity for interesting optical properties of the resulting structures.

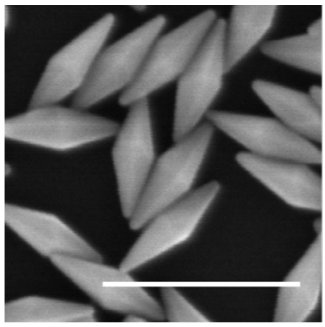


Figure 3.1: SEM image of bipyramid seed. Scale bar: 200 nm.

Au bipyramid was synthesized according to the method reported by Sánchez-Iglesias et al.[31](Fig. 3.1) The average length of bipyramid was 131.05 ± 4.84 nm, the average width was 38.42 ± 1.99 nm.

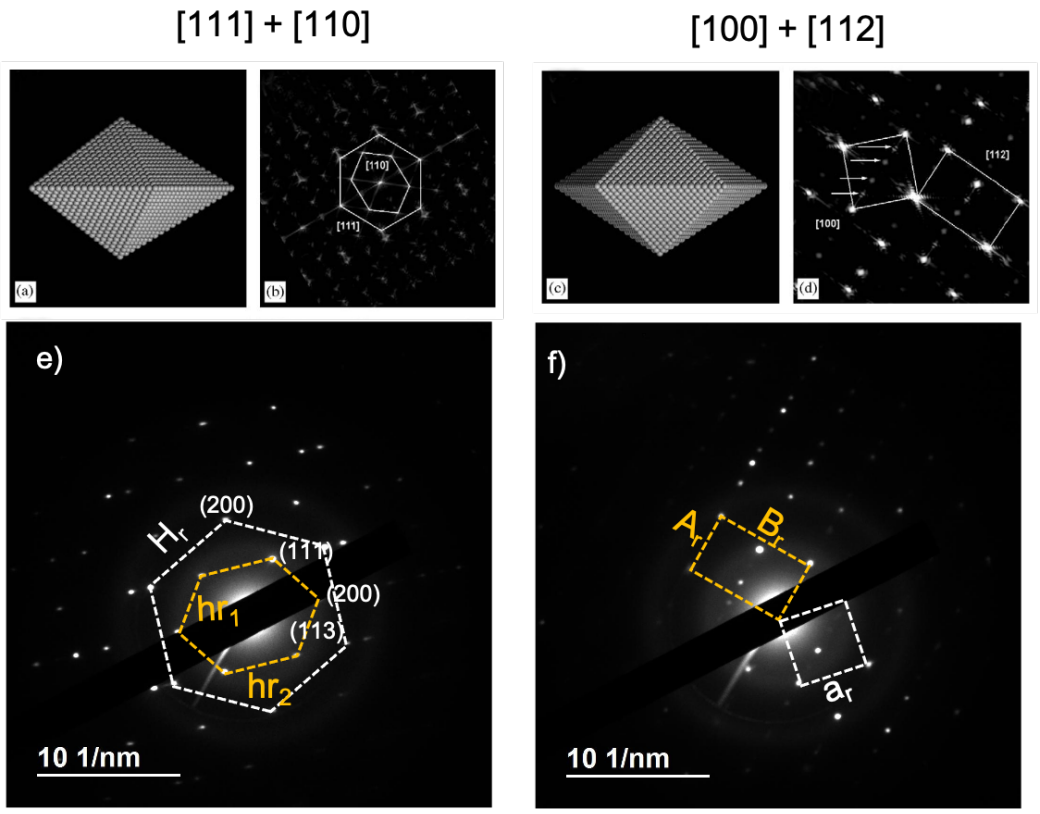


Figure 3.2: 3d projection of decahedron and simulated SEAD pattern from a) b) [100] and [112] zone axes and c) d) [100] and [112] zone axes.[32] Experimental SEAD pattern of A20 nanostructure from e) [100] and [112] zone axes and f) [100] and [112] zone axes.

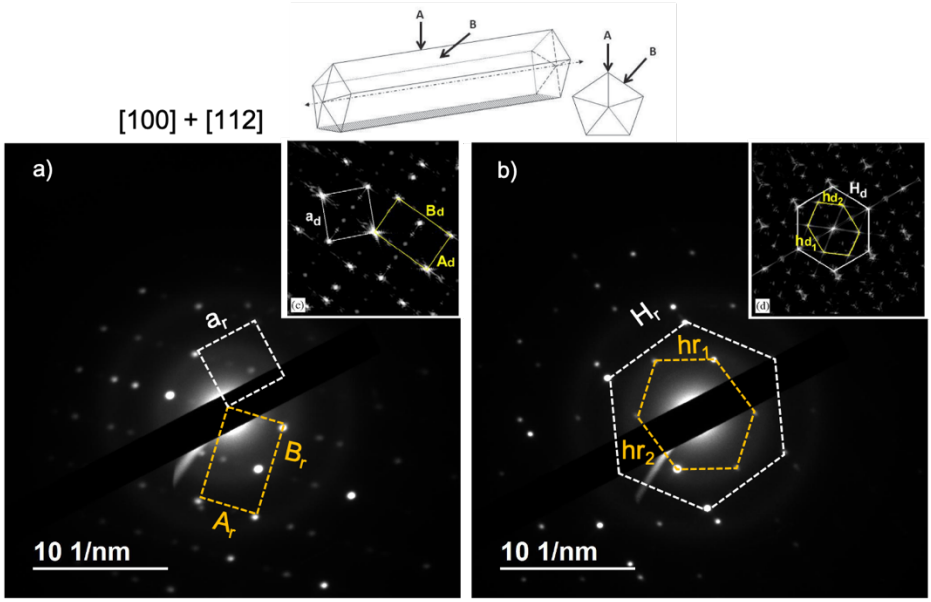


Figure 3.3: SEAD pattern of C20 nanostructure from a) [100] and [112] zone axes and b) [100] and [112] zone axes. Insets are simulated SEAD pattern of pentatwinned rod from litereature.[32]

Ag shells were overgrown onto the bipyramid core using silver acetate as the precursor and ascorbic acid as the reducing agent. Twenty bases long single stranded DNA A20 and C20 were used as capping ligands to direct the growth of nanostructures. As shown in Fig. 3.4f, g, the structures produced with A20 have truncated diamond shapes. To probe the internal structure of the nanocrystals, we compared the selected area diffraction (SEAD) pattern of the A20 produced structures (Fig. 3.2e, f) with the reported simulated pattern of a decahedron (Fig. 3.2b, d). A20 controlled structures exhibited similar SEAD patterns as that of a decahedron, which indicates A20 structures preserve the five-folded twin planes from the bipyramid seed. The A20 structures were also more elongated along the longitudinal axis compared with a decahedron, which indicates A20 structures also possess the stepped side facets inherited from the bipyramid core. On the other hand, C20 produced rod shape as shown by Fig. 3.4m, n). The geometry and SEAD pattern of C20 derived structures (Fig. 3.3a,b) correlated well with that of the penta-twinned gold

and silver nanorod (Fig. 3.3 insets). Therefore, C20 derived structures should be ascribed to the same penta-twinned rod structure with five {100} side facets and ten {111} end facets[33].

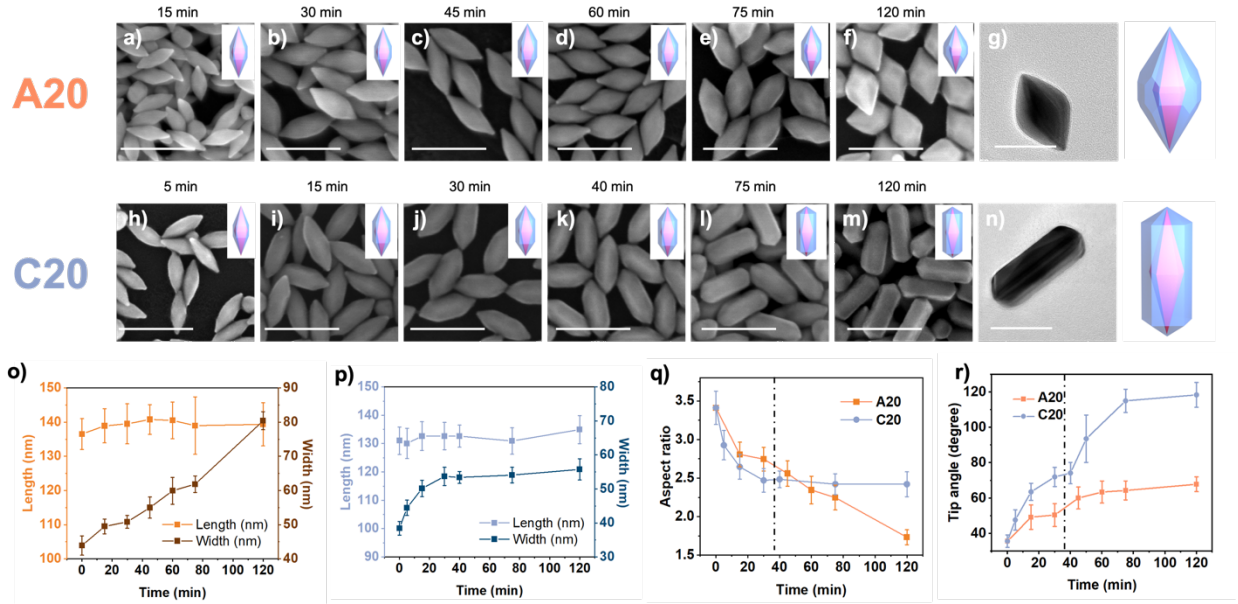


Figure 3.4: Size and shape evolution of Au-Ag nanocrystals synthesized with A20 and C20 sequences. SEM images and TEM micrographs of Au−Ag core−shell NPs formed at different time points in the presence of (a−g) A20, (h−n) C20, and their representative 3D models. Scale bars are 200 nm in SEM (a-f, h-m) images and 50 nm in TEM micrographs (g, n). o) Length (left, orange) and width (right, brown) of nanocrystals synthesized with A20 as a function of time. p) Length (left, light blue) and width (right, dark blue) of nanocrystals synthesized with C20 as a function of time. q) Aspect ratio of nanocrystals synthesized with A20 (orange) and C20 (blue) as a function of time. r) Tip angle of nanocrystals synthesized with A20 (orange) and C20 (blue) as a function of time. The dashed line in d) and q) marked the transition between the phase one and phase two.

The growth for A20 and C20 likely involve highly complicated mechanisms and multiple kinetic intermediate structures. To understand the kinetic evolution of the structures, we performed scanning electron microscope (SEM) characterizations on the intermediate structures

at different reaction times. Fig. 3.4 demonstrated the size and shape evolution of Au-Ag nanocrystals synthesized with A20 and C20 sequences. As shown in Fig. 3.4a-g, A20 directed Ag deposition first took place on the side facets of the bipyramid seeds (Fig. 3.4a-c). Then followed by significant growth of Ag shell towards the transversal direction, eventually led into the decahedral shaped products that has sharp longitudinal tips (Fig. 3.4d-f). C20 controlled Ag shell growth exhibited similar growth patterns as that of A20 at early time points (Fig. 3.4h-k) during which the growth primarily took place on the side facets of the bipyramids. However, at later time points (Fig. 3.4l, m), the Ag shell kept expanding along the longitudinal axis ([100] direction) which resulted in rod shaped structures. To quantitatively describe the evolution of the size and shape of the nanocrystals, we introduced four descriptors. Length and width were the dimensions of the nanocrystals along the longitudinal and transversal axis of the bipyramid. Aspect ratio was calculated by the length divided by the width. Tip angle was defined by the two tangent lines that originated from the vertex of the longitudinal ends intersecting with the periphery of their neighboring side facets in 2D projections. As shown in Fig. 3.4o, A20 controlled structures increased significantly in width (brown, right) as they grew, whereas their length remained rather constant (orange, left). On the other hand, the width for C20 controlled structures increased until 30 min, then remained constant (Fig. 3.4p, dark blue, right), whereas their length remained constant the whole time. As a result, the aspect ratio of A20 kept dropping overtime (Fig. 3.4q, orange) but the aspect ratio of C20 dropped until 30 min then remained constant (Fig. 3.4q, blue). Interestingly, the change of tip angles exhibited opposite trend as the change of the aspect ratios. The tip angle of A20 increased until 45 min, then kept constant (Fig. 3.4r). In contrast, the tip angle of C20 kept increasing throughout the course of the reaction (Fig. 3.4r). The rate of increasing in the tip angle for C20 seemed to reach a “steady state” at 40 min,

which coincided with the stopping time for tip angle increase for A20 directed growth. The tip angle for the final A20 structures (120 min) was also strikingly consistent with the tip angle of the "steady state" in C20 structures. The quantitative structural analysis unraveled the distinctively different kinetics in A20 and C20 controlled growth. The growth could be separated into two phases, marked by 30-40 min as the switching point for the kinetic pathway controlled by both sequences. In phase one, nanostructures grown in the presence of A20 and C20 exhibited similar growth behavior involving increase in both widths and tip angles. However, in the second phase that followed, A20 controlled structures kept increasing in widths but stopped increasing in tip angles, whereas C20 controlled structures kept increasing in tip angles but stopped increasing in widths. The coincidence of the kinetic transition point for the changing rate of aspect ratios and tip angles strongly indicates there may be key transitional structures that intersect both A20 and C20 directed evolution pathways. Fig. 3.6 shows the distribution of aspect ratios and tip angles for all the intermediate structures grown with A20 and C20. The tip angles and aspect ratios for A20 and C20 structures distributed on the same line on the structural map for tip angles less than 74 degree and aspect ratio larger than 2.5, which corresponded to the structural parameters in phase one. This result strongly suggests that A20 and C20 follow a common structural evolution pathway in the early stage of the growth. For more detailed discussion on the growth mechanism, see section 3.2.5.

3.2.2 Optical properties of DNA controlled nanostructures

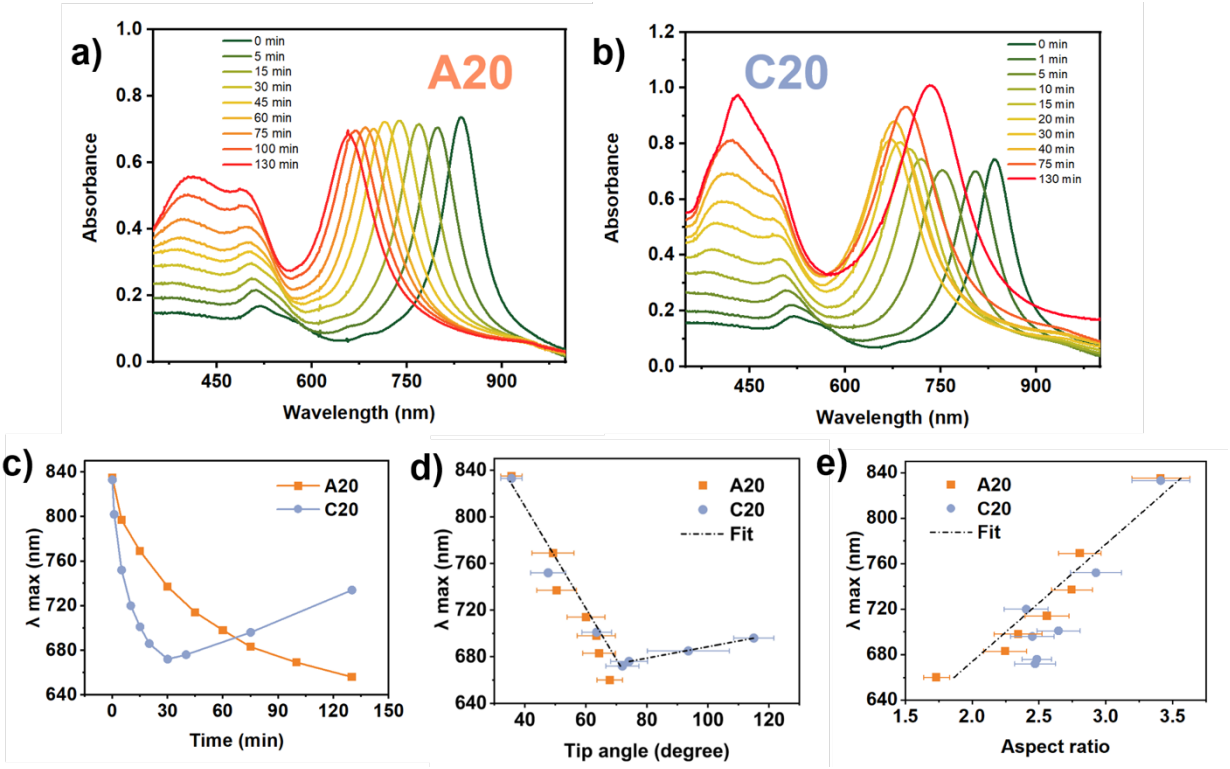


Figure 3.5: Extinction spectra of Au-Ag nanostructures synthesized with a) A20 and b) C20 sequences at different time points. c) Wavelength of longitudinal dipolar plasmon resonance peak as a function of time. d) Relationship between the wavelength of longitudinal dipolar plasmon resonance peak and d) the tip angle and e) the aspect ratio.

Optical properties of nanostructures are highly dependent on their shape and size. We investigated the optical properties of the Au-Ag structures and aimed to derive the relationship between their structures and their optical properties. Fig. 3.5a, b shows the extinction spectra of Au-Ag nanostructures at different time points. In the spectrum of the bipyramid seed (0 min, dark green), the peak at 835 nm could be ascribed to the longitudinal plasmon mode and the peak at 520 nm could be ascribed to the transverse plasmon mode, respectively.[30] In A20 structures, the wavelength of the longitudinal peak kept blue shifting as the nanostructures grew (Fig. 3.5c), whereas the intensity of the peak remained constant. The intensity of the transverse peak also

increased over the course of the reaction. On the other hand, in C20 directed growth, the wavelength of the longitudinal peak first blue shifted then red shifted, with a turning point of 30 min (Fig 3.5c). The intensity of both the longitudinal peak and the transverse peak increased overtime. We then tried to correlate the change of optical properties with the evolution of their corresponding structures. We focus the discussion on the position of the longitudinal plasmonic peak (λ max) as it exhibited a two-phase transitional behavior that is similar to that in the evolution of the structures. Fig. 3.5d shows the relationship between λ max and the tip angle of their corresponding structures. λ max decreased with increasing tip angles until 74 degree, then λ max started to increase with increasing tip angles. The tip angles for structures grown with A20 were exclusively less than 74 degrees, which resided in the region of monotonic decrease of λ max. Additionally, Fig. 3.4r shows that the tip angle of A20 structures monotonically increased overtime. Therefore, the change of the tip angle of A20 structures correlated well with the continuous blue shifts of λ max in Fig. 3.5a. On the other hand, the distribution of tip angles of C20 structures expanded beyond the switching point in Fig. 3.5d. Fig. 3.4r also shows that the tip angle of C20 structures monotonically increased overtime. As a result, the λ max of C20 structures in Fig. 3.5b followed the relationship in Fig. 3.5d, first blue shifted then red shifted as the nanostructures increased in tip angles. The observation could also be supported by the same time point that corresponded to the turning of λ max for C20 in Fig. 3.5c and a tip angle of 74 degrees in Fig. 3.4r and Fig. 3.5d. Fig. 3.5e shows the relationship between the λ max and the aspect ratio. The λ max increased as the aspect ratio increased for both A20 and C20 structures. Both A20 and C20 controlled nanostructure growth experienced decrease in aspect ratio as the width expanded (Fig. 3.4q). However, the aspect ratio of C20 structures stopped decreasing at 30 min whereas the aspect ratio of A20 structures kept decreasing until the structures stopped

growing. Therefore, the decrease in aspect ratio contributed to the blue shifts of λ max for the spectra of both A20 and C20 structures until 30 min, but only affected A20 spectra after 30 min. The switching between monotonic decrease and monotonic increase of λ max as the tip angle increased is extremely intriguing to us. Especially the switching time and corresponding tip angles coincided with the transition point between phase one and phase two in the structural evolution. We tried to figure out the origin of the switching from the relationship between the λ max and the aspect ratio. It has been reported that the λ max exhibited linear relationship with the aspect ratio (R) in Au nanorods,[34-35]Au bipyramids,[6] silver nanobars and nanorices.[36] The linear fit between λ max and the aspect ratio gave the relationship of λ max = 103.09 R + 4.54 (R^2 = 0.93) (equation 1) (Fig. 3.5e), indicating the trend is also true in the Au-Ag structures. As shown in Fig. 3.6, the aspect ratio decreased linearly as the tip angle (A) increased until 74 degree for both A20 and C20 structures, which corresponded to phase one in the structural evolution. Therefore, we speculated that the monotonic decrease of λ max at tip angles less than 74 degree in Fig. 3.5c was mainly caused by the decreased aspect ratios. On the other hand, the monotonic increase of λ max after 74 degrees was solely caused by the increase of the tip angle because only C20 structures in phase two developed tip angles larger than 74 degrees, and all C20 structures in phase two had the same aspect ratio (Fig. 3.6). Therefore, the quantitative relationship between λ max and the tip angle could be derived by fitting the Fig. 3.5d at the region where the tip angles were larger than 74 degrees. The relationship was λ max = 0.49 A + 1307 (R^2 = 0.99) (equation 2). We also fitted the region where the tip angles were smaller than 74 degrees based on the assumption that the wavelength shift at this region was entirely caused by the decrease in aspect ratios. Based on the relationship of ΔR = - 0.036 ΔA (Fig. 3.6, A < 74°), We found a relationship of Δλ max = 122.27ΔR, which indicated λ max changed slightly

faster than the effect from the aspect ratio alone (equation one). This deviation could come from the synergistic effect of material change from Au to Ag. It has been reported that when Ag was coated onto Au, the plasmonic peak of Au core experienced blue shifts as the optical properties of Au was gradually overshadowed by that of Ag. However, this transitional effect vanished after the Ag shell was thicker than 5 nm.[26, 37] To corroborate our explanation, we performed Discrete Dipole Scattering (DDSCAT) simulations for structures with different tip angles. In our simulation model, we used the dimensions of the final structure grown with C20 and systematically varied its tip angle. Using an idealized geometric model in the simulation allowed us to keep a constant aspect ratio while varying the tip angle, hence to deconvolute the effect from different structural parameters. Fig. 3.7a showed the result of the simulation. The longitudinal plasmonic peaks for structures with tip angles smaller than 74 degrees were significantly broadened and attenuated, which could be due to insufficient dipole scattering at thinner shells for sharp tips, similar to the early stage of the growth of Ag shell. The position of the peak blue shifted until 74 degrees then red shifted as the tip angle increased, which was consistent with our hypothesis that material change contributed to the additional blue shifts of λ max for tip angles less than 74 degree. We further plotted the simulated λ max as a function of the tip angle for tip angles larger than 74 degree (Fig. 3.7b). The λ max increased linearly with the tip angle, which was consistent with our experimental observations for tip angles larger than 74 degrees (Fig. 3.5d). We did not seek for quantitative agreement for the relationship between λ max and tip angles between the experimentally derived values and that from DDSCAT simulations. Because the structural models we used in DDSCAT were highly idealized, they might not have the exact experimental counterparts. Overall DDSCAT simulations and the fitting of the experimental data agreed with our hypothesis that the red shift of the longitudinal

wavelength was dominated by the increase of tip angles for tip angles larger than 74 degrees, and was dominated by the decrease of the aspect ratio for tip angles less than 74 degrees. The analysis not only deconvoluted the relationship between λ max and the two structural parameters, but also highlighted the relative contributions from the two structural parameters in affecting λ max in different kinetic and geometric domains, which is important to help identifying the most effective structural parameter in functional tuning. This quantitative model will be used to predict λ max for kinetically reconstructed structures in the next section.

The insights in the effect of tip angles and aspect ratios on λ max could help us better understand the change of λ max as a function of time (Fig. 3.5c). λ max of C20 structures rapidly decreased until 30 min, as a result of decrease in aspect ratios during this period of growth. After 30 min, the increase of λ max is solely determined by the increase of tip angles in the monotonic increasing region of Fig. 3.5d. Hence the λ max exhibited a two-phase switching behavior that correlated with the two-phase transition in structural evolution. On the other hand, the λ max of A20 structures kept decreasing, which was consistent with the monotonic decrease in aspect ratios in the structural evolution (Fig. 3.4q). The tip angles of A20 structures never exceeded 74 degree so there was no reverse effect in the change of λ max. The change of λ max for A20 structures was slower than that of C20 structures before 30 min, which could be explained by their slower decrease in aspect ratio in phase one of the structural evolution (Fig. 3.4q, r).

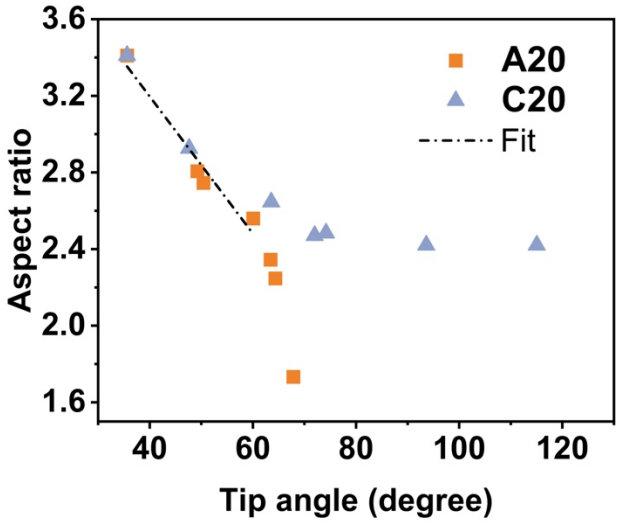


Figure 3.6: Relationship between aspect ratio and tip angle.

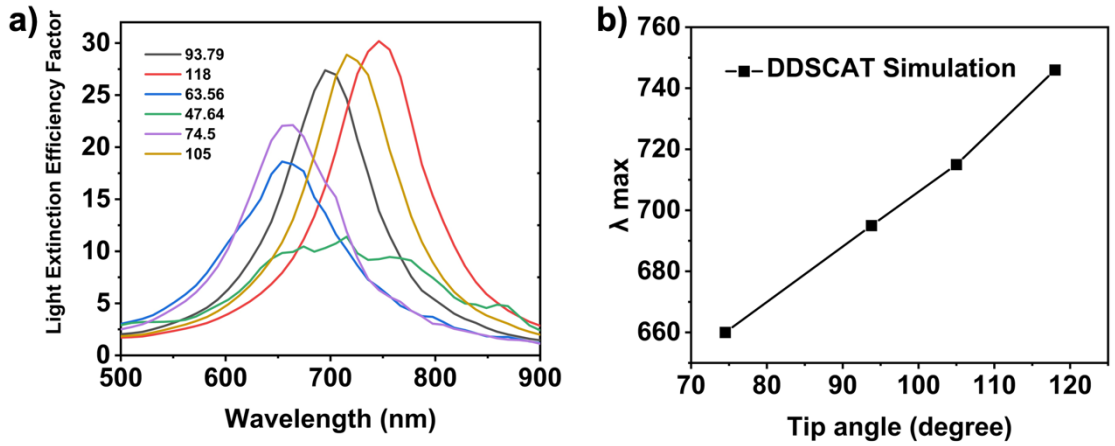


Figure. 3.7: a) DDSCAT simulation on longitudinal wavelength for structures at different tip angles (legends). b) Relationship between the wavelength of simulated longitudinal plasmonic peak and the tip angles.

Besides the wavelength for longitudinal peaks, tip angles and aspect ratios also determined the extinction of longitudinal peaks and that of the transverse peaks. We used the ratio between the extinction of the transverse peak (T) and that of the longitudinal peak (L) as the functional parameter to relate to the two structural parameters. As shown in Fig. 3.8a, the T / L

extinction ratio monotonically increased as the tip angle increased. On the other hand, the T / L extinction ratio decreased with increased aspect ratio for A20 structures (Fig. 3.8b). However, C20 structures with the aspect ratio of 2.5 have several T / L extinction ratios, which were the structures in phase two of the growth. Those structures all have the same aspect ratio but different tip angles, which resulted in different T / L extinction ratios. Those results suggested the stronger influence of the tip angle on the T / L extinction ratio compared with the effect of the aspect ratio. The precise control of T / L extinction ratio is important in polarization dependent applications such as plasmon-enhanced fluorescence and plasmon induced photothermal effects.[38-39]

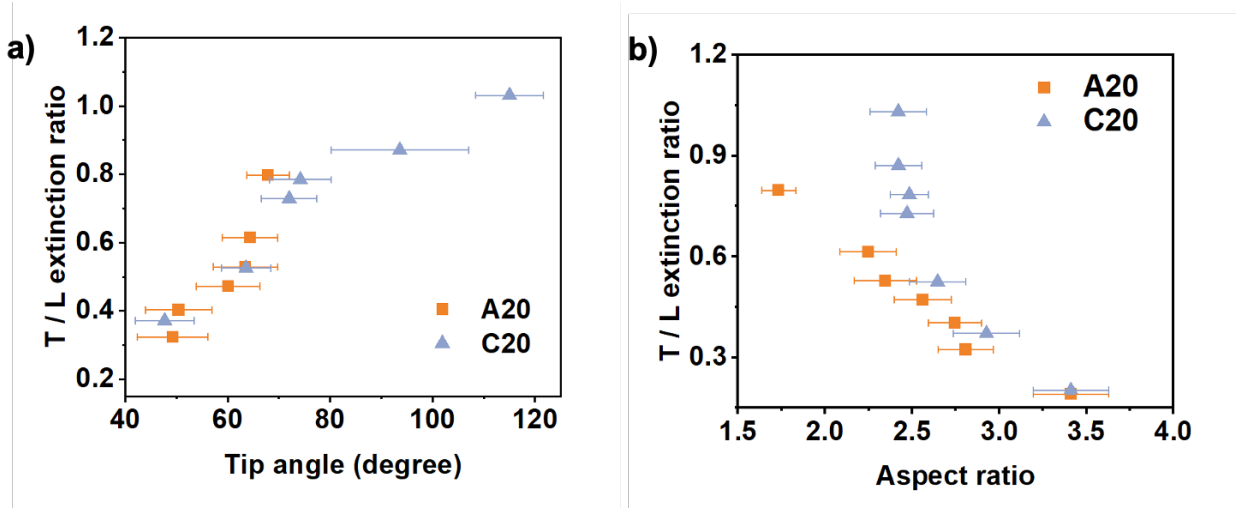


Figure 3.8: Ratio of the extinction of transverse plasmonic peaks (T) and longitudinal plasmonic peak (L) as a function of a) tip angles and b) aspect ratios.

In summary, the key relationships between optical properties and structural parameters are as follows. In phase one, the decreased aspect ratios for structures grown with both A20 and C20 caused the longitudinal peaks to blue shift. In phase two, A20 structures continued to decrease in aspect ratios hence the blue shifts went on. However, the aspect ratios for C20

structures stopped changing in phase two. As a result, the increase in tip angles became the dominate effect which caused the peak to red shift.

3.2.3 Kinetic reconstruction of Au-Ag nanostructures

Both A20 and C20 introduced unique growth mechanisms in Au-Ag nanostructures. The relative rate for the decrease in aspect ratios and increase in tip angles produced a variety of intermediate structures that have precise combinations of the two structural parameters. More intriguingly, those structural parameters quantitatively correlated with the optical properties of the nanostructures. The control of the DNA sequences in the kinetic evolution of the nanostructures offers tremendous opportunities to predictably construct new structures and their optical properties. If we can nudge the kinetic evolution pathway from that of one DNA sequence to another, the rate of changing the structural parameters will also be altered correspondingly, thereby generating different combinations of the structural parameters in the end products. The geometry of the reconstructed nanostructures as well as their optical properties should also be predictable based on the timing for changing the kinetic pathways. To test this exciting hypothesis, we isolated the intermediate structures from the growth in the presence of one DNA sequence, then transferred them to the growth environment in the presence of another sequence. To ensure close-to-completion ligand exchange, all the intermediate structures were washed three times in the presence of the second sequence, and the washed particles were also incubated in the presence of the second sequence for overnight. The regrowth with the exchanged sequence was left to completion.

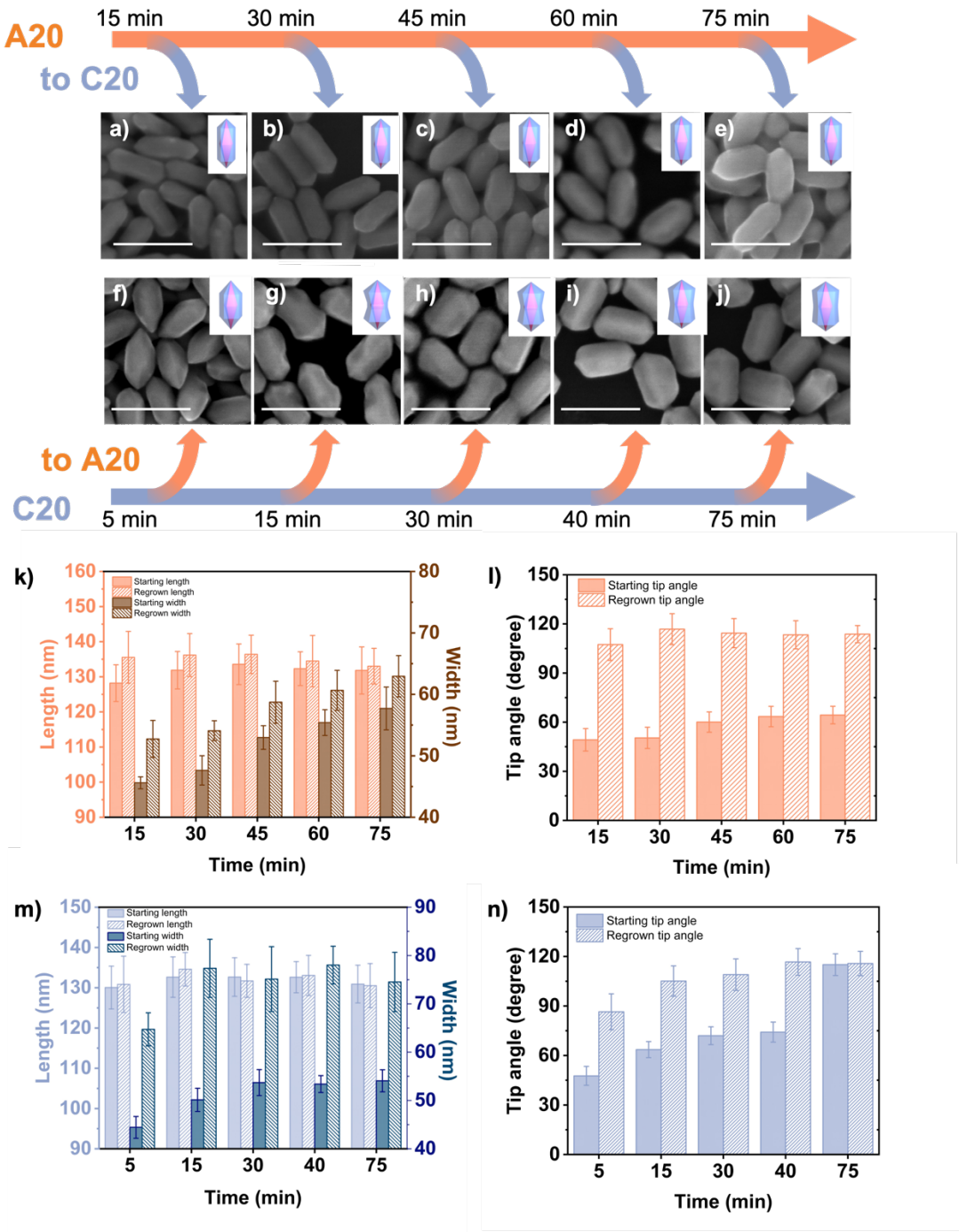


Figure 3.9: Size and shape of kinetically reconstructed Au-Ag nanocrystals with A20 and C20 sequences. SEM images of Au−Ag core−shell NPs formed by performing sequence exchange at different time points (a−e) A20 to C20 exchange, (f−j) C20 to A20, and their representative 3D models. Scale bars are 200 nm. k-n) Quantitative descriptions of structural parameters for all

Figure 3.9 (cont.): reconstructed structures. k,l) Length (k, orange) and width (k, brown) and tip angles (l) of nanocrystals formed by A20 to C20 sequence exchange. m,n) Length (m, light blue) and width (m, dark blue) and tip angles (n) of nanocrystals formed by C20 to A20 sequence exchange.

Fig. 3.9 shows the reconstructed nanostructures grown from the intermediate structures isolated at different time points. The structures regrown in the presence of C20 generally exhibited rod shapes similar to that grown with C20 alone (Fig. 3.9a-e), even though they started from the A20 intermediate structures. This observation suggested the kinetic evolution pathway was successfully altered by changing the sequence in the growth environment. Fig. 3.9k and l show the quantitative structural comparison between the starting structures isolated from the growth with A20 (solid bars) and that of the structures regrown with C20 (striped bars). Other than a slight increase in widths (striped brown), most of the regrown structures had similar dimensions as that of their starting structures (Fig. 3.9k), but their tip angles increased significantly (Fig. 3.9l), which were consistent with the effect of C20 in the phase two of the structural evolution. The starting structures came from A20 directed growth, some of which had larger widths than any structures grown with C20 alone. As a result, the regrown structures had similar tip angles as that of C20 structures but with wider widths. Notice that only the regrown structures originated from the A20 intermediate structures isolated at 15 min and 30 min exhibited similar dimensions as that of the final structures grown with C20 alone. The structures regrown from A20 intermediate structures of 45 min and later all exceeded C20 final structures in width. Coincidentally, 30 min to 40 min marked the transition between the phase one and the phase two in the structural evolution. Those results indicate that if the sequence exchange is applied in phase one, the structural evolution may be directed into that of the phase two of the

second sequence, the effect of the first sequence was almost negligible. However, if the sequence exchange is applied in phase two, new structures can be produced that have combinatorial effects from both sequences. The precise combinations of the width and the tip angle depend on the timing of the exchange. The structures reconstructed with A20 exhibited more interesting behaviors. As shown in Fig. 3.9f, the structures regrown from the C20 intermediate structures isolated at 5 min exhibited similar sharp tips as the structures grown with A20 alone, which indicated the pathway for the structural evolution was successfully altered. However, the structures grew from intermediate structures of 15 min and 30 min (Fig. 3.9g, h) had bulging belts around the two longitudinal ends of the structures. The bulging belts were not as significant in the structures regrown from the later time points (Fig. 3.9i, j). The end-bulged structures were clearly not observed before and were very likely to be produced by the additive kinetic effect from both C20 and A20 sequences, which highlighted the power of kinetic reconstruction in generating new structures. Interested readers might refer to the section 3.2.5 for more discissions on the formation mechanisms for those end-bulged structures. The quantitative analysis of dimensions (Fig. 3.9m) and tip angles (Fig. 3.9n) of C20 to A20 reconstructed structures showed opposite trends as that of A20 to C20. The widths of the structures regrown with A20 (striped dark blue) were significantly larger than their starting structures (solid dark blue). The tip angles of the regrown structures also increased compared with their starting structures, but the increase was not as significant as that of A20 to C20 regrowth (Fig. 3.9l). The structural change of C20 to A20 regrowth generally agreed with the kinetic effect of A20 in phase two, that was to increase the width but keep the same tip angles. However, the structural evolution pathway for C20 to A20 transitions was not as well defined as that of A20 to C20 transitions. The structures regrown from as early as 15 min already deviated from the structures grown with A20 alone, which was

earlier than the transition time point between phase one and phase two. This could potentially be due to the residual effect from C20 sequences, as it has stronger affinity towards Ag metal than that of A20.[24]

3.2.4 Optical properties of kinetically reconstructed Au-Ag nanostructures

By exchanging DNA sequences in the growth environment, the structural evolution pathways of the nanostructures could be altered in a predictable manner. The precise combinations of the structural parameters in the regrown structures could also be controlled depending on the timing of the exchange. We then sought to investigate the optical properties of the regrown structures. In section 3.2.2, we derived the quantitative relationship between λ max and the two structural parameters. We also qualitatively discussed the relationship between the T / L extinction ratio and the two structural parameters. We wonder whether we could use the known structure-function relationships to understand and predict the optical properties of the regrown structures, which points toward the ultimate dream of functional prediction from synthetic design.

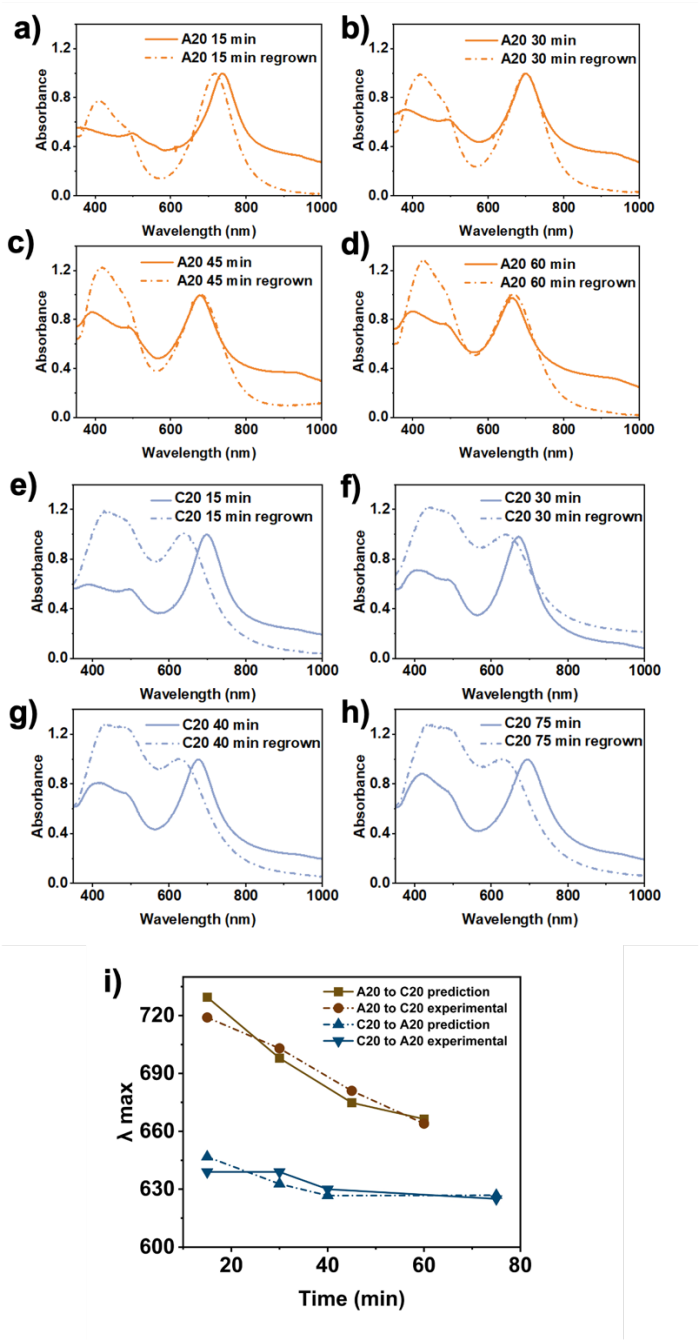


Figure 3.10: Optical properties of kinetically reconstructed Au-Ag nanocrystals with A20 and C20 sequences. UV-vis spectra of starting structures (solid lines) and regrown structures (dashed lines) for a-d) A20 to C20 kinetic transitions and e-h) C20 to A20 kinetic transitions. The spectra were normalized according to the extinction of the longitudinal peaks. i) Experimentally

Figure 3.10 (cont.): determined (solid lines) and predicted (dashed lines) λ max of the structures from A20 to C20 regrowth (brown) and C20 to A20 regrowth (dark blue).

We compared the extinction spectra of the regrown structures with that of their starting structures. The longitudinal peaks for the structures derived from A20 to C20 regrowth had minimal shifts compared with their starting structures. The main kinetic effect for C20 in the structure regrowth was to increase their tip angles, accompanied by a slight increase of widths (Section 3.2.3). The red shifts caused by the increased tip angle might be compensated by the blue shifts caused by the decrease of the aspect ratio, hence the λ max could remain unchanged. Additionally, regrown structures also exhibited significant increase in the extinction of the transverse peaks compared with that of their longitudinal peaks (Fig. 3.10a-d). According to Fig. 3.6a, the ratio between transverse extinction and longitudinal extinction increased as the tip angle increased, which explained the experimental observation. On the other hand, the longitudinal peaks for the structures derived from C20 to A20 blue shifted compared with their starting structures, and their transverse peaks also significantly increased in intensity (Fig. 3.10e-h). The main effect for A20 to direct the regrowth was to decrease the aspect ratio, and the decreased aspect ratio was known to cause the blue shifts of λ max (Fig. 3.5e), hence the blue shifts of the longitudinal peaks were understandable. The increased intensity of the transverse peak could also be explained from the decreased aspect ratio, as the decrease of the aspect ratio was correlated with increasing T / L extinction ratio (Fig. 3.8b).

The spectral change of the regrown structures qualitatively agreed with our expectation, we then sought to quantitatively correlate the change of λ max with their corresponding structural parameters. Previously, we have derived the quantitative relationships between λ max and the aspect ratio (λ max = 103.09 R + 4.54), and between λ max and the tip angle (λ max =

0.49 A + 1307, A > 74). Because all regrown structures experienced decrease in aspect ratios and increase in tip angles to some extent, we want to use the previously derived structure-function relationships to predict the λ max of the regrown structures based on the additive effect from the changing of both structural parameters. The effect of material changes for tip angles less than 74 was neglected in the calculation because it was a transitional effect that only affected some structures regrown from early time points when the Ag shell was extremely thin. Moreover, the change of aspect ratio dominated at the region when the material change took effect. Fig. 3.10 i showed the λ max of the predicted value based on the structural parameters of the regrown nanostructures for both A20 to C20 transitions and C20 to A20 transitions. The predicted λ max agreed well with the experimentally determined values, even for the structures with end-bulged structures (Fig. 3.9g, h). This result strongly suggests that the tip angle and the aspect ratio are the two most important parameters that determine the λ max in a penta-twinned Au-Ag core-shell structure. And the relationships between the structural parameters and functional parameters in the regrowth process were consistent with that in the primary growth. The analysis not only deconvoluted the relationships between λ max and the two structural parameters, but also highlighted the relative contributions from the two structural parameters in affecting λ max in different kinetic and geometric domains. The predictable relationships between the structural evolution and their corresponding functional properties enable design of kinetic paths towards targeted functional nanostructures.

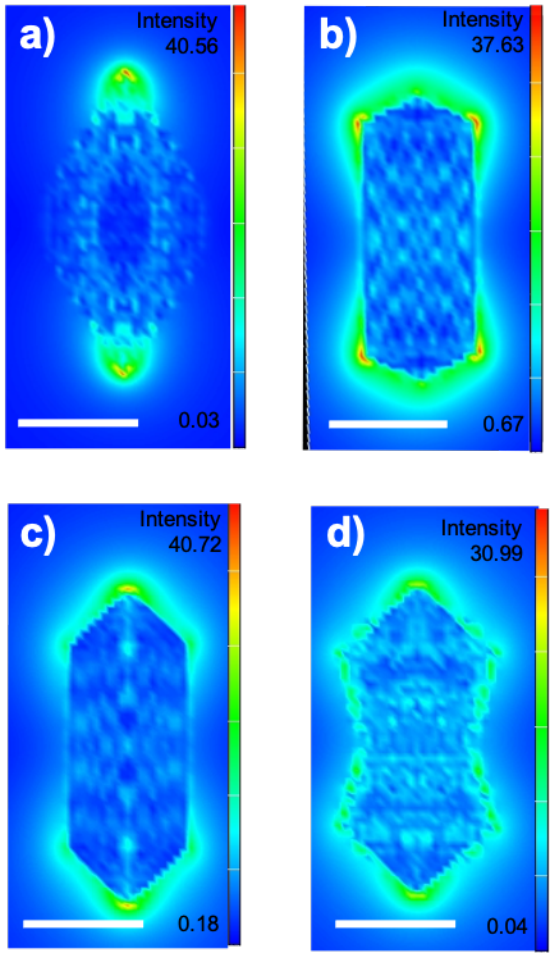


Figure 3.11: Simulated spatial distribution of near electric field intensity of Au-Ag nanostructures excited at their corresponding λ max. The structures were synthesized with a) A20 only (120 min), b) C20 only (120 min), c) A20 to C20 transition (45 min) and d) C20 to A20 transition (15 min). The polarization was along the longitudinal direction. The dimensions of the particles were set as the same as the experimental dimensions. Scale bar: 50 nm. The map was simulated by DDSCAT.

The structures of the nanocrystals not only affect the far field optical properties such as the location and intensity of LSPR, but also affect their near field properties such as near electric field enhancement. Near electric field enhancement is important in applications such as Surface-Enhanced Raman Scattering (SERS) because the intensity of the Raman signal scales with the

fourth power of the local electric field.[40] Fig. 3.11 shows the simulated distribution of near electric field for the nanostructures synthesized either with single DNA sequence (Fig. 3.11a, b) or reconstructed with sequence exchange (Fig. 3.11c, d). All nanostructures exhibited significant near field enhancement (30-40) owning to their highly anisotropic geometries. Besides, the distribution of electric field hotspots in different structures were highly dependent on their aspect ratios and the tip angles. In the structure synthesized with A20 (Fig. 3.11a), the electric field concentrated at the longitudinal tips of the nanostructures. On the other hand, the structures synthesized with C20 (Fig. 3.11b) formed more hotspots at the edges/vertices between the longitudinal ends and the side facets. The drastic difference in the distribution of electric field highlighted the importance of controlling tip angles in the nanostructures. As the tip angle increased, the electric field initially concentrated at the two sharp tips of the bipyramid derived structures, then gradually diffused to the nearby edges and vertices. The field enhancement at the longitudinal tips (47.56) was slightly higher than that in the edges (37.63), but the C20 structures possessed more hotspots than A20 structures. And both the intensity of the electric field enhancement and the number of hotspots in a plasmonic substrate affect the overall magnification on Raman signal.[16] The regrowth of structures with another sequence offered opportunity to fine tune the distribution of the hotspots. Fig. 3.11c showed the electric field distribution of structures regrown with C20 from A20 intermediate structures. The hotspot still has the similar intensity as that of the structures grown with A20 alone, but the hotspots were more diffused along the entire periphery of the ending facets as a result of wider tip angles after regrowth. Similarly, the end bulging structures regrown with A20 (Fig. 3.11d) also redistributed the electric field hotspots around the entire structures as a result of increased aspect ratios and facet protrusions. The shape reconstruction offered a powerful tool to tune the distribution and

intensity of electric field hotspots. Together with the predicative relationships between the structural parameters and the wavelength of the LSPR band, the kinetic reconstruction offered tremendous opportunities to design SERS substrates for specific instrumentations and analytes. The distribution of electric field also shined light on the dependence of λ max on both the tip angles and aspect ratios. The intensity of the electric field is related with the density of the local surfaces charges.[41-42] Highly concentrated electric field at tips or edges indicated effective charge separation. It has been reported that charge separation caused by anisotropic shapes caused red shifts of LSPR in Ag nanoparticles.[43-44] The red shifts of λ max with increased tip angles (A > 74) (Fig. 3.5d) can therefore be explained by further separation of the edges and vertices where the electric field concentrated. Similarly, the blue shifts of λ max with decreased aspect ratio can be explained by the redistribution of electric field along the end facets. Wider dimension caused the opposite charges to diffuse closer to each other.

3.2.5 Mechanisms for DNA controlled structural evolution of Au-Ag nanostructures

DNA controlled structural evolution of Au-Ag nanostructures exhibited interesting two-phase-transition. In the first phase, the structures grown with both A20 and C20 went through similar process of increasing tip angles and decreasing aspect ratios. However, in the second phase, structures grown with A20 mainly decreased in aspect ratios whereas the structures grown with C20 mainly increased in tip angles. The shared shape evolution pathway for both sequences in phase one was likely to be induced by the defects in the bipyramid seed. The distinct evolution trajectories in phase two was likely due to the different interaction of DNA sequences with different facets of the evolving crystals.

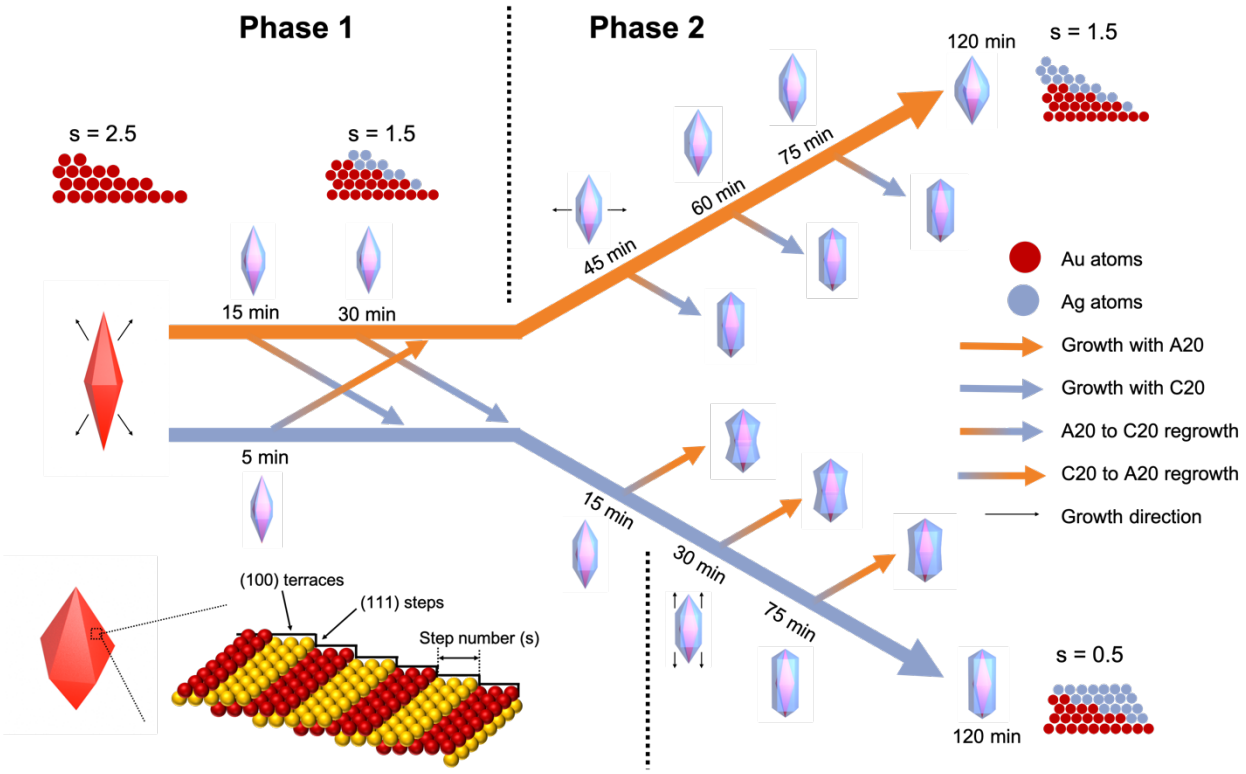


Figure 3.12: Scheme for proposed mechanisms of the evolution of Au-Ag nanostructures grown with A20 only, C20 only and regrowth.

Figure 12 shows the proposed mechanisms for the evolution of Au-Ag nanostructures. The ten side facets of the bipyramid were highly stepped surfaces composed of (100) terraces separated by (111) steps[15, 29] Those steps and terraces formed many kinks, ledges and ledge-kink sites with partially coordinated atoms. Therefore, as the crystals grew, there was a strong driving force for the atoms to preferentially deposit on those partially coordinated sites to lower the surface energy. The strength of such driving force can be qualitatively gauged from the step number, which is the dimension of the terraces measured by the number of open atoms. [29] A larger step number means the structures have more exposed {100} facet atoms, which were higher in energy compared with that on {111} facets. Hence there was a strong kinetic driving

force to minimize the step number at phase one of the growth. The microscopic step number can be calculated from the macroscopic tip angles by the following equations:

$$\theta = 2 \arctan(\tan\alpha \cos 18°) \text{ and } \tan\alpha = \frac{\sqrt{3}}{2s}.$$[29]

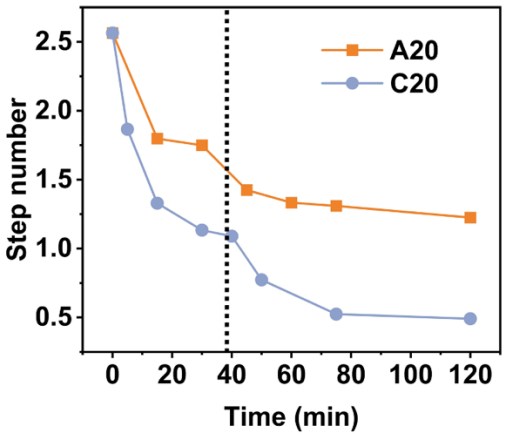


Figure. 3.13: Step number as a function of time. The dashed line indicates the separation between phase one and phase two.

As shown in Fig. 3.13, the step number for both A20 and C20 structures decreased significantly in phase one (from 2.5 to less than 1.5), which was consistent with the proposed mechanisms. Microscopically, the decrease in step number required continuous deposition of atoms onto the open terraces. Macroscopically, the crystals increased both in tip angles and aspect ratios as a result of growing the side facets. Before 40 min, such driving force was likely the main driving force for structural evolution with both DNA sequences. Once the step number was lowered to around 1.5, a more close-packed surface was formed, hence the driving force was weakened. As a result, different DNA sequences started to play roles in dictating the evolution of the structures in phase two of the growth.

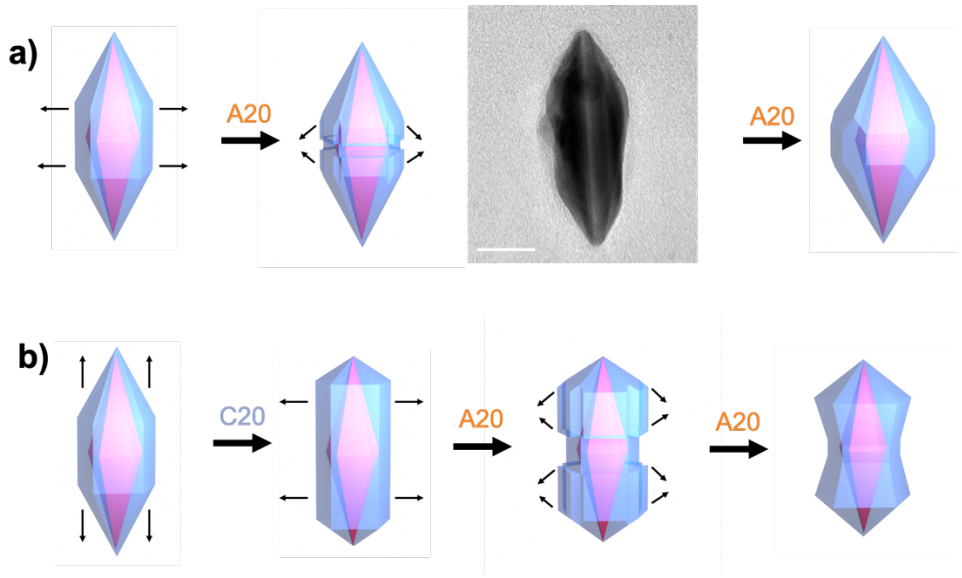


Figure 3.14: Mechanisms for structural evolution with a) A20 only and b) C20 to A20 transition. The TEM image showed the key intermediate structure. Scale bar 20 nm. Black arrows indicate the growth direction.

In phase two, A20 controlled the structures to increase in transversal dimension while keeping the same tip angle. This was likely because the atom deposition on the end facets were slowed down and the deposition was primarily on the newly formed {100} side facets. Even though the end facets were still more stepped compared with the low index facets, A20 might have stabilized the end facets more than the side facets. A20 has been found to stabilize the high index facets of Ag structures in our previous study as well.[24] The growth of the newly formed side facets were likely to have gone through the face elevation process. Fig. 3.14a showed the scheme of such process. We have also found the face-elevated intermediate structures that corroborated this hypothesis (Fig. 3.14 inset TEM image). The face-elevated intermediates were high in surface energy hence were transient. The face elevated structures were also found in the overgrowth of Ag on Au decahedra in the presence of A20,[24] indicating this was a common mechanism in the development of penta-twinned structures in the presence of A20. Elevation of

side facets created grooves and ridges along the twin edges, which became additional driving force for the crystals to grow transversally to eliminate those high energy concave sites.

On the other hand, C20 controlled structures stopped growing transversally in phase two, but kept increasing tip angles. This was likely because C20 did not preferentially stabilize the end facets as A20 did, so the deposition continue to take place on the end facets. The step number kept decreasing, until more close-packed {111} facets were formed. Even though the newly formed {100} side facets were not necessarily lower in surface energy than the end facets, the expansion towards the transversal direction was self-restricted due to the lattice strain in the penta-twinned structures.[45] C20 has also been shown to stabilize {111} facets in Ag structures,[20, 24] which corroborated the observation that the fully grown C20 structures always have tip angles that were close to the tip angle of a {111} facets enclosed decahedron (114.73 degrees).

The general rule for the regrowth process was that if the starting intermediate structures were at phase one, the regrowth process would first finish the growth in phase one, then followed the pathway for phase two of the second sequence. As a result, the regrowth produced almost identical structures as that grown with the second sequence only. Whereas if the starting structures already entered phase two, the regrowth process would directly follow the pathway of phase two determined by the second sequence. Consequently, new shapes emerged because of the combinatorial effect from the phase two of both sequences. The structures regrown with A20 to C20 transitions could be perfectly explained by this general principle. The initial growth with A20 determined the overall dimension of the crystals whereas the secondary growth with C20 determined the tip angles in the final structures. However, the structures regrown with C20 to A20 exhibited end-bulging structures that could be explained by neither longitudinal nor transversal growth. This process could be explained by the unique face elevation mechanisms for

A20 directed growth. When the face elevation mechanism was applied on a structure that have small tip angles, the grooves formed along the transversal periphery could easily be eliminated by additional atom deposition and migration. However, initial growth with C20 increased tip angles, hence enlarged the side facets. In the structures regrown with C20 to A20 transition at 15 min and 30 min, because C20 has stronger affinity towards Ag metal, [24] even after the sequence was exchanged to A20, the residual effect for C20 directed growth likely continued to increase the tip angles, hence further enlarged the side facets. As a result, the face elevation from C20 derived structures also formed larger grooves that could not be fully compensated (Fig. 3.14b). The elevated faces were later developed into the bulging belts separated by uncompensated grooves. As the sequence exchange was applied at later time points, the evolution pathway of phase two for C20 gradually dominated in the structural evolution, so the unique structural feature gradually disappeared in regrown structures with regrowth at later times.

3.3 Conclusion

In conclusion, we systematically analyzed the evolution of aspect ratios and tip angles in the growth of Au-Ag nanostructures controlled by two different DNA sequences. The optical properties such as the wavelength and the extinction of the longitudinal plasmonic peak as well as the distribution of the near electric field were found to be closely related with those two structural parameters. The co-evolution of structures and functions during the growth of the plasmonic nanostructures gave us access to a continuous spectrum of functional features that would otherwise take multiple synthesis reactions with different sets of reaction conditions. We further used the knowledge of DNA controlled evolution of the structural parameters to design new structures by exchanging DNA sequences in the growth environment. The structural parameters of the resulting structures could be predictively tuned by the timing of the exchange.

The optical properties of the resulting structures agreed both qualitatively and quantitively to the prediction based on their structural parameters.

The unique two-phase kinetic evolution pathway in DNA mediated growth of Au-Ag nanostructures provides the unique opportunity to analyze the two structural parameters both individually and collectively. It allows us to deconvolute the contributions from the two structural parameters in affecting λ max and the extinction of plasmonic peaks in different kinetic and geometric domains, which is important for identifying the most effective structural parameter in functional tuning. Moreover, the predictable combinatorial effect in the regrowth is only made possible by the distinct evolution pathway of each individual parameter in the second phase of the growth. These results demonstrate the powerful toolbox provided by programmable biomolecular capping ligands in producing novel structures in a predictable manner. The analysis of the complicated co-evolution of the structure and functional parameters provides valuable insights in the kinetic process of the nanostructure formation. With better understanding of the kinetic process, we will eventually realize the dream of predictive design of the synthetic path for functional nanostructures.

3.4 Experimental section

3.4.1 Chemicals and Materials

All single stranded DNA sequences were purchased from Integrated DNA Technologies (Coralville, IA) with standard desalting and without further purification. Gold(III) chloride trihydrate (≥99.9% trace metals basis), Cetrimonium bromide (CTAB), sodium borohydride (99.99% trace metals basis), silver acetate (AgOAc, 99.99% trace metals basis), L-ascorbic acid (≥99%), cetyltrimethylammonium chloride (CTAC) and citric acid were purchased from Sigma-Aldrich. Deionized water (18.2 MΩ) was used to dissolve all chemicals.

3.4.2 Preparation of Au Bipyramid seeds

Au bipyramid seeds were synthesized using previously published seed-mediated procedure. {Sanchez-Iglesias, 2017 #34} The seeds for Au bipyramid was synthesized by reducing $HAuCl_4$ (10 mL, 0.25 mM) with $NaBH_4$ (0.25 mL, 25 mM) in the presence of CTAC (50 mM) and citric acid (5 mM) under vigorous stirring at room temperature. The seed solution was then heated in an oil bath at 80 ºC for 90 min under gentle stirring. 200 μL of gold seeds was added to a growth solution containing CTAB (12.5 mL, 100 mM), $HAuCl_4$ (625 μL, 10 mM), $AgNO_3$ (125 μL, 10mM), HCl (250 μL, 1M) and ascorbic acid (100 μL, 100 mM) at 30 ºC. The mixture was left undisturbed at 30 °C for 4 hours.

3.4.3 DNA-Mediated Synthesis of Au-Ag Core-Shell NPs

The Au bipyramid seeds was washed by centrifugation (7k rpm, 5 min) for three times to remove as much CTAB as possible. Such practice was shown to effectively remove most of the surface ligands on the seeds in the synthesis of DNA mediated Au-Ag nanostructures in our previous work.[24] The washed bipyramid solution was diluted with DI water until the absorbance at 840 nm reached 0.7. 10 mL of the diluted seed solution were incubated with 7 μM single stranded DNA (C20, A20, T20) for 15 minutes. Then 100 μL of 10 mM ascorbic acid solution and 200 μL of 10 mM AgOAc solution were added. Stir violently for 1min, followed by gentle stir for 2 hours.

3.4.4 Kinetic reconstruction of DNA controlled Au-Ag nanostructures

1ml aliquots were taken from the growth solution of DNA-mediated synthesis of Au-Ag nanostructures at different time points. The solutions were immediately centrifuged in 1.7 ml centrifuge tubes for 1 min at 8k rpm. The supernatants were removed, and the sediment were dispersed in 1 μM solution of the new DNA sequence. Such process was repeated for three

times. In the last time, the sediments were dispersed in 20 μM solution of the new DNA sequence. The resulting solution was incubated for at least 12 hours for more complete ligand exchange. The prepared solution was used as seeds in the regrowth. 10 μL of 10 mM ascorbic acid solution and 20 μL of 10 mM AgOAc solution were added into the seed solution, followed by violent stir for 1 min, and gentle stir for 2 hours.

3.4.5 Instrumentation and Characterization

The synthesized nanostructures were analyzed using a JEOL 2100 cryo TEM operated at 200 kV or a Hitachi S4800 SEM at 10 kV and 10 μA. UV-vis spectroscopy was performed on an HP 8453 UV-Vis spectrometer.

3.5 Reference

1. Park, J.-H.; Ndao, A.; Cai, W.; Hsu, L.; Kodigala, A.; Lepetit, T.; Lo, Y.-H.; Kanté, B., Symmetry-breaking-induced plasmonic exceptional points and nanoscale sensing. *Nature Physics* **2020,** *16* (4), 462-468.

2. Wang, H.; Rao, H.; Luo, M.; Xue, X.; Xue, Z.; Lu, X., Noble metal nanoparticles growth-based colorimetric strategies: From monocolorimetric to multicolorimetric sensors. *Coordination Chemistry Reviews* **2019,** *398*, 113003.

3. Li, S.; Miao, P.; Zhang, Y.; Wu, J.; Zhang, B.; Du, Y.; Han, X.; Sun, J.; Xu, P., Recent Advances in Plasmonic Nanostructures for Enhanced Photocatalysis and Electrocatalysis. *Advanced Materials* **2021,** *33* (6), 2000086.

4. Kim, J.; Yoo, S.; Kim, J.-M.; Choi, S.; Kim, J.; Park, S.-J.; Park, D.; Nam, J.-M.; Park, S., Synthesis and Single-Particle Surface-Enhanced Raman Scattering Study of Plasmonic Tripod Nanoframes with Y-Shaped Hot-Zones. *Nano Letters* **2020,** *20* (6), 4362-4369.

5. Kim, M.; Lee, J. H.; Nam, J. M., Plasmonic photothermal nanoparticles for biomedical applications. *Advanced Science* **2019,** *6* (17), 1900471.

6. Wang, W.; Yu, P.; Zhong, Z.; Tong, X.; Liu, T.; Li, Y.; Ashalley, E.; Chen, H.; Wu, J.; Wang, Z., Size-dependent longitudinal plasmon resonance wavelength and extraordinary scattering properties of Au nanobipyramids. *Nanotechnology* **2018,** *29* (35), 355402.

7. Qi, Y.; Xing, T.-y.; Zhao, J.; Weng, G.-j.; Li, J.-j.; Zhu, J.; Zhao, J.-w., Tuning the surface enhanced Raman scattering performance of anisotropic Au core−Ag shell hetero-nanostructure: The effect of core geometry. *Journal of Alloys and Compounds* **2019,** *776*, 934-947.

8. Xia, Y.; Xia, X.; Peng, H.-C., Shape-Controlled Synthesis of Colloidal Metal Nanocrystals: Thermodynamic versus Kinetic Products. *Journal of the American Chemical Society* **2015,** *137* (25), 7947-7966.

9. Walsh, M. J.; Tong, W.; Katz-Boon, H.; Mulvaney, P.; Etheridge, J.; Funston, A. M., A Mechanism for Symmetry Breaking and Shape Control in Single-Crystal Gold Nanorods. *Accounts of Chemical Research* **2017,** *50* (12), 2925-2935.

10. Zhang, P.; Wyman, I.; Hu, J.; Lin, S.; Zhong, Z.; Tu, Y.; Huang, Z.; Wei, Y., Silver nanowires: Synthesis technologies, growth mechanism and multifunctional applications. *Materials Science and Engineering: B* **2017,** *223*, 1-23.

11. Park, K.; Drummy, L. F.; Wadams, R. C.; Koerner, H.; Nepal, D.; Fabris, L.; Vaia, R. A., Growth Mechanism of Gold Nanorods. *Chemistry of Materials* **2013,** *25* (4), 555-563.

12. Chen, H.; Shao, L.; Li, Q.; Wang, J., Gold nanorods and their plasmonic properties. *Chemical Society Reviews* **2013,** *42* (7), 2679-2724.

13. Zhang, L.; Sha, X.; Fan, Q.; Han, L.; Yin, Y.; Gao, C., Gold nanoshurikens with uniform sharp tips for chemical sensing by the localized surface plasmon resonance. *Nanoscale* **2017,** *9* (43), 17037-17043.

14. Ding, S.; Yang, D.; Liu, X.; Nan, F.; Cheng, Z.; Im, S.-J.; Zhou, L.; Wang, J.; Wang, Q., Asymmetric growth of Au-core/Ag-shell nanorods with a strong octupolar plasmon resonance and an efficient second-harmonic generation. *Nano Research* **2018,** *11* (2), 686-695.

15. Chow, T. H.; Li, N.; Bai, X.; Zhuo, X.; Shao, L.; Wang, J., Gold Nanobipyramids: An Emerging and Versatile Type of Plasmonic Nanoparticles. *Accounts of Chemical Research* **2019,** *52* (8), 2136-2146.

16. Montaño-Priede, J. L.; Pal, U., Estimating Near Electric Field of Polyhedral Gold Nanoparticles for Plasmon-Enhanced Spectroscopies. *The Journal of Physical Chemistry C* **2019,** *123* (18), 11833-11839.

17. Ortiz, N.; Skrabalak, S. E., On the Dual Roles of Ligands in the Synthesis of Colloidal Metal Nanostructures. *Langmuir* **2014,** *30* (23), 6649-6659.

18. Zeng, J.; Zheng, Y.; Rycenga, M.; Tao, J.; Li, Z.-Y.; Zhang, Q.; Zhu, Y.; Xia, Y., Controlling the Shapes of Silver Nanocrystals with Different Capping Agents. *Journal of the American Chemical Society* **2010,** *132* (25), 8552-8553.

19. Wang, Z.; Zhang, J.; Ekman, J. M.; Kenis, P. J. A.; Lu, Y., DNA-Mediated Control of Metal Nanoparticle Shape: One-Pot Synthesis and Cellular Uptake of Highly Stable and Functional Gold Nanoflowers. *Nano Lett.* **2010,** *10* (5), 1886-1891.

20. Wu, J.; Tan, L. H.; Hwang, K.; Xing, H.; Wu, P.; Li, W.; Lu, Y., DNA Sequence-Dependent Morphological Evolution of Silver Nanoparticles and Their Optical and Hybridization Properties. *JACS* **2014,** *136* (43), 15195-15202.

21. Tan, L. H.; Yue, Y.; Satyavolu, N. S. R.; Ali, A. S.; Wang, Z.; Wu, Y.; Lu, Y., Mechanistic Insight into DNA-Guided Control of Nanoparticle Morphologies. *JACS* **2015,** *137* (45), 14456-14464.

22. Song, T.; Tang, L.; Tan Li, H.; Wang, X.; Satyavolu Nitya Sai, R.; Xing, H.; Wang, Z.; Li, J.; Liang, H.; Lu, Y., DNA‐Encoded Tuning of Geometric and Plasmonic Properties of Nanoparticles Growing from Gold Nanorod Seeds. *Angew. Chem. Int. Ed.* **2015,** *54* (28), 8114-8118.

23. Satyavolu, N. S. R.; Tan, L. H.; Lu, Y., DNA-Mediated Morphological Control of Pd–Au Bimetallic Nanoparticles. *JACS* **2016,** *138* (50), 16542-16548.

24. Wang, Y.; Counihan, M. J.; Lin, J. W.; Rodríguez-López, J.; Yang, H.; Lu, Y., Quantitative Analysis of DNA-Mediated Formation of Metal Nanocrystals. *Journal of the American Chemical Society* **2020,** *142* (48), 20368-20379.

25. Wang, Y.; Reddy Satyavolu, N. S.; Lu, Y., Sequence-specific control of inorganic nanomaterials morphologies by biomolecules. *Current Opinion in Colloid & Interface Science* **2018,** *38*, 158-169.

26. Zhu, X.; Zhuo, X.; Li, Q.; Yang, Z.; Wang, J., Gold Nanobipyramid-Supported Silver Nanostructures with Narrow Plasmon Linewidths and Improved Chemical Stability. *Advanced Functional Materials* **2016,** *26* (3), 341-352.

27. Li, X.; Lin, X.; Lin, S.; Sun, X.; Gao, D.; Liu, B.; Zhao, H.; Zhang, J.; Cong, S.; Wang, L., Au Nanospheres@Ag Nanorods for Wide Linear Range Colorimetric Determination of Hypochlorite. *ACS Applied Nano Materials* **2019,** *2* (5), 3161-3168.

28. Zhu, X.; Xu, J.; Zhang, H.; Cui, X.; Guo, Y.; Cheng, S.; Kan, C.; Wang, J., Gold nanobipyramid-embedded ultrathin metal nanoframes for in situ monitoring catalytic reactions. *Chemical Science* **2020,** *11* (12), 3198-3207.

29. Liu, M.; Guyot-Sionnest, P., Mechanism of Silver(I)-Assisted Growth of Gold Nanorods and Bipyramids. *The Journal of Physical Chemistry B* **2005,** *109* (47), 22192-22200.

30. Lee, J.-H.; Gibson, K. J.; Chen, G.; Weizmann, Y., Bipyramid-templated synthesis of monodisperse anisotropic gold nanocrystals. *Nature Communications* **2015,** *6*, 7571.

31. Sánchez-Iglesias, A.; Winckelmans, N.; Altantzis, T.; Bals, S.; Grzelczak, M.; Liz-Marzán, L. M., High-Yield Seeded Growth of Monodisperse Pentatwinned Gold Nanoparticles through Thermally Induced Seed Twinning. *Journal of the American Chemical Society* **2017,** *139* (1), 107-110.

32. Reyes-Gasga, J.; Elechiguerra, J. L.; Liu, C.; Camacho-Bragado, A.; Montejano-Carrizales, J. M.; Jose Yacaman, M., On the structure of nanorods and nanowires with pentagonal cross-sections. *Journal of Crystal Growth* **2006,** *286* (1), 162-172.

33. Johnson, C. J.; Dujardin, E.; Davis, S. A.; Murphy, C. J.; Mann, S., Growth and form of gold nanorods prepared by seed-mediated, surfactant-directed synthesis. *Journal of Materials Chemistry* **2002,** *12* (6), 1765-1770.

34. Huang, X.; Neretina, S.; El-Sayed, M. A., Gold Nanorods: From Synthesis and Properties to Biological and Biomedical Applications. *Advanced Materials* **2009,** *21* (48), 4880-4910.

35. Gans, R. v., Form of ultramicroscopic particles of silver. *Ann. Phys* **1915,** *47* (10), 270-284.

36. Wiley, B. J.; Chen, Y.; McLellan, J. M.; Xiong, Y.; Li, Z.-Y.; Ginger, D.; Xia, Y., Synthesis and Optical Properties of Silver Nanobars and Nanorice. *Nano Letters* **2007,** *7* (4), 1032-1036.

37. Jiang, R.; Chen, H.; Shao, L.; Li, Q.; Wang, J., Unraveling the Evolution and Nature of the Plasmons in (Au Core)–(Ag Shell) Nanorods. *Advanced Materials* **2012,** *24* (35), OP200-OP207.

38. Ming, T.; Zhao, L.; Yang, Z.; Chen, H.; Sun, L.; Wang, J.; Yan, C., Strong Polarization Dependence of Plasmon-Enhanced Fluorescence on Single Gold Nanorods. *Nano Letters* **2009,** *9* (11), 3896-3903.

39. Li, Z.; Ye, Z.; Han, L.; Fan, Q.; Wu, C.; Ding, D.; Xin, H. L.; Myung, N. V.; Yin, Y., Polarization-Modulated Multidirectional Photothermal Actuators. *Advanced Materials* **2021,** *33* (3), 2006367.

40. Kneipp, K.; Moskovits, M.; Kneipp, H., *Surface-enhanced Raman scattering: physics and applications*. Springer Science & Business Media: 2006; Vol. 103.

41. Zhang, X.-Y.; Han, D.; Ma, N.; Gao, R.; Zhu, A.; Guo, S.; Zhang, Y.; Wang, Y.; Yang, J.; Chen, L., Carrier Density-Dependent Localized Surface Plasmon Resonance and Charge Transfer Observed by Controllable Semiconductor Content. *The Journal of Physical Chemistry Letters* **2018,** *9* (20), 6047-6051.

42. Li, K.; Liu, A.; Wei, D.; Yu, K.; Sun, X.; Yan, S.; Huang, Y., Electromagnetic Field Redistribution in Metal Nanoparticle on Graphene. *Nanoscale Research Letters* **2018,** *13* (1), 124.

43. Cobley, C. M.; Skrabalak, S. E.; Campbell, D. J.; Xia, Y., Shape-Controlled Synthesis of Silver Nanoparticles for Plasmonic and Sensing Applications. *Plasmonics* **2009,** *4* (2), 171-179.

44. Kottmann, J. P.; Martin, O. J. F.; Smith, D. R.; Schultz, S., Plasmon resonances of silver nanowires with a nonregular cross section. *Physical Review B* **2001,** *64* (23), 235402.

45. Lofton, C.; Sigmund, W., Mechanisms Controlling Crystal Habits of Gold and Silver Colloids. *Advanced Functional Materials* **2005,** *15* (7), 1197-1208.

CHAPTER 4: QUANTITATIVE DESIGN OF METAL NANOCRYSTAL SYNTHESIS USING ELECTROCHEMISTRY

4.1 Introduction

To fully digitalize the reaction of the formation of metal nanocrystals, it is essential to establish the quantitative relationships between the reactants, the kinetics, and the resulting nanostructures. The key parameters for the quantitative description are the energy terms of the reaction, such as free energy and activation energy. Typically, those energy terms are primarily obtained by simulation because they are very difficult to be measured experimentally.[1] However, those energy terms can be easily measured in an electrochemical cell.[2] The redox reaction in the synthesis of metal nanocrystals can be understood in the concept of a battery. The cathodic reaction is the reduction of metal ions and the anodic reaction is the oxidation of reducing agents. The free energy, activation energy and reaction kinetics in the synthesis reaction can be converted to the potential, overpotential and current output of the battery. In this way, all energetic quantities became measurable. We can establish quantitative relationships between reactants and kinetics, hence the resulting nanocrystals, similar to the voltage-current relationships in a battery. This conceptual model will enable scientists to make informed choices of chemical reactants in a synthetic protocol based on the desired nanostructured outcome, which will significantly reduce trial and error. I demonstrated this idea in a model system of synthesizing Palladium nanocrystals. By modulating redox potentials of the starting chemical reactants, the reaction kinetics and the size of the resulting Palladium nanostructures were tunable. This study established the quantitative relationship between the starting reactants, the

kinetics and the structural parameters in the synthesis of metal nanocrystals, which signifies a major step towards predictable synthesis of nanomaterials.

4.2 Results and discussion

4.2.1 Introduction of ultramicroelectrode

Ultramicroelectrode was employed in monitoring the reaction kinetics as well as the reduction potential of the metal precursors in the following section. Herein, I give a brief introduction of ultramicroelectrode before introducing the specific experiments that were performed.

Ultramicroelectrode (UME) is an electrode with at least one dimension (such as the radius of the disk) smaller than 25 μm (Figure 4.1).[2] UME as small as several nanometers can also be made. UME can adopt the shape of a disk, a sphere, a band or a cylinder. For the following discussion, we will focus on the disk-shaped UME.

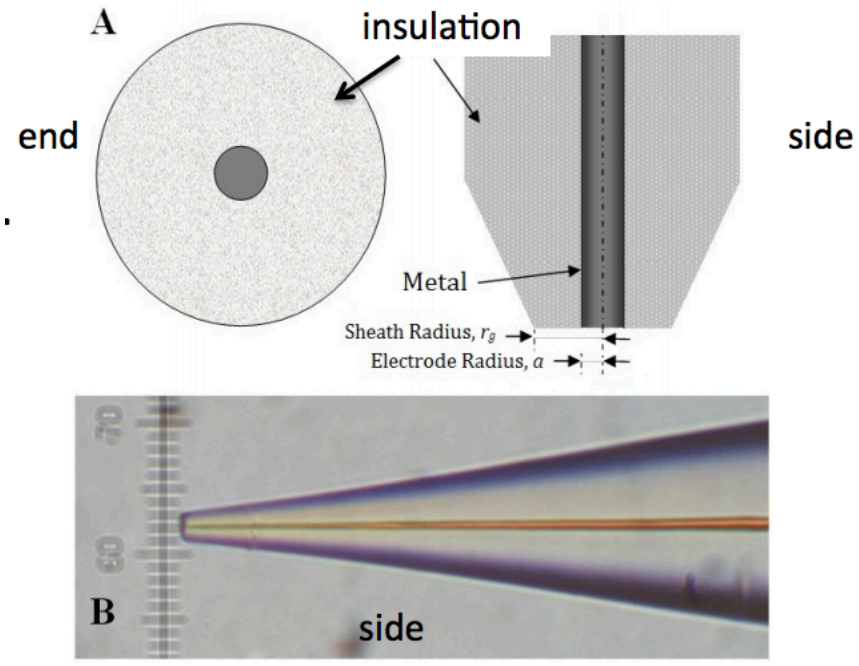


Figure 4.1: (A) Schematics of a tip ultramicroelectrode. The exposed metal is the active part of the electrode. (B) Optical micrograph of a tip. The platinum wire (orange) is sealed inside a glass sheath. (Adapted from https://knowledge.electrochem.org/encycl/art-m04-microscopy.htm)

Such small size gives UME unique functional features. The behavior of the electrode-solution interface is analogous to that of a capacitor. When a potential is applied on an electrode, counter ions in the solution are attracted to the electrode surface to balance the electrode charge, hence forming the electric double layer. Capacitive current is the current caused by charging the electric double layer. The capacitive current is a non-faradaic current. After a certain potential is set at the electrode, meaningful measurement can only be made after the double layer is sufficiently charged. In a cyclic voltammetry (CV) measurement, potential is constantly changing so the capacitive current always exists. As scan rate (v) increases, the Faradaic current might eventually be completely masked by the capacitive current. Besides, when the concentration of the reactive redox species is low ($<10^{-5}$ M), the Faradaic current will also be significantly smaller compared with the capacitive current, hence the signal of the redox active species cannot be adequately separated. However, the small size of UME significantly reduced the couple layer capacitance and capacitive current during a potential sweep. For a 4 μm diameter UME, the double layer should be 99% charged within 3 μs. Therefore, UMEs has much better sensitivity to a Faradaic process compared with standard electrodes. The small size of UME not only changes its double layer capacitance but also modulates the diffusion layer of the electrode-solution interface. The region of solution near the electrode surface over which the concentration of the electroactive species is different from that in bulk solution is the diffusion layer. Within the diffusion layer, the current is limited by the mass transport of the electroactive species from the solution to the electrode surface. The thickness of the diffusion layer changes as a function of time. It takes about 360 h for a 1 cm disk electrode to reach steady state current.[3] Such dynamic process complicates the analysis for charge transfer process. The kinetics of the actual reaction could be unattainable because it is masked by the diffusion process. There are

multiple methods to minimize the complications from the diffusion process. The most commonly adopted method is to use a rotating disk electrode (RDE). RDE introduces rapid convectional mass transport to increase the ion flux near the electrode surface, which reduces the thickness of the diffusion layer. However, significant convection is introduced into the reaction system, which might change the reaction kinetics. However, if the size of the electrode is reduced to micron size, the shape of the diffusion layer is transformed from a linear diffusion profile to a hemispherical profile (Fig. 4.2). As a result, UMEs have much larger diffusion coefficient compared with that of a standard electrode. Mass transport coefficient of a spherical electrode with a diameter of 10 μm corresponds to a speed of 10000 rpm RDE. Whereas this is the maximum speed for rotating electrodes, the dimensions of UME can be made smaller. Besides, the limitation for mass transport is lifted with no convection complication introduced into the system. The diffusion layer only grows to a thickness of 100 μm or less for a UME. It only takes approximately 1.3 s for a 10 μ m disk electrode to reach a stationary state. [3] The easy access to the steady state current allows us to probe the reaction kinetics without the complication of mass transport. Besides, because the steady state current of the UMEs is proportional to the concentration of the electroactive species, monitoring steady state current of a system provides us with a way to monitor the progress of a reaction.

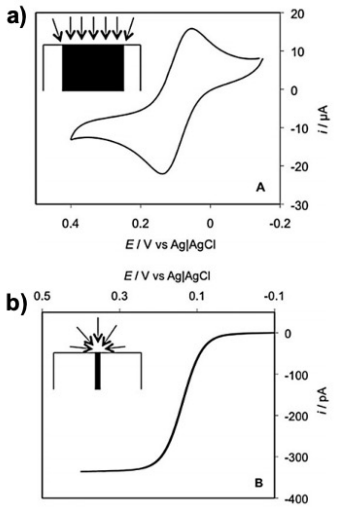


Figure 4.2: Typical cyclic voltammograms obtained at a) a 2 mm diameter Pt disk and b) a 1.3 mm diameter Pt disk UME in 1 mM ferrocenemethanol dissolved in 0.1 M KCl. The insets in each figure show the predominant mode of mass transfer to the electrode surface. a) Semi-infinite linear diffusion to a macroelectrode. b) Hemispherical diffusion to a UME. Adapted with permission from reference [4], copyright 2010, Royal Society of Chemistry.

Beisdes, UME can also minimize the Ohmic drop. Ohmic drop refers to the extra energy needed to get ions moving in solution. The extra potential loss (E_{ohmic} = IR) distorts the cyclic voltammogram and masks the important information. The conventional solution to mitigate this problem is to add supporting electrolyte to increase the conductivity of the solution (decrease R). However, supporting electrolyte might affect the electrostatic interactions between nanoparticles hence change the resulting structures. A UME can reduce the Ohmic drop because it has smaller current compared with standard electrode (decrease I), which allows it to perform measurements is solution with high resistance. This is important for us to construct kinetic systems that is close to the native nanoparticle synthesis system.

4.2.2 Choosing reducing agents

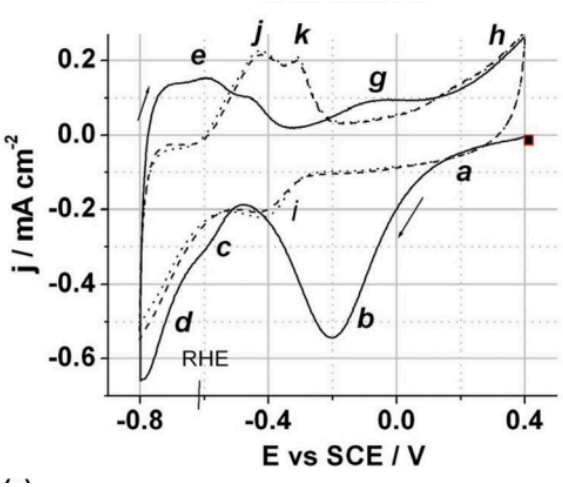


Figure 4.3: Cyclic voltammograms of sodium citrate. Adapted with permission from reference [5], copy right 2011, The Electrochemical Society.

To predictably tune the anodic potential of the hypothetical synthetic cell, we need to choose a series of reducing agents that have tunable reduction potential. However, it would be a significant task if we were to choose from conventional reducing agents. The conventional reduction agents such as citrate, ascorbic acid and sodium borohydride usually adopt multiproton and multielectron reduction pathway. As shown in Fig 4.3, The reduction potential of sodium citrate was not well defined, and likely to be pH dependent. The forward and reverse peaks were not symmetrical, and the peak positions were also different for different scans, which indicates the reaction kinetics are controlled by complicated reduction mechanisms. The complicated reduction mechanisms and a lack of definitive reduction potentials of conventional reducing agents made it difficult to choose appropriate reducing agents solely based on their reduction potentials. On the other hand, redox mediators are a series of molecules, polymers, ions, or compounds that can be reversibly oxidized and reduced upon electrochemical cycling. The redox mediators usually have high reversibility, fast kinetics, and negligible side reactions.[6] A variety

of redox mediators with different redox potentials have been discovered or synthesized. Fig.4.4 shows cyclic voltammograms of a series of ferrocene derivatives with different functional groups. The redox potentials of those ferrocene derivatives could be modulated by switching between electron-withdrawing or electro-donating functional groups. The shape of their cyclic voltammograms also demonstrate the perfect reversibility in the electron transfer process. Therefore, we used redox mediators as tunable and predictable reducing agents to construct our model system for nanoparticle synthesis.

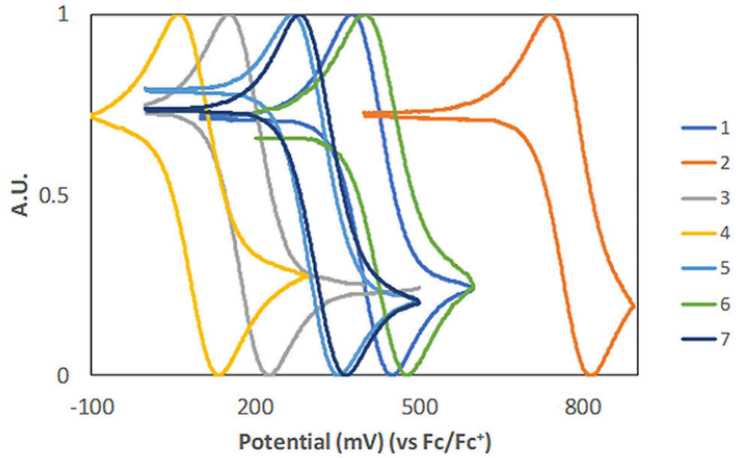


Figure 4.4: Cyclic voltammograms of ferrocene derivatives. Adapted with permission from reference [7], copy right 2019, John Wiley and Sons.

The model system was to synthesize Pd nanoparticles in aqueous solution. In order to select appropriate redox mediators for such system, we screened 17 redox mediators. Table 4.1 lists the name of those redox mediators. We have several criteria for the screening. Firstly, because the synthesis would be performed in aqueous solution, the redox mediators should be soluble in water for at least 1mM. Secondly, the redox mediators should remain stable with multiple rounds of CV scan. Distortion of cyclic voltammograms or disappearance of the peaks indicated the mediators were either decomposed or formed some unstable intermediators. All

those processes could potentially interfere with the nanoparticle formation reaction. Thirdly, the redox mediators should strictly perform outer sphere electron transfer in the presence of Pd^{2+}. Because only in outer sphere electron transfer, the reduction kinetics can be predicted by the thermodynamic equilibrium potentials of both the precursor and the redox mediators. However, if the redox mediators coordinate with Pd^{2+}, the reduction kinetics will be more difficult to predict. We evaluate this criterion by performing CV test of redox mediators both with and without Pd^{2+}. If the resulting voltammograms were consistent, the redox mediator does not interact with Pd^{2+}. Besides those criteria, we also recorded the redox potentials of each redox mediators. We would like to pick redox mediators with widely spread redox potentials so that we can see the effect of the reaction kinetics as a function of cell potentials. Finally, we also recorded the oxidation state of the redox mediators in the air, as this will tell us whether we should pretreat the mediators to reduce them to their reduced state before starting the experiments. As shown in Table 4.1, most of the redox mediators that were screened satisfy the solubility criterion except for 1,2-naphthoquinone, aminoferrocene and 5-hydroxy-1,4-naphthoquinone. Prussianblue, aminoferrocene, methyl-p-tolyl, 4,4-dipyridyl were not stable with multiple rounds of CV scan. 2 6-Dichlorophenolindopheno and 5-hydroxy-1,4-naphthoquinone interacted with Pd^{2+} so they couldn't be used. After the initial screening, the remaining candidates were N,N,N,N-tetramethyl-p-phenylenediamine (TMPD), ferrocene methanol (FcMeOH), hexaammineruthenium(III) chloride (Ruhex), 2-hydroxy-1,4 napthoquinone, trimethylhydroquinone, 2-methyl-1,4-naphthoquinone, 2 3 5 6-tetramethyl-1 4-phenylenediamine, anthraquinone-2-sulfonic acid sodium salt hydrate, methylviologen, tetramethyl-1 4-phenylenediamine and 5-hydroxy-1,4-naphthoquinone. Among those candidates, we chose TMPD, FeMeOH, Ruhex and methyl viologen for our initial investigation. Other than

FeMeOH, all other candidates been to pretreated to their reduced state before starting the reaction.

Table 4.1: Properties of redox mediators.

Red mediator	Solubility	Stability	Interaction with Pd^{2+}	Redox potential (V) vs Ag/AgCl	air state
TMPD	At least 1mM	Good	No	0.46, 0.03	0.03V oxidized
FcMeOH	At least 3mM	Good	No	0.21	Reduced
2 6-dichlorophenolindopheno	Probably more than 1mM	Good	Yes	-0.12	Mostly oxidized
Hexaammineruthenium(III) chloride	More than 3mM	Good	No	-0.15	Mostly oxidized
2-hydroxy-1,4 napthoquinone	At least 1mM	Good	No	-0.2735	Partially oxidized
Trimethylhydroquinone	At least 1mM	Good	No	-0.3	Partially oxidized
2-methyl-1,4-naphthoquinone	At least 1mM	Good	No	-0.38	Oxidized
2 3 5 6-tetramethyl-1 4-phenylenediamine	At least 1mM	Good	No	-0.3915	Oxidized
Anthraquinone-2-sulfonic acid sodium salt hydrate	At least 1mM	Good	No	-0.5653	Oxidized
Methyl viologen	At least 1mM	Good	No	-0.675	Oxidized
Tetramethyl-1 4-phenylenediamine	At least 1mM	Good	No	-0.35	Oxidized
1,2-Naphthoquinone	Very little	-	-	-	-
Prussianblue	At least 1mM	Bad	-	-	-
Aminoferrocene	Less than 1mM	Bad	-	-0.1	-
5-hydroxy-1,4-naphthoquinone	Less than 1mM	Good	Yes	-0.25	-
Methyl-p-tolyl	At least 1mM	Bad	-	-	-
4,4-dipyridyl	At least 1mM	Bad	-	-	-

4.2.3 Measuring reduction potentials and overpotentials of metal precursors

Na_2PdCl_4 is a commonly used precursor for the synthesis of Palladium nanocrystals.[8-9] To determine its reduction potential, we obtained its cyclic voltammograms using both the UME and the standard electrode (Fig. 4.5a, b). We then used digiElch simulation to extract the thermodynamic and kinetic parameters from the cyclic voltammograms.

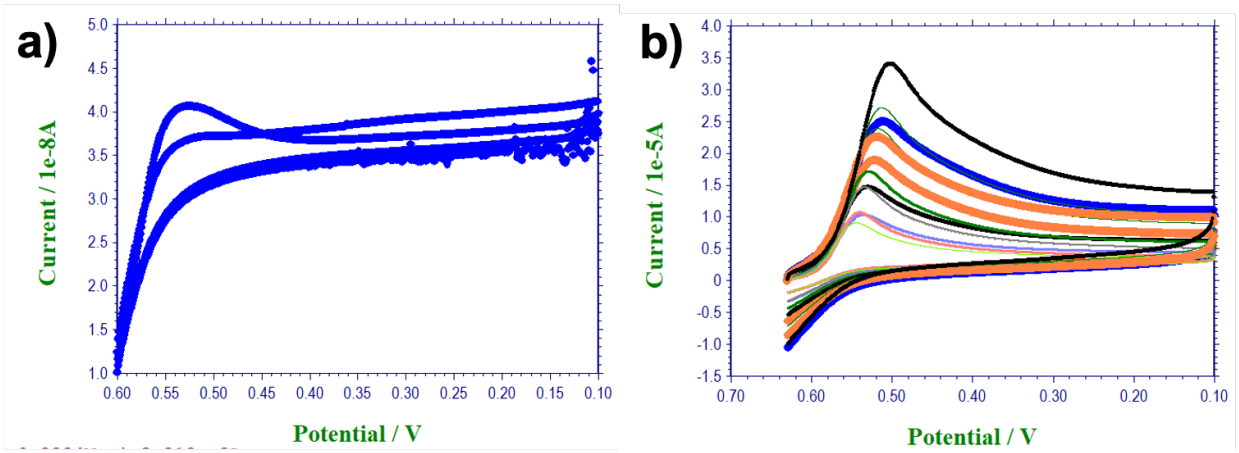


Figure 4.5: Cyclic voltammograms of 2 mM Na_2PdCl_4 solution using a) a Pt UME with a radius of 12.5 μm (scan rate 20 mV/s) , and b) a Au macro electrode (scan rate 10 -100 mV/s). Reference Ag/AgCl electrode.

There are two possible mechanisms by which Na_2PdCl_4 can be reduced. The first possibility is a chemical reaction precedes an electrochemical reaction (CE).

C: $PdCl_4^{2-} \overset{k_f}{\leftrightarrow} Pd^{2+} + 4Cl^-$ $K_{eq} = \frac{k_f}{k_b}$

E: $Pd^{2+} + 2e \overset{k}{\leftrightarrow} Pd$ $E^0 = 0.721$V

In a CE mechanism, the $PdCl_4^{2-}$ ion first dissociates into Pd^{2+} and Cl^-, then Pd^{2+} is used as the direct precursor to generate Pd atoms. The shape and position of the cyclic voltammogram is determined by the equilibrium constant and rate constant of the preceding dissociation reaction, as well as the rate constant and the redox potential of the Pd^{2+} reduction reaction. We fitted the cyclic voltammograms obtained by both the UME and the macroelectrode with a scan rate of 20 mV/s. The fitting using digiElch simulation gave $K_{eq} = 1x10^{-5}$, $k_f = 2x10^4$ cm/s and $k = 1x10^4$ cm/s. The large k_f and k values indicates that both the preceding chemical reaction and the electrochemical reaction are electrochemically reversible. We used the obtained parameters to simulation the cyclic voltammograms on a macroelectrode with different scan rate. As shown in

Fig. 4.6a, the reduction wave of the cyclic voltammograms reached a plateau, and the peak position (E_p) was independent of the scan rate. This indicates the cyclic voltammogram is governed by the rate at which Pd^{2+} is supplied by the preceding chemical reaction, instead of by diffusion. However, in the experimental data (Fig. 4.5b), the cyclic voltammograms with all scan rates clearly exhibited diffusion limited behavior. There is a negative shift of E_p at higher scan rate, which indicates that it is not a perfectly reversible reaction (k and k_f should not be as large). Therefore, we can conclude that the reduction of $PdCl_4^{2-}$ did not adopt CE mechanism.

The remaining possible mechanism is that the $PdCl_4^{2-}$ is reduced via a one-step electrochemical reaction (E). The reduction simultaneously generates Pd atoms and Cl^- ions.

E : $PdCl_4^{2-} + 2e \overset{k}{\leftrightarrow} Pd + 4Cl^-$ $E^0 = 0.58V$

The simulation of E mechanism gave a k of 0.003 cm/s, which indicates the reaction is quasi-reversible. We used the k value to simulate cyclic voltammograms on a macro electrode and different scan rate (Fig. b). The simulated cyclic voltammograms exhibited diffusion-controlled curve at all scan rate, and has a negative shift of E_p as the scan rate increased, which was consistent with the experimental observation. This result indicates the dissociation of ligand and electron transfer is likely to be concerted. Such simulation can be performed on different precursors with different ligands, so the redox potential as well as the activation energy of the precursors could be obtained.

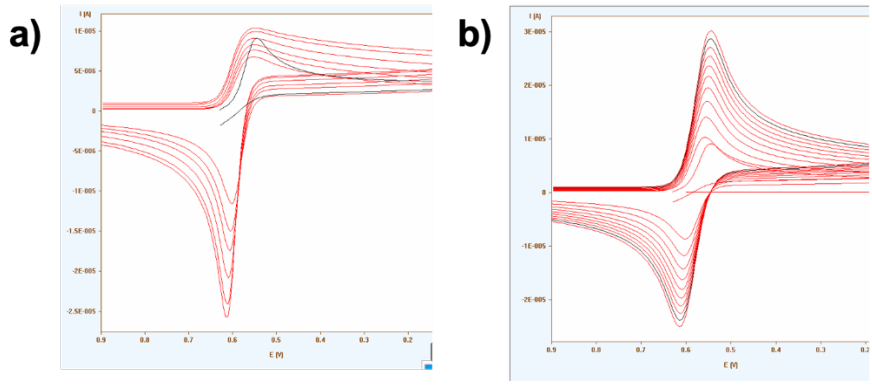


Figure 4.6: Cyclic voltammograms of 2mM Na_2PdCl_4 solution simulated by DigiElch software at different scan rate assuming a) CE mechanism and b) E mechanism.

4.2.4 Monitoring reduction kinetics

It is important to monitor the reaction kinetics of nanoparticle formation while the reaction is going on, without introducing too much disturbance. In Chapter two, we used spectroscopy methods to measure the concentration of metal precursors to monitor reaction kinetics. However, the spectroscopy-based method requires manual sampling at different time points, which would be too labor intensive if we were to screen many reaction conditions. Therefore, we need a method to monitor the reaction kinetics *in situ*, with high throughput and minimal perturbances to the system. The unique feature of the UME made it possible. The steady current (i_{ss}) of a UME can be expressed as $i_{ss} = 4\pi nFDC_{red}r_0$. Therefore, if a constant potential is held at the steady state region of a cyclic voltammogram, we can know the instant concentration of the electroactive species (C_{red}). Fig. 4.7 uses the cyclic voltammograms of FeMeOH as an example to illustrate this idea. The steady state current was shifted to more positive values as the FeMeOH was oxidized. Therefore, if a constant potential is held at 0.4V, and we monitor the current change as a function of time, we can monitor the concentration of remaining FeMeOH (reduced) in real time. The UME is a non-invasive kientic probe because it

only requires minimal current (nA) that almost has no effect on the overall concentration of the reduced and oxidized species.

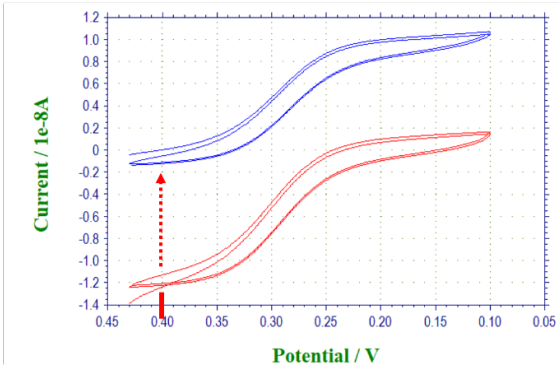


Figure 4.7: Cyclic voltammogram of FeMeOH in reduced (red) and oxidized (blue) form. The red mark indicates the potential for the current-time measurement. The red arrow indicates the trend for current change as the reaction progresses.

We used the UME to monitor the reaction of Palladium bromide ($PdBr_2^{2-}$) reacting with FeMeOH. As shown in Fig. 4.8a, we performed CV scan for both $PdBr_2^{2-}$ and FeMeOH to determine their redox potentials and starting concentrations. Then we started a current-time (i-t) measurement of FeMeOH, then added the metal precursor into the FeMeOH to start the reaction. As shown in Fig. 4.8b, the current instantly decreased in absolute value by more than ten-fold, indicating the reaction started. The i-t curve could later be converted to the concentration-time plot for direct visualization of the reaction kinetics. Once the reaction was finished (the current stopped changing), we performed another CV scan to probe the ending concentration of the redox mediator. In Fig. 4.8c, FeMeOH was almost completely oxidized after the reaction (Fig.4.8 c, blue). 5mM PVP was added in the reaction solution to provide colloidal stability of the particles. Such process was repeated for all the reaction conditions that were tested.

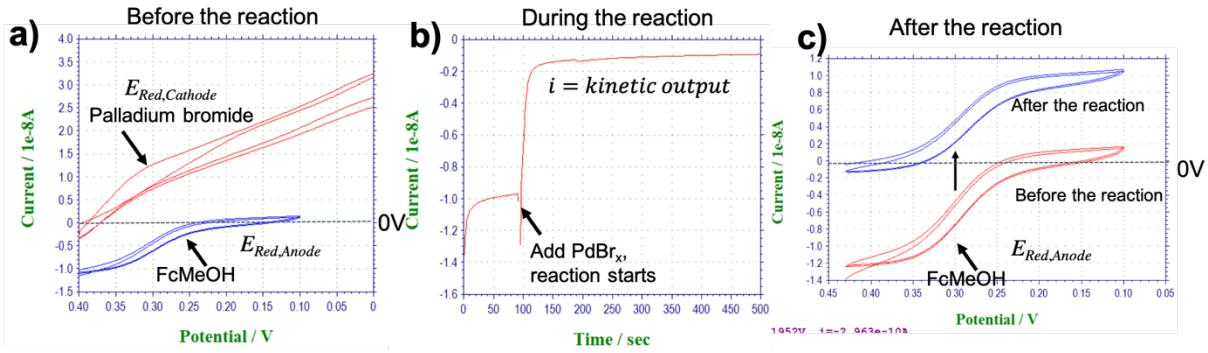


Figure 4.8: a) Respective cyclic voltammograms of Palladium bromide and FcMeOH before mixing them. b) i-t curve of FeMeOH during the reaction. c) Comparison of cyclic voltammograms of FeMeOH before and after the reaction.

4.2.5 Effect of different concentration of ligand

Ligands play important roles in controlling the nanocrystal synthesis reaction. It has been reported that ligands could stabilize the metal precursors, hence modulate their reduction kinetics.[10-12] In the concept of an electrochemical cell, if ligands change the free energy of the precursor, the redox potential of the cell should also be changed. As a result, the current output of the cell will also be changed accordingly. One important matrix in designing a protocol for nanoparticle synthesis is to choose an appropriate concentration of ligands. Conventionally, such parameter is chosen by iterative screening of synthetic conditions. If we can establish the relationship between the driving force (potential) and the kinetic output (current) of the hypothetical cell, we can quantitatively predict the relationship between the ligand concentration and the kinetics of nanoparticle synthesis reaction. Br^- is a commonly used ligand in Palladium nanoparticle synthesis. It has been found that increasing Br^- concentration resulted in slower reaction kinetics and larger particles.[13] It has also known that Br^- coordinates with Pd^{2+} and forms square planer complexes.[14] We used the Br^- modulated reduction of Na_2PdCl_4 as a model

system to study the relationship between the ligand concentration, the kinetics and the structures of nanocrystals.

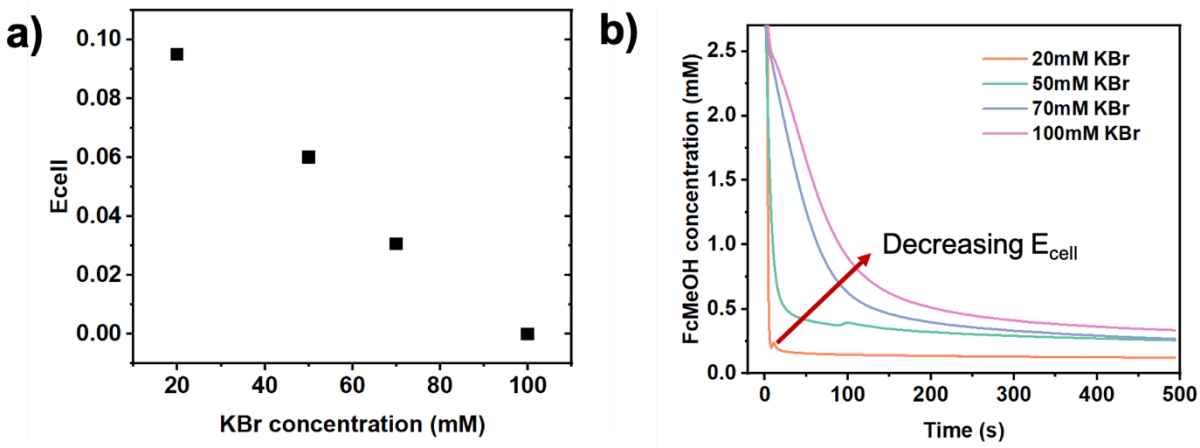


Figure 4.9: a) Potential of the hypothetical cell as a function of KBr concentration. b) FcMeOH concentration as a function of time. Different curves represent different KBr concentration.

Fig. 4.9a shows the relationship between the potential of the cell and the concentration of the Br^- ion. The potential of the cell (E_{cell}) was the difference in redox potential (ΔE) between the Br^- stabilized precursor and that of the FeMeOH. Because the concentration of Br^- was more than 10 times that of the Na_2PdCl_4 (2 mM), and Br^- has much stronger affinity towards Pd^{2+} than Cl^-,[15] the change of the redox potential of the precursor was mainly due to Br^- coordination instead of a mixed effect from both Br^- and Cl^-. Because the redox potential of FeMeOH should not be affect by Br^-, the driving force of the cell (E_{cell}) was lowered as a result of Br^- coordination. This observation was consistent with the hypothesis that the more the metal ion is stabilized by the ligand coordination, the harder it can be reduced. Fig. 4.9b shows the kinetics of the reaction by monitoring the concentration of FcMeOH. The reaction kinetics was slower when the concentration of the Br^- increased. This observation was consistent with our hypothesis that

higher concentration of ligands leads to lower free energy of the reactants, which results in slower reaction kinetics.

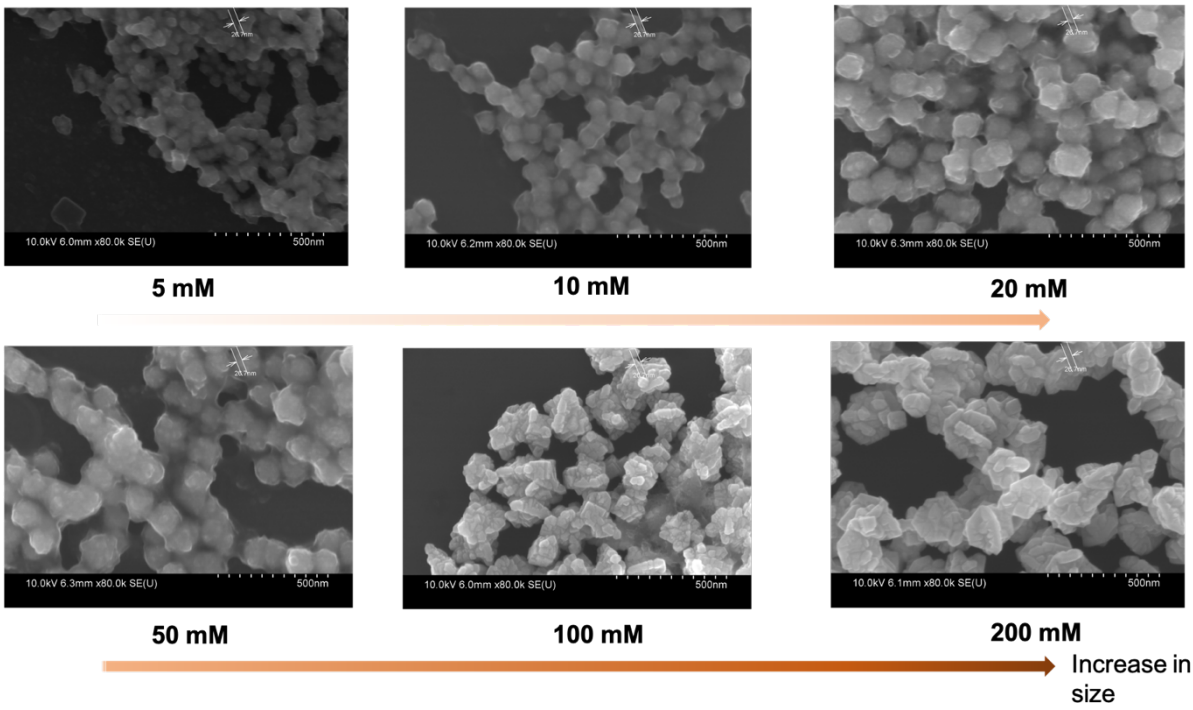


Figure 4.10: SEM images of Pd nanoparticles synthesized with different concentrations of KBr.

We further investigated the size of the resulting Pd nanoparticles. As shown in Fig. 4.10, increased concentration of Br^- ligands resulted in larger Pd nanoparticles. This observation could be explained from the classical nucleation theory. Higher concentration of Br^- results in slower reduction kinetics, hence lower supersaturation level of Pd atoms compared with those with lower Br^- concentration. Therefore, less nuclei were formed in the solution with higher Br^- concentration. Because the concentration of the Pd source was the same for all reaction conditions, the solution with less nuclei generated larger nanoparticles.

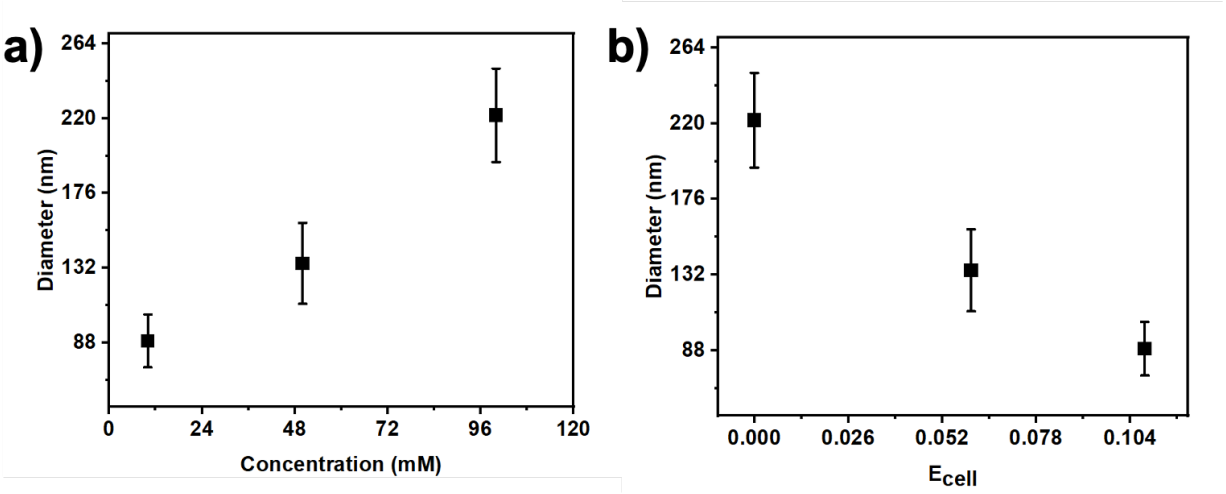


Figure 4.11: Diameter of the nanoparticles as a function of a) KBr concentration and b) E_{cell}.

We further plotted the diameter of the particles as a function of the Br^- concentration and E_{cell} (Fig. 4.11). The diameter of the particles increased as the concentration of the Br^- ligand increased (Fig. 4.11a), and the diameter of the particles decreased as the E_{cell} decreased (Fig. 4.11b). This preliminary result gave us a way of correlating the starting free energy of a system and the structural output. The E_{cell} can help us make informed choices on the type and concentration of precursors and ligands. More data is needed to generalize a definitive relationship between the starting chemicals and final structures.

Finally, we quantitatively fitted the kinetic curves in Fig. 4.9b. We adapted the Finke-Watzky model[16-17] as follows

$$Pd^{2+} + 2Fc \xrightarrow{k_1} Pd^0 + 2Fc^+$$

$$nPd^0 \xrightarrow{homougeneous\ nucleation} Pd^0{}_n$$

$$Pd^0{}_n + Pd^{2+} + 2Fc \xrightarrow{k_2} Pd^0{}_{n+1} + 2Fc^+$$

$$-\frac{d[Fc]}{dt} = k_1 [Pd^{2+}] [Fc]^2 + k_2 [Pd^{2+}] [Fc]^2 [Pd^0{}_n]$$

Fc represents FeMeOH. Pd^{2+} represents Pd ion precursor, Pd^0_n and Pd^0_{n+1} represents the formed nuclei. k_1 and k_2 are the rate constant for solution reduction and surface reduction, respectively. The rate for solution reduction was directly related to the starting reactants, whereas the rate for surface reduction not only relied on the concentration of available Pd^{2+} and the concentration of FeMeOH, but also on the concentration of nuclei generated by the solution reduction. Herein, we will focus our discussion on the relationship between k_1 and E_{cell}. Table 4.2 shows the fitted rate constants at different concentration of Br^-. k_1 decreased as the concentration of Br^- increased.

Table 4.2: Fitted rate constants for kinetic curves with different Br^- concentration.

KBr Concentration	20mM	50mM	100mM
k_1 (mM^{-2}/s)	0.318	0.046	0.003
k_2 (mM^{-3}/s)	3.019×10^{-15}	1.46×10^{-23}	0.003

According to the Butler-Volmer model,{Bard, 1980 #115} rate constant (k) of a reaction can be related to the potential (E) using the following equation

$k = k^0 \exp[-af(E - E^0)]$.

k^0 is the standard rate constant. a is the transfer coefficient, f= F/RT. We wonder whether we can use the Butler-Volmer model to establish the quantitative relationship between E_{cell} and k_1 As shown in Fig. 4.12a, we plotted ln (k_1) as a function of E_{cell}. ln (k_1) exhibited a linear relationship with that of E_{cell}, which was consistent with the Butler-Volmer model. We also plotted the relationship between the diameter of the particles as a function of ln (k_1), it also agreed with our hypothesis that smaller k_1 (larger lnk_1) produced larger particles because of the lower supersaturation lever of Pd atoms.

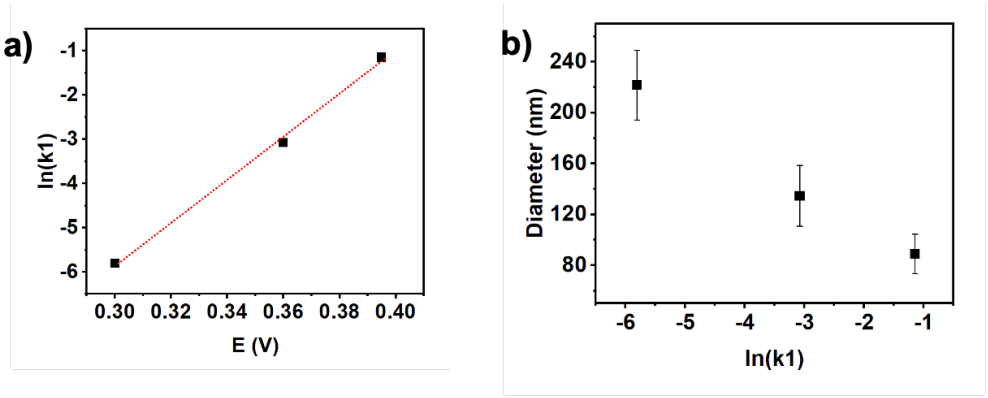


Figure 4.12: a) Relationship between k_1 and E_{cell}. b) Relationship between diameter of the nanoparticles and k_1.

4.3 Conclusion

In conclusion, this Chapter demonstrated the preliminary effort to establish the quantitative relationship between the starting reactants, the kinetics, and the structural parameters in the synthesis of metal nanocrystals .I developed a model system of synthesizing Palladium nanocrystals by using Pd halides and pseudo-halides as the precursors and redox mediators as the reducing agents.I also monitored reaction kinetics using UME, and established the preliminary quantitative relationship between the driving force, the kinetics and the size of the Pd nanoparticles. The tunable coordination chemistry of the precursors and the reversible redox behavior of the reducing agents enabled designing a synthesis protocol based on the thermodynamic driving force and the kinetic outputs of the reaction. This work signifies an important step towards fully digitalized design towards functional nanomaterials.

4.4 Experimental section

4.4.1 Fabrication of Ultramicroelectrode

A glass capillaries was cut in two halves, a torch was used to seal one end of each half. A 1-2 cm Pd wire was inserted into the capillary. The UME was sealed using a heating coil. Silver epoxy was used to build external connection of the microwire to a regular wire for external connections. Finally the UME was polished and sharpened to expose the microwire and proper radius of the glass sheath.

4.4.2 Pd nanocrystal synthesis and monitoring reaction kinetics

4.5 mL solution with 3 mM redox mediators, 5.55 mM PVP and 100mM KBr was prepared. A Pd UME, a carbon counter electrode and and a Ag/Ag reference electrode were positioned in the solution. A constant potential was held while the current was monitored as a function of time (i-t curve). Once the current stopped changing, 0.5 mL 10 mM Na_2PdCl_4 was immediately added to the solution. The i-t curve was monitored until the current stopped changing. The resulting solution was centrifuged 3 times. The Pd nanoparticles were analyzed by SEM.

4.5 References

1. Heinz, H.; Ramezani-Dakhel, H., Simulations of inorganic-bioorganic interfaces to discover new materials: insights, comparisons to experiment, challenges, and opportunities. *Chem. Soc. Rev.* **2016,** *45* (2), 412-448.

2. Bard, A. J.; Faulkner, L. R., Fundamentals and applications. *Electrochemical methods* **2001,** *2* (482), 580-632.

3. Heinze, J., Ultramicroelectrodes in Electrochemistry. *Angewandte Chemie International Edition in English* **1993,** *32* (9), 1268-1288.

4. Walsh, D. A.; Lovelock, K. R. J.; Licence, P., Ultramicroelectrode voltammetry and scanning electrochemical microscopy in room-temperature ionic liquid electrolytes. *Chemical Society Reviews* **2010,** *39* (11), 4185-4194.

5. Berkh, O.; Burstein, L.; Shacham-Diamand, Y.; Gileadi, E., The Chemical and Electrochemical Activity of Citrate on Pt Electrodes. *Journal of The Electrochemical Society* **2011,** *158* (6), F85.

6. Tamirat, A. G.; Guan, X.; Liu, J.; Luo, J.; Xia, Y., Redox mediators as charge agents for changing electrochemical reactions. *Chemical Society Reviews* **2020,** *49* (20), 7454-7478.

7. Lim, B. J.; Hwang, I.; Ellington, A. D.; Sessler, J. L., Synthesis of Ferrocene Derivatives Allowing Linear Free Energy Studies of Redox Potentials. *Helvetica Chimica Acta* **2019,** *102* (2), e1800186.

8. Lim, B.; Jiang, M.; Tao, J.; Camargo, P. H. C.; Zhu, Y.; Xia, Y., Shape-Controlled Synthesis of Pd Nanocrystals in Aqueous Solutions. *Advanced Functional Materials* **2009,** *19* (2), 189-200.

9. Favier, I.; Pla, D.; Gómez, M., Palladium Nanoparticles in Polyols: Synthesis, Catalytic Couplings, and Hydrogenations. *Chemical Reviews* **2019**.

10. Yin, X.; Shi, M.; Wu, J.; Pan, Y.-T.; Gray, D. L.; Bertke, J. A.; Yang, H., Quantitative Analysis of Different Formation Modes of Platinum Nanocrystals Controlled by Ligand Chemistry. *Nano Letters* **2017,** *17* (10), 6146-6150.

11. Ortiz, N.; Skrabalak, S. E., On the dual roles of ligands in the synthesis of colloidal metal nanostructures. *Langmuir* **2014,** *30* (23), 6649-6659.

12. Langille, M. R.; Personick, M. L.; Zhang, J.; Mirkin, C. A., Defining Rules for the Shape Evolution of Gold Nanoparticles. *Journal of the American Chemical Society* **2012,** *134* (35), 14542-14554.

13. Jin, M.; Liu, H.; Zhang, H.; Xie, Z.; Liu, J.; Xia, Y., Synthesis of Pd nanocrystals enclosed by {100} facets and with sizes <10 nm for application in CO oxidation. *Nano Research* **2011,** *4* (1), 83-91.

14. Heit, Y. N.; Sergentu, D.-C.; Autschbach, J., Magnetic circular dichroism spectra of transition metal complexes calculated from restricted active space wavefunctions. *Physical Chemistry Chemical Physics* **2019,** *21* (10), 5586-5597.

15. Elding, L. I., Palladium(II) halide complexes. I. Stabilities and spectra of palladium(II) chloro and bromo aqua complexes. *Inorganica Chimica Acta* **1972,** *6*, 647-651.

16. Watzky, M. A.; Finke, R. G., Transition Metal Nanocluster Formation Kinetic and Mechanistic Studies. A New Mechanism When Hydrogen Is the Reductant: Slow, Continuous Nucleation and Fast Autocatalytic Surface Growth. *Journal of the American Chemical Society* **1997,** *119* (43), 10382-10400.

17. Yang, T.-H.; Peng, H.-C.; Zhou, S.; Lee, C.-T.; Bao, S.; Lee, Y.-H.; Wu, J.-M.; Xia, Y., Toward a Quantitative Understanding of the Reduction Pathways of a Salt Precursor in the Synthesis of Metal Nanocrystals. *Nano Letters* **2017,** *17* (1), 334-340.